Understanding the Relationships between the Structure and the Physical Properties of Conjugated Polymers using Particle Scattering and Electronic Properties

Lorenzo Guio

A dissertation

Submitted in partial fulfillment of the

requirements for the degree of

Doctor of Philosophy

University of Washington

2024

Reading Committee:

Christine Luscombe, Chair

Lilo Pozzo

Eleftheria Roumeli

Program Authorized to Offer Degree:

Materials Science and Engineering

University of Washington

Abstract

Understanding the Relationships between the Structure and the Macro-Scale Properties of Conjugated Polymers using Small Angle Scattering and Field Effect Mobility

Lorenzo Guio

Chair of the Supervisory Committee

Christine Luscombe

Materials Science and Engineering

Conjugated polymers are semiconducting materials of high interest for use in organic photovoltaics (OPV), organic light-emitting diodes (OLED), and organic field-effect transistors (OFET) owing to their light weight, flexibility, and solution processability. However, their electronic and physical property limitations have prevented their widespread use in devices such as solar cells and transistors. This work seeks to understand the relationship between tunable parameters, microstructure morphology, and device properties in conjugated polymers to design better materials and bridge the performance gap with traditional semiconductors. Specifically, characterization techniques including particle scattering and electronic property measurements are used to understand the connection between molecular structure, thin film morphology and electronic performance in thiophene and indacenodithiophene based conjugated polymers.

Acknowledgements

I want to thank many people in my life for their collaboration, support, friendly competition and friendship. No doctoral thesis, especially not this one, is achievable without the many people that contribute directly and indirectly to the time and work that compose it.

I want to thank my advisors Prof. Christine K. Luscombe and Prof. Lilo D. Pozzo. If they did not take a chance on me on multiple occasions, I would not have even had the opportunity to pursue this degree. Thank you both for all the scientific, intellectual and personal support that you have provided me and guided me with through my degree. Most of all, I want to thank you for your patience as this period saw multiple life changes for all of us including an entire pandemic and moving a family to Japan.

I want to thank all the lab members of both the Luscombe and the Pozzo labs. Every day you were who I relied on for advice, for help when it was most needed and for friendship. I especially want to thank those students who served as mentors to me and whom without I would have been much more lost in the early years. Thank you, Dr. Jon Onorato, Dr. Wesley Tatum, and Dr. Caitlyn Wolf. Your knowledge and patience in teaching me the ground level workings of research were more important than you know. I also want to thank the friend groups outside and inside of research. The most important skill in tackling a challenge is having the right mindset, and that starts with your friends. Amazon squad, SENSOL, Saffron King and Fantastic Four, you know who you are, and without y'all this isn't possible.

I want to thank my family, especially my parents, one of which decided to pursue his own PhD once I began my own. Thank you for not only encouraging me to take this road, but supporting me in innumerable ways over my entire career and even serving as a bit of friendly competition (I lost). Last, I want to thank Clara, my partner, there is no one individual who has put up with me more these last 5 years. Thank you, biddy.

Table of contents

List of Figures

List of Tables

Chapter 1. Introduction and Motivation

1.1 Conjugated Polymers

Traditional semiconductors are integral to modern electronic devices. However, inorganic (non-carbon-based) semiconductors such as silicon and gallium arsenide have several limitations that make their use in specific applications difficult. One such application is healthcare devices that can be attached directly to the skin or implanted in the body[1]. Wearable devices, which are of high interest in the field of medicine, require that they be flexible, stretchable, and durable to survive the stretching, pulling, and twisting of their environment. These properties are not associated with typically brittle inorganic semiconductors, which are highly crystalline. Clever engineering has been employed, which allows devices made of inorganic semiconductors to stretch by constructing prestressed mechanical structures such as springs[2]. Unfortunately, the fabrication of these structures is a slow, multistep process that greatly limits large-scale manufacturing. Another application of semiconductors is the use of photovoltaics. Solar cells require a large area for light collection. Producing large-area devices using inorganic semiconductors is expensive because of the limited manufacturing methods involving slow crystal growth or vapor deposition[3,4]. This high manufacturing cost has significantly limited the use of solar energy technologies based on inorganic semiconductors.

There is a need for a new generation of flexible, stretchable materials that can be manufactured into large-area devices. Organic semiconductors, which include carbon in their chemical makeup, are one such class of materials. Within organic semiconductors are a subset of materials known as semiconducting or conjugated polymers (CP). Synthetic polymers, commonly known as plastics, are ubiquitous in everyday life and can be found anywhere from gaskets on space stations to cases on phones. They have been used in a variety of applications since their

invention in the early 20th century and were thought to be electronic insulators until the 1970s. This mindset was changed with the invention of the first conducting polymer, polyacetylene, for which the creators Shirakawa *et al.* were awarded a Nobel prize in 2000[5,6]. Since then, CP, such as polyaniline, polythiophene, and polypyrrole, have been researched and developed for use in electronic devices[7]. CPs are solution processable, which facilitates large-scale manufacturing because they can be rapidly deposited over large-area substrates under near-to-ambient conditions. This property has been exploited to create roll-to-roll fabricated and flexible solar cells (Figure 1-1)[8,9]. Scalable manufacturing reduces the cost of fabricating large areas of active material, thus reducing the cost of photovoltaics and improving their energy payback time. Energy payback time is the time required for a photovoltaic system to recover the energy invested in its production, and

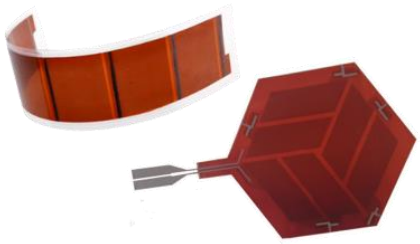

Figure 1-1: Ribes Tech, an Italian company, is manufacturing roll to roll organic solar cells at the time of this writing.

improving this figure of merit is vital for more widespread adoption of the technology[10]. CP can also be made both flexible and stretchable for use in wearable electronics, and skin-applied sensors have been manufactured in laboratories. These biosensors and skin-compatible transistors have shown good electronic device performance, while maintaining their ability to deform and stretch along the human skin[11,12].

The overall device performance of CP is not as good as that of traditional inorganic semiconductors. Electronic device performance figures of merit for these applications include the

charge carrier mobility and photovoltaic power conversion efficiency (PCE). Charge carrier mobility is an intrinsic property of a material that allows the flow of electrons or electron holes in a potential field and is directly proportional to conductivity. Charge carrier mobility in the best doped organic materials (30 $cm^2\ V^{-1}\ s^{-1}$) is an order of magnitude lower than that of doped silicon (500 $cm^2\ V^{-1}\ s^{-1}$)[13,14]. The PCE is the percentage of incident solar energy that is converted into electrical energy. Among organic semiconductors, 19.3% has been achieved for a single-junction solar cell, whereas single-crystal silicon solar cells achieve a PCE of up to 27%.[15,16] Despite their shortcomings, organic semiconductors have gained attention owing to their promise of flexible, stretchable, and solution-processable electronic devices. In the years since their conception, organic electronic devices have seen an increase in charge carrier mobility that surpasses the rise that silicon experienced, and even with lower PCE, some organic photovoltaics are already more affordable, with shorter energy payback times than their inorganic counterparts[17,18].

The source of their properties must be well understood to develop better CPs for advanced applications. It has been demonstrated that the structure and form of these materials at the nano- and microscopic scales are fundamental to the determination of their electronic properties[19–22]. It is well understood from traditional plastics that the same structures determine the mechanical properties of bulk materials, such as stretchability and toughness[23–26]. To improve their performance, researchers must better understand the relationship between the CP structure and its physical properties.

1.2 Polymer Structure and Properties

Polymers, or as they are more commonly referred to, plastics, owe their mechanical and physical properties to their molecular structure. At the molecular level, polymers are composed of many repeated subunits called monomers, which are connected to each other by covalent bonds

(Figure 1-2). Like the small molecules that make up the rest of the materials in the world, the physical properties of polymers are determined by the nature of the monomer that makes them up. In addition, the arrangement in which the monomers are found in the polymer chain, as well as other properties such as the chain length, also influence the materials properties[27]. Polymers can be found everywhere; for example, some natural polymers include proteins, such as wool, DNA, and carbohydrates, such as starch. Synthetic polymers are man-made and include polystyrene and polyethylene, which are used in household items, such as chairs. Biopolymers, such as polylactic acid (PLA), are used in biodegradable containers and 3d printing.

To better understand what allows polymers to have such a diverse array of properties, one must investigate the monomer. The size, shape, and functional groups of the subunits can affect the mechanical behavior. For instance, the presence of aromatic rings in monomers such as styrene results in polymers that are more rigid and glassy owing to the stiff nature of the aromatic groups[28]. The carbon-fluorine bonds found in the polytetrafluorethylene (Teflon) monomer allow it to serve as a non-stick cooking surface, as it makes the polymer very hydrophobic and non-reactive. However, some properties arise from the arrangement of the monomer subunits. The best example is polyethylene, the simplest polymer that consists of a chain of carbon atoms (Figure 1-2). When these atoms are connected in a straight chain, they can pack well together and form crystals, resulting in a very strong, stiff, and durable material that can be used in tough containers, such as milk jugs. However, if the monomers are connected in a non-linear manner with branches in the polymer chain, the chains cannot pack well together. This results in flexible and non-durable materials that are used in plastic bags.

In much the same way as the previously mentioned household polymers, conducting

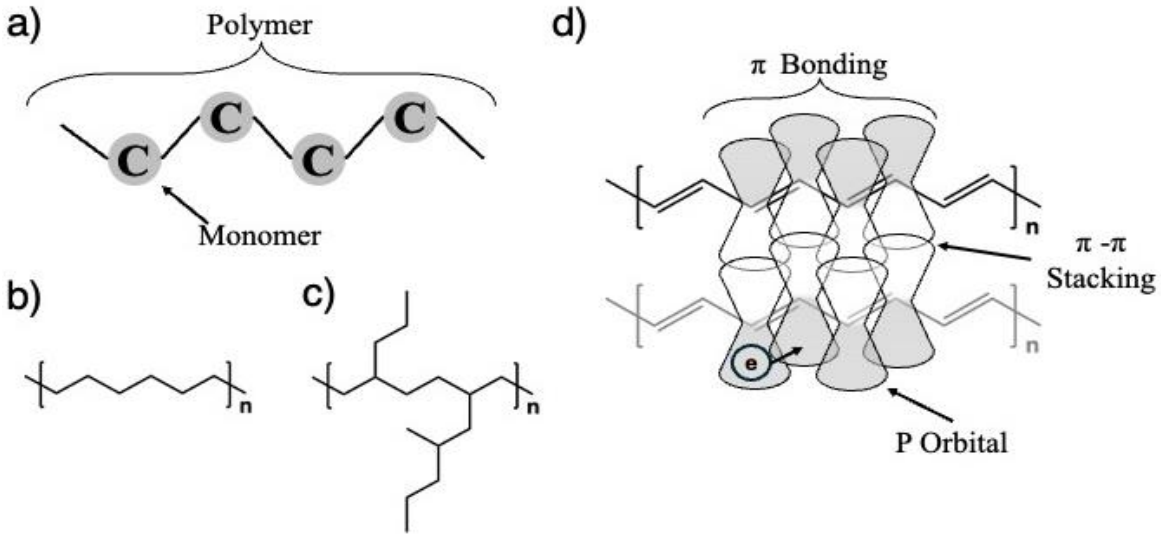

Figure 1-2: Schematic of polymer structures. a) Polymer and monomer relationship, b) linear polyethylene, c) branched polyethylene, d) overlapping π bonding orbitals in polyacetylene.

polymers can transport charges because of both the monomer molecular structure and the ordering of the monomers in the chain. Take polyacetylene: a carbon chain of alternating single and double bonds. The carbon chain is almost identical to that of polyethylene, which is used for plastic bags; however, the connection between carbon atoms includes an additional bond, which is called a π bond. The alternating single- and double-bond structures manifest as a series of connected π bonds that continue throughout the entire chain, as shown in Figure 1-2. Because of the continuous π bond structure, electrons can move between carbon atoms. These "delocalized" electrons can then be transported throughout the chain backbone (intrachain transport) upon being pushed by a potential field[29]. Charge transport can also occur between different chains or chain segments that have overlapping *P* orbitals (interchain movement) owing to their proximity. This overlap, called π-π stacking, allows charge carrier transport between the stacked chain segments. This form of carrier movement is slower than intrachain transport, yet it is fundamental for efficient transport

in three dimensions[30,31]. If electronic charges are transported only along the backbones of these polymers, then charges cannot move across the bulk material because polymer chains thermodynamically conform in a way that prevents them from being completely extended, thus covering long distances.

Crystalline CP shows microstructural features like those of traditional crystalline polymers such as linear polyethylene. The morphology consists of ordered polymer segments dispersed in

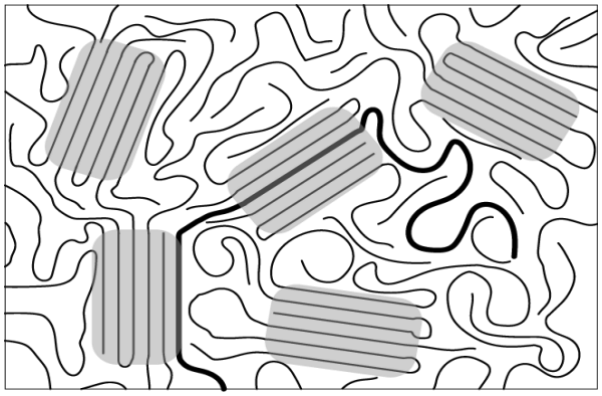

Figure 1-3: Crystalline polymer morphology with highlighted tie chain. The gray areas are crystal domains.

random polymer coils, forming a semicrystalline ordering, as shown in Figure 1-3. Studies have found that charge transport is most efficient through these ordered crystalline regions of CP. In the crystalline regions, chains remain rigid and coplanar, having very few chain torsions between monomer units. Chain torsion leads to trap states for charge carriers; this occurs because the overlapping orbitals that participate in the continuous π bonding have a dumbbell shape. When they rotate with respect to each other, they can cease to overlap, thus creating a local spot where charges can no longer move. If a chain is not planar because of significant chain torsion, then there will be many "breaks" along the conduction path, which manifests as a positive correlation between chain planarity and efficiency of intrachain transport.[32–34] Also, in the crystalline regions, there are more opportunities for interchain charge transport. Good chain packing in more ordered

regimes leads to close proximity of chains, and therefore extended π–π stacking.[32,35] In addition to exhibiting a folded lamellar structure, CP also forms ordered regions with domains of greater length, such as those seen in structures such as nanowires and nanoribbons.[36,37] The most efficient material charge transport occurs when there is a high degree of interconnectivity between crystalline domains by tie chains, as shown in black in Figure 1.1. Tie chains are extended polymer chains that participate in π–π interactions with multiple ordered regions, serving as conductive bridges between them.

There is still much left to be discovered in the structure-property relationships of CP. Early CP such as poly (3-hexylthiophene) and poly(2,5-bis(thiophen-2-yl)thieno3,2-b]thiophene) (pBTTT) displayed extensive crystallinity, which was found to be positively correlated with device performance; therefore, research has focused on improving the formation and control of ordered and crystalline regimes. However, newer donor-acceptor copolymers, such as poly(indacenodithiophene-C16-benzothiadiazole) ($PIDT_{C16}$-BT), challenge this idea by demonstrating high field-effect charge mobility but lacking detectable long-range order[38–40]. Having access to good electronic performance without constraining the mechanical properties by maintaining high degrees of crystallinity opens possibilities for applications of conjugated polymers.

Although organic semiconductors have been investigated because of their claim to traditional polymer properties, such as deformability and high fracture toughness characteristics, high-performing CP tend to not fully display this traditional plastic behavior. The need for rigid polymer backbones and highly ordered regions to improve electrical performance leads to higher crystallinity, which decreases the elastic modulus of the material.[23,24] Flexibility in neat CP is obtainable but comes at the cost of device performance, The newer donor-acceptor copolymer

materials are paving the way for more mechanically compliant high-mobility materials since they do not depend on crystallinity to display high mobilities, but there is still ground left to cover in optimizing them for devices and understanding how they work. In addition, researchers have been able to overcome mechanical weaknesses in crystalline CP by blending them with other polymers like elastomers.[41] Blends additionally can introduce a method by which the active device layer can be modified to fit specific mechanical and electronic parameters.

1.3 Polythiophenes

The most widely studied CP are semicrystalline poly(3-alkylthiophene) (P3AT). P3AT has been thoroughly investigated because of its good optoelectronic properties, stability, and ease of side chain tailoring. They serve as models for semi-crystalline CP. Figure 1-4 shows the molecular

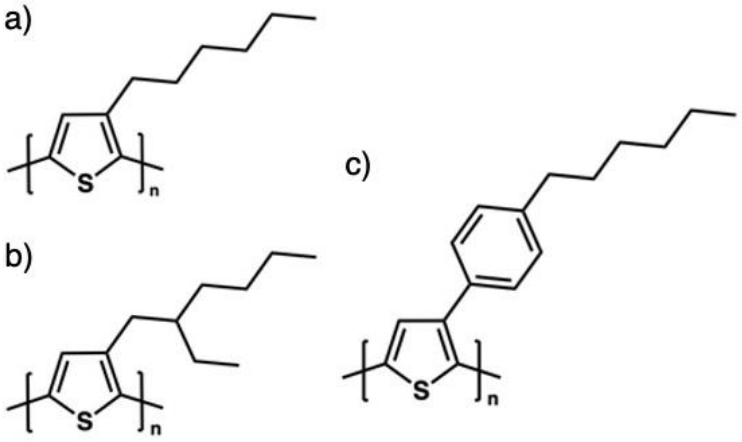

Figure 1-4: Molecular structure of polythiophenes. (a) poly(3-hexylthiophene) (b) poly(3-(2-ethylhexyl) thiophene) (c) poly(3-(4-octylphenyl) thiophene).

structures of various P3AT, including what is known as the fruit fly in the field of CP, poly(3-hexylthiophene) (P3HT). The molecular structure of these polymers consists of an electron-rich thiophene backbone complemented by alkyl side chains that give the polymer its solubility and aid with packing. Each monomer has one side chain, giving it directionality, which allows for different coupling along the backbone. The morphology of P3HT consists of crystalline regions dispersed in an amorphous polymer matrix. The crystalline domains assume three degrees of order. The first

degree is the polymer backbone itself, which propagates in the [001] direction in the crystal. The second degree of order originates from π–π stacking by chains directly adjacent to each other and normal to each other. π–π stacking occurs under two circumstances: chain folding and different

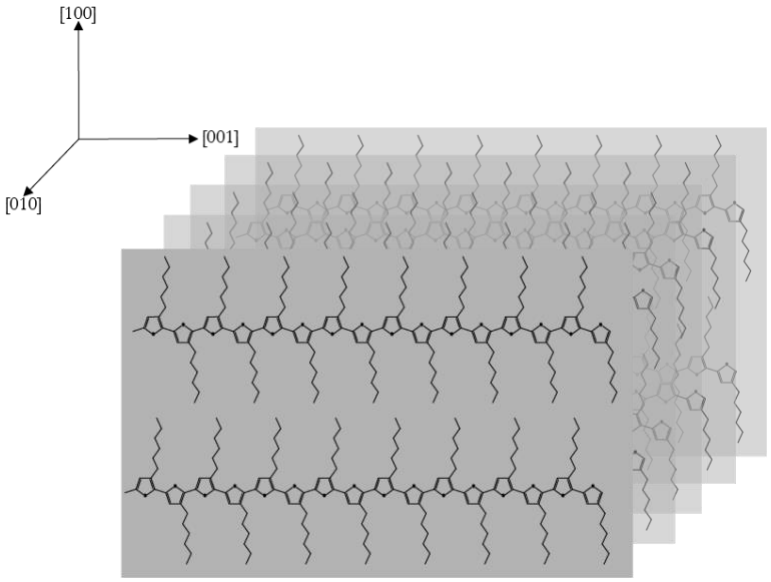

Figure 1-5: Crystal structure of P3HT crystalline regime.

chain stacking. The π-π stacking order of the crystal propagates in the [010] direction. The third degree originates from the side-chain crystallization, which occurs in the [100] direction. The crystal lattice directions and the corresponding crystallite schematics are shown in Figure 1-5. As mentioned before, charge transport is dominated by intrachain movement along the [001] direction and supplemented by interchain movement along the π-π stacking direction [010].

In addition to forming crystallites, P3HT can and has been formed into higher-order structures such as nanoribbons and nanowires.[42] Nanowires of P3HT can be formed most commonly using self-assembly methods. The nanowires have a width and height equal to the [001] and [100] crystal directions, respectively, and typically measure 24-27 nm wide and 3-4 nm tall, respectively. Their length is in the π–π stacking direction [010], which is typically on the order of one micron. The typical film morphology of P3HT nanowires is shown in Figure 1-6. The formation of nanowires of P3HT and using a material combination of nanowires, which are

crystalline, smaller crystallites, and amorphous chains in the thin-film active layer of OFETs have been shown to improve the mobility of the material without nanowires. The nanowires form a better interconnected network of efficient charge transport ordered regions that facilitate charge carrier flow throughout the film.[43,44] For this reason, it is favorable not only to have crystalline regions in P3AT but also for them to be organized into higher-order nanofibers and nanowires.

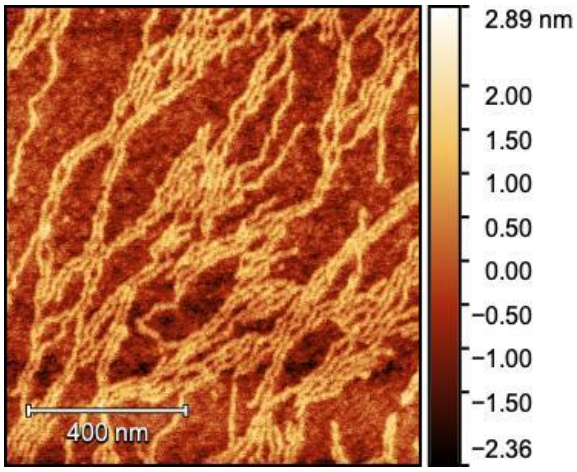

Figure 1-6: Atomic force microscopy image of P3HT nanowires formed using the whisker method.

Due to the intimate relationship between microstructure and macroscale properties, being able to control the microstructure of conjugated polymers is of the utmost importance. The CP microstructure is influenced by the molecular structure and characteristics of the monomer units and polymer chains. It is also influenced by processing factors, such as polymer deposition conditions, post-deposition annealing, and blend formation with other polymers. The first molecular parameter that influences the microstructure is the length of thiophene side chains and their orientation within the polymer. Park *et al*. demonstrated that shorter side chains were correlated with better chain packing in the ordered domains, leading to better mobility as compared to longer side chains.[45] However, shorter side chains also limit the processability of the polymer as it becomes less soluble. Therefore, the field gravitates towards a balance between good chain

packing and sufficient processability. In special applications, such as blends, it may be beneficial to use the side chain length to control interactions between components and influence the morphology. Another aspect of the side chains is their relative positions on the thiophene units

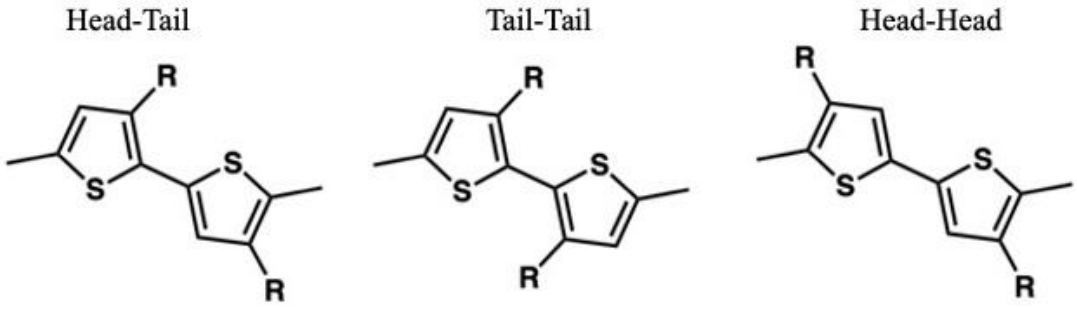

Figure 1-7: Types of couplings possible in the synthesis of P3HT that give rise to regioregularity in the polymer chain.

along the backbone. The figure of merit for this is called regioregularity, which is the percentage of head-tail couplings of thiophenes in P3HT. Figure 1-7 shows the different types of coupling that can occur, leading to different degrees of regioregularity. A higher percentage of the polymer that is coupled in a head-tail conformation allows polymer chains to adopt planar configurations that increase conjugation and allow for better chain packing.[32,46] Regio-irregularities like head-head and tail-tail coupling lead to sterically driven chain torsion, which disrupts conjugation and the crystal lattice. Higher regioregularity results in higher degrees of crystallinity and better formation of higher-order structures, such as nanofibers.

Another influential molecular factor in the overall morphology of P3HT is the molecular weight of the polymer chain. Increasing the molecular weight is correlated with increasing crystallinity and tie-chain content, which leads to increases in charge transport.[47,48] Furthermore, there are critical chain lengths, past which certain phenomena are displayed. The first is chain folding, in which the polymer chain becomes long enough to not simply stack with other extended chains in proximity but folds completely to π-stack with itself. This occurs at around 50 monomer

units of P3HT and is shown schematically in Figure 1-8.[48] The other critical length is entanglement, in which the backbone becomes long enough to form tie-chains. Tie chains result

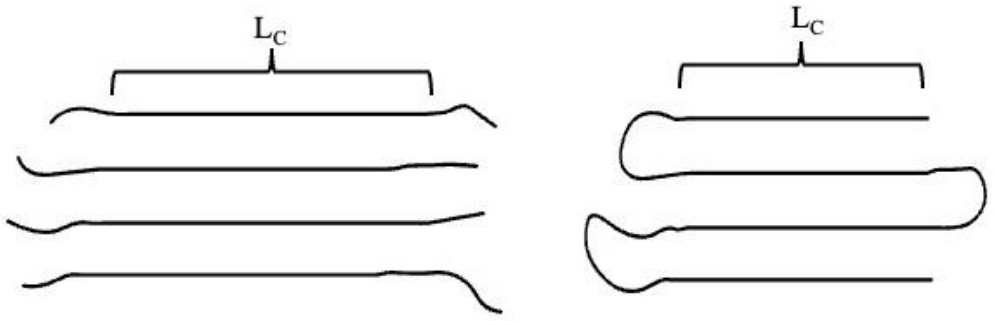

Figure 1-8: Chain packing of different polymer chain lengths of P3HT. Short chains stack (left) and long chains fold (right). This impacts the crystal width (L_C).

in an increase in the amount of connectivity because more chains participate in multiple ordered regions. In general, the higher percentage of regioregularity and longer the polymer chains are, the higher the quality of the nanowires formed, and higher percentage of overall polymer incorporated into the nanowires.[43]

In addition to the molecular structure and weight, the processing conditions are the most important tunable parameters for controlling the film morphology and polymer microstructure. One of the processing techniques that occurs when polymers are in solution is self-assembly. During self-assembly, disordered molecules of a material are induced to spontaneously organize themselves into higher-order structures driven by local inter-and intramolecular interactions. In polymers, self-assembly is an invaluable tool for controlling chain conformation. The simplest example of self-assembly in CP, which also happens to be the most used technique, is supersaturating a solution with CP and allowing slow phase separation to achieve a higher order in the CP phases. This ordering is driven by the thermodynamic forces. In P3HT, π-stacking of thiophene rings is an energetically favorable conformation that leads to crystallite formation. This results in the formation of fibers and crystallites in these solutions. Samitsu *et al.* developed a

method by which P3HT is dissolved in a poor solvent, anisole, to form a supersaturated solution. The solution was heated and stirred to fully dissolve the P3HT. After slowly cooling the supersaturated solution over 3 h, nanowires of P3HT were formed.[49] This is most commonly referred to as the whisker method. Chang *et al*. formed nanowires in dilute solution by irradiating the solution using UV radiation.[50] Most self-assembly methods require the use of creating a slightly unfavorable condition for the polymer chains to stay in solution, thus leading to aggregates, which then lead to higher-order structures (nanowires). It is therefore important to note that self-assembly and nanofiber formation are related to the interactions between the polymer chains, the solvent, and other system components, such as a different polymer chain.

Another form of processing that has been widely used to fine-tune the morphology of P3AT is thermal annealing. In this method, after films are cast, they are exposed to elevated temperature. At these temperatures, particularly above the glass and crystallization temperatures of the polymers, the chains in the solid state can relax into energetically favorable conformations. The result is a morphology related to the lowering of the thermodynamic energy of chain-chain interactions as well as the interactions at interfaces that can improve the overall device performance. An *et al*. studied the effect of thermal annealing on cast films of P3HT and found that it enhanced the π–π interaction in the P3HT crystal domains.[51] This increase leads to an improved field-effect mobility of the corresponding OFET. At the same time, however, annealing above the crystallization temperature can eliminate higher order structures such as nanowires. The nanowires formed in solution via the whisker method can be reversibly transformed into smaller crystallites by thermal annealing.

Annealing plays an even larger role when a combination of materials is used in composites, such as organic solar cells (OSC). Typical solar cells contain a bilayer of semiconducting materials. One is a donor, and the other is an acceptor. When a light particle, hits the active material and excites an electron-hole pair, the pair must travel to the interface of the two materials where the electron and the electron hole are separated. This separation generates a potential and creates current. In inorganic semiconductor materials, electron-hole pairs can travel large distances before they recombine. Therefore, the device can be designed with two bulk materials meeting at a flat

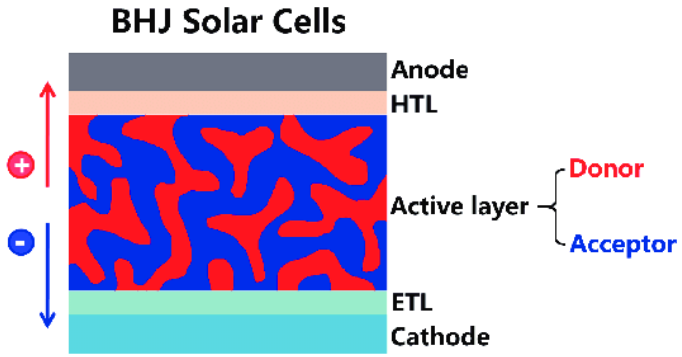

Figure 1-9: Schematic of the layers in an organic solar cell showing the morphology of the bulk heterojunction. The figure is reproduced from Tong *et al.*

interface as an electron–hole pair created hundreds of nanometers away from the interface can travel all the way there before recombination. When photons create an electron-hole pair in CP and other organic semiconductors, they travel only 3-8 nm before they recombine.[52] This is a problem if one wants to have an active layer thicker than 20 nm to capture as much light as possible. To combat this, the active layer is designed as a bulk heterojunction (BHJ) where the donor and acceptor materials are mixed with each other to minimize the domain sizes and increase contact area, where the electron-hole pairs are split. This morphology is shown in Figure 1-9[53]. Research has focused on improving this morphology and the interaction between the donor and acceptor materials to improve solar cell efficiency. One of the most common material

combinations studied is P3HT and [6,6]-phenyl C61-butyric acid methyl ester (PCBM). Chen *et al*. studied the effects of annealing on the morphology and the subsequent impact on the efficiency of charge movement.[54] They found that immediately upon annealing, the two materials formed bi-continuous networks, allowing charges to separate at the high surface area interfaces and then travel through the networks to their opposing charge collecting poles. Post-deposition annealing is fundamental for controlling and understanding the morphology of the CP by itself and as a blend.

1.4 Indacenodithiophene Polymers

Donor–acceptor (DA) copolymers are a relatively new type of conjugated polymer whose molecular design is inspired by the active layer of organic photovoltaics. Within the repeat unit, they contain an electron-rich and electron-poor portion, one serving as the electron donor and the other as the acceptor. The electron-donating units are rich in electrons because of the presence of conjugated systems with electron-donating groups or atoms such as oxygen or nitrogen. Electron-accepting units are electron-scarce owing to electron-withdrawing or electronegative groups. This structure of alternating electron-donating and electron-accepting units affects the optoelectronic properties of copolymers. One positive impact is that the absorption spectrum, the wavelength at

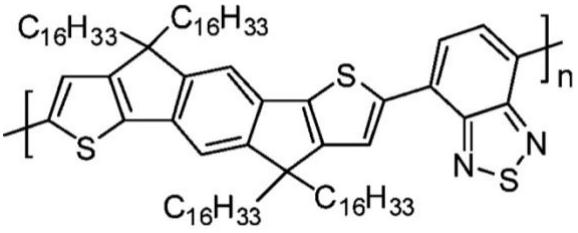

Figure 1-10: Molecular Structure of Poly(Indacenodithiophene-C16-benzothiadiazole). The donor unit is the 5-ring fused structure (left) and the acceptor unit is the 2-ring structure (right).

which a material strongly absorbs light, shifts into the near-infrared region, allowing for the absorption of more wavelengths of light, which is instrumental in efficient solar-energy capture[55].

To serve as a good electron donor, the molecular structure of the donor unit may involve extended fused rings. One such fused ring moiety that emerges from DA polymers is the donor unit, indacenodithiophene (IDT) (Figure 1-10). The molecular structure consists of a central benzene ring joined to two flanking thiophenes by a connecting bridge. Long side chains are attached to the atom on the connecting bridges and are used to solubilize the polymer. Polymers based on IDT tend to have rigid backbones which reduce chain torsion and adopt a planar chain conformation. Both characteristics reduce the trap states to charge mobility, making the polymer adept at conducting charges. Although donor-acceptor polymers were conceived for applications in photovoltaics, some designs such as IDT have resulted in improved electronic properties, meriting their use in many other applications.

Zhang *et al*. synthesized an IDT-based copolymer, poly(Indacenodithiophene-C16-benzothiadiazole) ($PIDT_{C16}$-BT), which displayed an OFET mobility greater than 3 $cm^2\ V^{-1}\ s^{-1}$, beating that of polythiophenes[56]. Surprisingly, in contrast to P3HT, which displays highly crystalline regions, $PIDT_{C16}$-BT shows very broad and weak X-ray diffraction (XRD) peaks, indicating a low degree of overall crystallinity and no detectable long-range crystalline order. To understand why a polymer with such low crystallinity and order can still display such high mobility, various groups have investigated the unique charge transport mechanisms of polymers. Simulations have shown that the IDT unit combined with the acceptor unit, benzothiadiazole (BT), reduces torsion along the backbone via interactions between the nitrogen on the BT unit and the

proton on the adjacent IDT unit[40,57]. These interactions create a large energetic barrier that

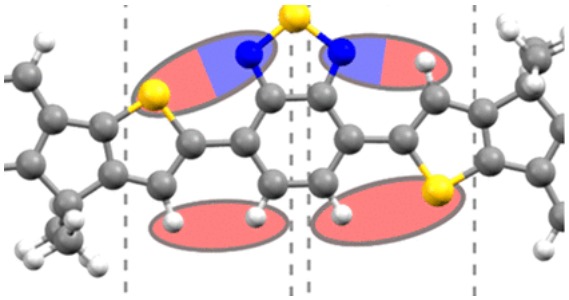

Figure 1-11: Non-covalent interactions of IDT-BT. Red areas of the ovals represent a partial positive charge, while blue areas represent partial negative charge; gray atoms = C, white atoms = H, yellow atoms =S. Reproduced from Wadsworth *et al.*

maintains a specific rotational angle between monomer units. Figure 1-11[58] shows the two conformations that the angle between the BT and IDT unit adopt, with the conformation on the right side being preferential. This preferred conformation leads to a uniquely planar polymer backbone chain. The combination of reduced chain torsion and high planarity minimizes trap states along the polymer backbone. The result is that charge carriers can travel long distances along the chain before requiring interchain hopping in what is called quasi-one-dimensional transport[40]. Only occasional interactions between neighboring chains in the form of local aggregates or small crystals separated by short distances are necessary to allow charges to hop from one chain to the next. The rigidity and planarity that maintain efficient intrachain charge transport combines with the long side chains to disrupt close chain packing. The long side chains extend in a direction normal to the plane of the polymer backbone, creating steric hindrances to π-π stacking and other interactions that semiflexible CP like P3HT experience. The outcome is a polymer with amorphous properties, such as high ductility, that maintains excellent electronic performance[38]. By not requiring crystalline domains for high electronic performance, PIDT$_{C16}$-BT opens possibilities for compatibility with various other types of materials for OPV and blend applications. Ren *et al.* also

employed it as an intrinsically stretchable semiconductor for use in wearable devices.[59] The study applied very thin films of CP on flexible substrates, and demonstrated the use of an array of transistors that could stretch and deform.

The crystalline domains of IDT-based polymers are composed of small and infrequent interactions between polymer chains. The typical characterization method used to determine the quantity, size and structure of crystalline domains is grazing incidence wide angle X-ray scattering (GIWAXS). Using this technique, the π-π stacking and alkyl side chain distances have been determined. However, there is no crystal unit structure analogous to that of polythiophenes because crystal domains are of small length scales. They are composed of one chain segment interacting with another through side chain interdigitation or acceptor unit π-π stacking[40]. Modifications to the molecular structure of IDT-based polymers have been investigated to understand their effects on polymer properties. Much like its semiflexible analogs, IDT-based polymer film microstructure can be tuned by side chain engineering. It would be expected that the side chains act as insulators between polymer chains so decreasing their length would allow for closer interaction between chains and remove steric hindrances to chains coming together. Bronstein *et al*. studied the influence of side chain length on electronic performance[60]. They found that long side chains were necessary for solution processability of the polymer and made better films for devices compared to shorter side chains. Because of this, the highest mobility came from the longest side chains of 16 carbons long. Surprisingly, they also found the highest degree of aggregation occurred with the long side chains which also aided in improved device performance. This showed that shorter side chains are not necessarily better for processability or final film morphology.

The acceptor unit of IDT-based copolymers can be swapped for structures that have specific electronic properties that tune the bandgap. Studies have shown that using different acceptor units

allows the control of the HOMO level which is a useful tool for tailoring the polymers for photovoltaic applications[61]. However, using different acceptor units also changes the interaction between the donor and acceptor units that induces the high planarity seen in $PIDT_{C16}$-BT. Certain acceptor units can create very favorable bandgaps for solar capture but decrease chain planarity and ultimately, decrease electronic device performance. For transistor applications, tuning the acceptor unit can lead to varying mechanical and electronic properties. Li *et al*. synthesized three IDT-based polymers with different acceptor units that had varying degrees of chain torsion due to interactions between the donor and acceptor[62]. They found that when the acceptor unit induced more chain torsion, the hole mobility would decrease, but ductility of the polymer would increase. The decreased planarity decreased intermolecular interactions between chains which aids in mechanical compliance but hinders electronic connectivity and device performance.

Another structural modification occurs at the connecting bridge between thiophen and benzene in the IDT core. The bridging carbon atom can be swapped for other heteroatoms such as silicon or germanium. Those molecular changes have shown to influence the chain packing and overall aggregation. Larger atoms push away the side chains from the polymer backbone. Since those side chains serve as steric hindrance from π-π stacking; the effect is improved connectivity between polymer chains[58,61,63]. Although not a molecular structure modification, molecular weight is a polymer parameter used to tune material properties as has been shown for many polymers and would be expected to make an impact in the properties of IDT based polymers. Zhao *et al*. studied the impact of increasing the molecular weight of $PIDT_{C16}$-BT to 1MDa[64]. They found that the increased molecular weight increased both the device performance and the deformability of the polymer reaching 100% crack-onset strain (COS). The authors proposed a microstructural model

where the polymer chains form locally strained conformations that facilitate efficient charge transport while allowing for large deformations under stress.

Although IDT-based polymers have shown promise as nearly amorphous materials that still display high charge mobilities, it is still of interest to develop techniques to manipulate and improve their morphology and long-range order. Studies of molecular modifications to IDT-based polymers tend to cover the device performance and very limited morphological figures of merit: π-π stacking distance from GIWAXS, and general degrees of aggregation from absorption spectroscopy. To improve and manipulate the morphology, it must first be well characterized. Some groups have attempted using novel techniques and analysis to unravel the film morphology of IDT-based copolymers. Cendra *et al*. used low-dose transmission electron microscopy (TEM) and high-resolution TEM (HRTEM) to image and quantify the nanoscale and mesoscale

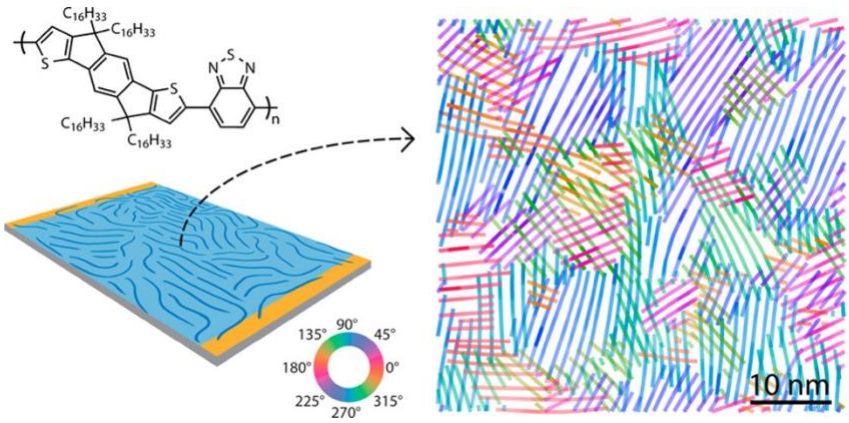

Figure 1-12: Representation of PIDTC16-BT film microstructure taken from HRTEM. Figure reproduced from Cendra *et al.*

organization of the copolymer. These techniques revealed nanoscale crystallites of aligned polymer chains throughout the film[65]. The analysis showed a film which contained short and medium range order of aligned polymer chains that formed grains, which had local preferential alignment as shown in Figure 1-12. As was expected, the long side chains prevent dense packing and therefore although there were locally ordered grains, the film is mostly amorphous.

As covered in the previous section, there are a variety of methods by which semicrystalline CP can be modified post-synthesis to improve the material properties. The two most prevalent methods are the pre-aggregation of the polymer in solution and thermal or vapor annealing after polymer film deposition. These techniques have been attempted with IDT-based polymers. Shin *et al*. investigated how the pre-aggregation of PIDT$_{C16}$-BT in solution affects their electronic performance[66]. They used a mixed solvent system of good and poor solvents for the polymer to induce aggregation. They found that picking the right solvent mixture would induce better pre-aggregation as determined by absorption spectroscopy. However, upon fabricating devices from the solution, thee expected improvement in electronic performance was not observed. Another group, Chen *et al*. developed a method to improve the annealing of PIDT$_{C16}$-BT films by incorporating a high boiling point solvent into the solution prior to spin-coating. Typically, thermal annealing for PIDT$_{C16}$-BT does not affect film morphology; the chains do not relax any more than at room temperature because the glass transition is below room temperature, and they appear to be already at a low energetic state. However, by thermally annealing the films with small amounts of solvent still in the film, the evaporating solvent created more space for the films to move around and reduce energetic disorder. The result was improved aggregation determined by absorption spectroscopy which gave way to improved charge transport determined by transistor measurements. There remains work to be done in understanding the aggregates that form in solution that will lead to the ordered domains seen in the film, to better tune the electronic performance.

Chapter 2. Experimental Methods

2.1 Particle Scattering

The potential of X-rays to probe atomic structures was realized when Max von Laue, alongside Friedrich and Knipping, discovered X-ray diffraction by crystals in 1912. Their experiment showed that crystals could act as a diffraction grating for X-rays, implying that X-rays are electromagnetic waves with wavelengths on the order of interatomic distancess[67]. This discovery led William Henry Bragg and William Lawrence Bragg to develop Bragg's Law in 1913, which provides a simple equation relating the angle of incidence and the lattice spacing of crystals to the wavelength of the X-rays[68]. Over the 20th century, improvements in X-ray sources, detectors, and computational methods expanded X-ray scattering applications. Dorothy Crowfoot Hodgkin famously used X-ray crystallography to determine the structures of vital biochemical substances like penicillin and vitamin B12, for which she received the Nobel Prize in Chemistry in 1964[69].

Neutrons were discovered by James Chadwick in 1932. Unlike X-rays, neutrons do not experience interactions with atomic electrons, allowing them to penetrate deeply into materials and interact with the nuclei[70]. The first significant use of neutron scattering began with the advent of nuclear reactors in the 1940s, which served as powerful neutron sources. This development significantly enhanced the study of atomic and molecular structures using neutrons[71]. Clifford Shull and Ernest Wollan at Oak Ridge National Laboratory pioneered various neutron scattering techniques, providing insights into the arrangement and dynamics of atoms in solids[72]. These techniques proved essential for studying materials with complex light-element compositions and magnetic properties. Today, neutron scattering is used in material science, chemistry, physics, and biology, facilitated by advanced reactors and spallation sources providing intense neutron beams.

This technique is indispensable for understanding the structure and dynamics of complex systems at the atomic and microscale.

2.1.1 Basic Theory

Neutron and X-ray scattering are nondestructive characterization methods that can provide information about the arrangement and dynamics of materials at various length and time scales. Depending on the region of interest, one can probe from the crystal lattice molecular arrangements on the order of Angstroms to large aggregates in a morphology such as nanowires on the order of hundreds of microns. The major difference between X-rays and neutrons from a scattering

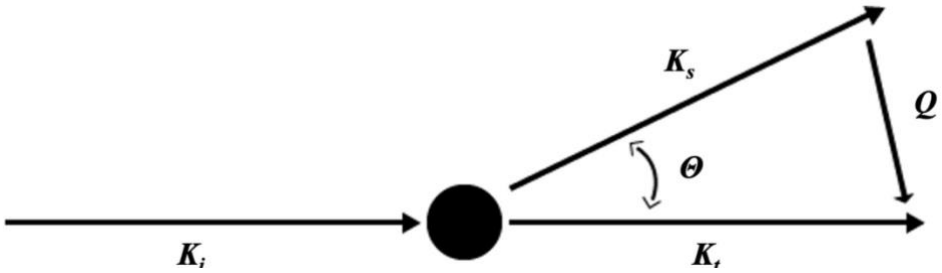

Figure 2-1: Interaction between incident beam and scattering object.

perspective is the degree to which they interact with the atoms of a material. While X-rays interact with the electron shell that occupies most of the volume in an atom, neutrons only interact with the nuclei. In an experiment, particles are directed at a sample with an incident momentum, K_i, and either interact with the atoms in the material or pass through. A schematic of this interaction is shown on Figure 2-1, where K_s is the scattered particle beam, K_t is the transmitted beam, Θ is the scattering angle and Q is the scattering vector. The interaction between the incident particle beam and the sample is a function of the type of atom or nuclei, the dynamics of the atoms and the arrangement of atoms in the material. The interaction with an atom causes a change in the direction and energy of the neutrons or X-rays, which can be detected and transformed into scattering vectors. This work utilizes small angle neutron scattering (SANS), small angle X-ray scattering (SAXS), wide angle X-ray scattering (WAXS), and grazing-incidence wide angle X-ray Scattering

(GIWAXS). These are all elastic scattering techniques in which the kinetic energy exchange between scattering particles and sample is assumed negligible, so that only the direction change of the scattered particle is relevant. The particle-sample interaction then is a function only of the atom type and arrangement. The magnitude of the incident beam vector is inversely proportional to its wavelength, λ. Due to the elastic nature of the scattering, the magnitude of K_i equals the magnitude of K_s. Q is a vector in reciprocal space, in units of A^{-1}. The relationship with real space is given by Bragg's law. This leads to the following equation for Q.

$$K_s - K_t = |Q| = \frac{4\pi}{\lambda} Sin\left(\frac{\theta}{2}\right) = \frac{2\pi n}{d}$$

2-1

This equation relates the reciprocal space Q vector with the real-space distance d. In addition to the assumption of negligible energy transfer, there are two more assumptions that this definition of scattering makes. (1) the scattering beam only accounts for a small portion of the incident beam (Born approximation), and (2) multiple scattering is negligible[73]. In a scattering experiment, the number of particles at distance Q from the transmission beam are detected in a two-dimensional space which is then integrated and reduced using background, sample thickness and empty cell data into an absolute scattering intensity profile $I(Q)$. Features in a material will cause an increase in the intensity at different length scales. The total scattering intensity can be broken down into the following Equation[74,75]:

$$I(Q) = \phi\, \Delta\rho^2\, V\, P(Q)\, S(Q)$$

2-2

where ϕ is the scale or volume fraction of scattering domains in the sample, V is the volume of the scattering domain, $\Delta\rho^2$ is the scattering contrast, or the difference in scattering length density between components in the system, $P(Q)$ is the form factor, which includes information about the

shape of the scattering domain, and $S(Q)$ is the structure factor which includes information about spatial correlations between domains distributed throughout the sample. The presence of structural features at a given length scale will cause an increase in the scattering signal at the corresponding Q value to that length scale, which is what give rise to the curves of $P(Q)$ and $S(Q)$.

The scattering contrast $\Delta\rho^2$ in equation 2-2 arises because scattering particles interact with atoms of different elements to different degrees. The degree to which an atom will interact with an incident beam of particles can be described by the scattering cross section, which is expressed in units of area. It represents the effective surface area seen by the incident particle (X-ray or neutron), and as such, is a measure of the probability that an interaction will occur between the particle and the atom. The cross section can be calculated theoretically using various methods, including quantum mechanics and classical electromagnetism. It can also be measured experimentally using techniques such as X-ray scattering spectroscopy. For X-rays, which interact with the electron cloud, the electron density around the nucleus of an atom is directly correlated with the scattering cross section. Because of this, as you increase the size of the atom and go up in atomic number, you tend to see an increase in electron density and therefore an increase in scattering cross section.

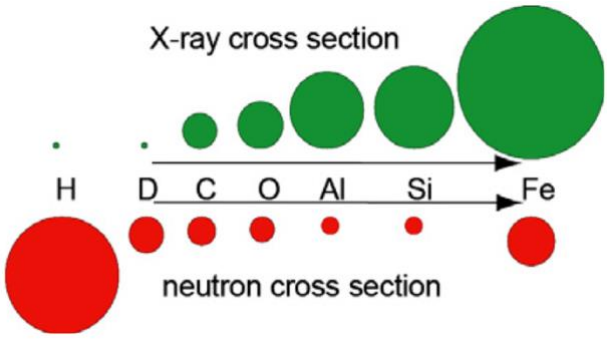

Figure 2-2: Scattering cross section comparison for X-rays and Neutrons for select elements. Reproduced from Ref .

Unlike X-rays whose interaction with atoms follows a periodic trend with increasing electron density, the degree of interaction between neutrons and atomic nuclei is random across atomic

size. A representation of relative sizes of scattering cross sections for X-rays and neutrons is shown in Figure 2-2.

As shown by the figure, it is more probable for a neutron to hit hydrogen than deuterium. Hydrogen has a total scattering cross section of 82.02 * 10^{-24} cm^2 while deuterium's is 7.64 * 10^{-24} cm^2. The scattering contrast places constraints on the samples that one can perform scattering on because there must be a difference in scattering cross section between the matrix or solvent and the sample. At the same time, that property can be used as an advantage to visualize only specific portions of the sample. For example, in neutron scattering, different components of a blend can be "hidden" from the neutron scattering intensity profile by deuterating those components to match the matrix or background. This is known as contrast variation neutron scattering (CV-NS), and it allows probing specific phases within a bulk sample. CV-NS can capture the bulk morphology at length scales ranging from 1 nm to 10 μm by replacing the hydrogen atoms of one phase with deuterium to create sufficient contrast between the polymeric components. Changing hydrogen atoms to deuterium atoms does not significantly alter the structural behavior of polymers. Additionally, neutron scattering has the advantage of being able to scatter from almost any solvent and material, whereas that is not the case for X-ray scattering. Certain atoms such as halogens are strong X-ray absorbers, limiting the use of halogenated solvents. Also, there is no way to change the chemical makeup of a scattering sample to create X-ray scattering contrast without significantly altering its chemical and structural behavior. Works in the literature have demonstrated how CV-NS can be useful for understanding CP structure in both the solution and the solid state. Researchers have been able to define the thermodynamics in polymer blends by extracting the Flory-Huggins parameter.[76] Others have been able to capture the mixing of the amorphous phases between the crystalline regimes.[77]

2.1.2 Instrumentation

A typical scattering experiment requires: (1) source for the particles (2) monochromator to make the particles of the same wavelength, (3) collimators to shape the beam, (4) sample stage, and (5) detector to capture the scattered particles as a function of Q[78]. For each of the techniques used in this work, the experimental setup keeps to those essentials. Each technique differs either in the type of particles used or geometry, so the instrumentation differs to match.

Particle Sources and Beam Modifiers

For X-rays, sources can come in the form of sealed X-ray tubes in which electrons are accelerated across a potential and their subsequent impact into the cathode material generates X-rays[79]. These X-ray sources are of moderate intensity and are commonly employed in university

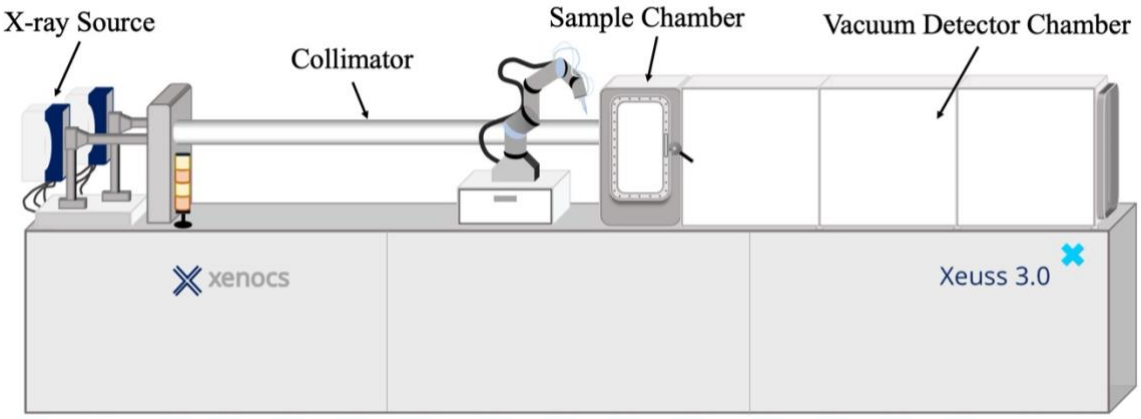

Figure 2-3: Schematic of Xeuss 3.0 X-ray scattering instrument at use at the University of Washington. Picture courtesy of Maria Politi.

laboratories. This work presents data obtained using one such source and instrument which is manufactured by Xenocs (Grenoble, France) (Figure 2-3) and used at the University of Washington. X-rays can also be produced in much higher intensities at synchrotron radiation sources which are a type of particle accelerator that produces intense beams of X-rays[80]. Usually, these are required when a more powerful beam of light is necessary to image samples and can be accessed through grant proposals or collaborations. This work presents data obtained at the

Stanford Synchrotron Radiation Lightsource (SSRL). Neutrons do not typically have a commercially available source because neutrons are more difficult to generate, and their sources are most commonly nuclear reactors. To perform neutron scattering experiments, nuclear reactors are maintained specifically for research such as the NIST Center for Neutron Research (NCNR), which accepts proposals for experiments utilizing neutrons.

The primary function of collimation is to shape and direct the particle beam onto the sample, ensuring that the particle beam is well defined and to reduce background scattering. Circular pinhole collimation is commonly used, where the neutron beam passes through a series of circular apertures to create a beam with a well-defined circular cross section. The collimation system is designed to minimize the divergence of the neutron beam, ensuring that the particles incident on the sample are nearly parallel. Monochromators ensure that the particles are the same speed or wavelength. From equation 2-1, the *Q* vector is inversely proportional to the wavelength of incident particles, so if there is a wide distribution of wavelengths, the structural features will be broadened and more difficult to detect. X-ray and neutron collimators commonly take the form of slits stationed throughout the beam path that tailor the beam cross section before it hits the sample. Monochromators for X-rays are usually single crystal reflectors that diffract specific wavelengths of radiation[81]. Monochromators for neutrons are usually spaced choppers that are timed to only allow neutrons of a specific velocity to continue through, and in this way, narrow the wavelength of those particles in the beam.

Instrument Geometries

The type of scattering geometry (small angle vs wide angle, and transmission vs grazing-incidence) indicates the length scale of the structures being determined and the configuration of the samples. Equation 2-1 relates the *Q* vector to the real-space distance *d* inversely. The smaller

the angle of scattering, the larger the structures that are being investigated. Small angle X-ray and neutron scattering observes structures from tens to hundreds of nanometers. Wide angle X-ray scattering probes atomic distances in the single nanometers and angstroms. In the field of polymers this equates to small angle scattering probing chain conformations and aggregate structures such as nanowires. Wide angle scattering probes the crystalline and lamellar spacing of polymer crystals and chains. Much of the data presented in this work including WAXS, SAXS and SANS data was collected using a collimated transmission configuration. To capture all angles from very small (0.001 $Å^{-1}$) to very wide (3 $Å^{-1}$), the sample and detector chamber is cleverly constructed as shown in Figure 2-4. The detector is designed to move along the axis of the scattered beam to capture the

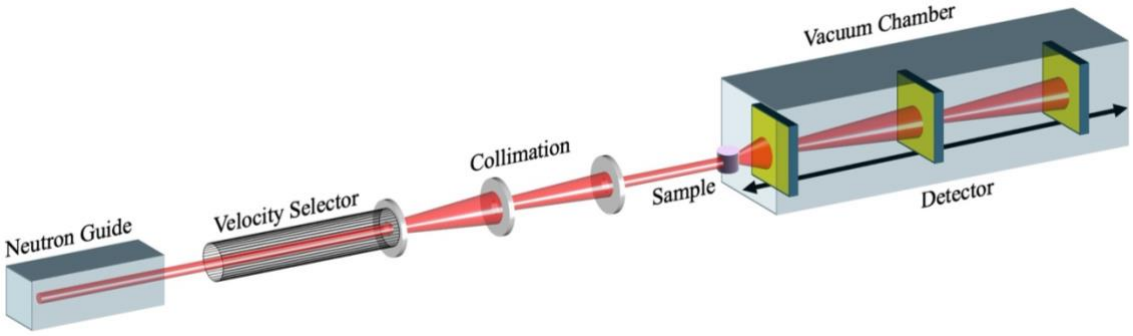

Figure 2-4: Typical SANS Instrument setup. The detector is not 3 separate detectors, but one single detector that moves along an axis parallel to the scattered beam to capture wider and smaller angles depending on the distance from the sample.

entire range of angles depending on its proximity to the sample. Additionally, sample stages are often constructed to alter parameters such as temperature and humidity. Some stages can perform mechanical deformation or sonication on the samples as they are being measured[82].

GIWAXS, in contrast to the other techniques which measure scattering after the beam passes through the sample (transmission), uses a grazing-incidence geometry, where the X-ray beam hits the sample at a very shallow angle, typically less than 1° (Figure 2-5)[83]. Because of this, the effective scattering volume is greater than in WAXS, resulting in stronger signals from difficult to detect crystal spacing in polymers. GIWAXS is specifically designed to study thin films,

surfaces, and interfaces, and is particularly useful for characterizing the structure of materials in two dimensions[84]. It can obtain information on how the structures orient themselves with respect

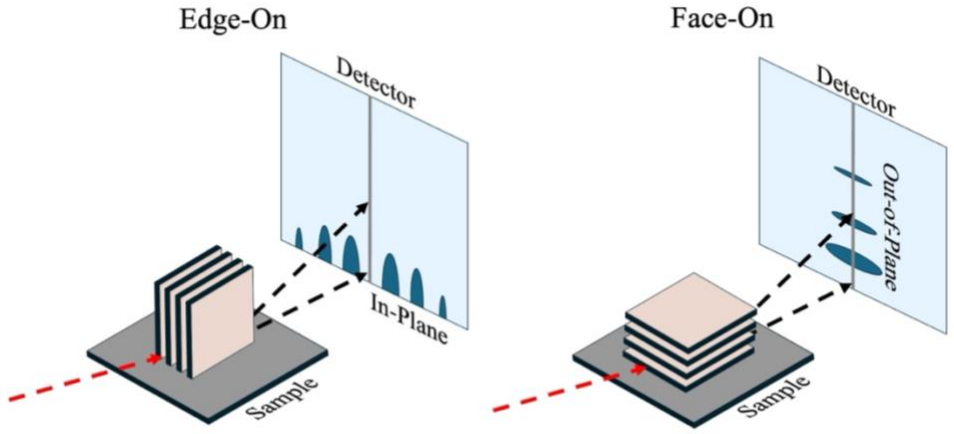

Figure 2-5: Schematic of grazing-incidence geometry used in GIWAXS showing edge-on and face-on lamellar geometries and their respective representative plane scattering.

to the film plane, which is very useful for understanding interfacial interactions in thin film electronic devices. Figure 2-5 shows how the alignment of lamellar sheets with respect to the film plane can be discovered from the 2-dimensional scattering profile on the detector. If the lamellae orient themselves in an "edge-on" fashion, then the scattering peaks for the lamellae will appear in the in-plane angle. If the lamellae are stacked and parallel with the plane, then their scattering peaks will appear in the out-of-plane angle[84]. In this way, the preferred orientation of polymer crystals and lamellae can be determined in their films.

2.1.3 Data Analysis and selected Models

Small Angle Scattering

During scattering experiments, data is collected in a 2D detector and in small angle scattering is typically integrated azimuthally to obtain a 1D profile. The factors due to the instrument such as background radiation and neutron or X-ray flux can be normalized in the data. Sample holder or capillary scattering and sample thickness are further corrected for. This leaves the absolute scattering intensity as a function of the form and structure factors, $I(P(Q)S(Q))$.

Structural information can be derived from scattering profiles in two ways: (1) I vs Q relationships at high and low ranges of *Q*; (2) fitting carefully selected models to the profiles. An example of the first method is the determination of the characteristic size of a polymer molecule, its radius of gyration, R_g. The relationship between the radius of gyration and the form factor in the scattering intensity is given by

$$P(Q) = Nexp(-\frac{Q^2 R_g^2}{3})$$

2-3

where *N* is the degree of polymerization. This equation is only applicable in the very small region of *Q* when $Q * Rg < 1$ and when *N* is known. By fitting the relationship to the region of the scattering intensity that follows a Q^{-2} dependance, the radius of gyration of the scattered polymer can be determined. In a similar fashion, the predicted scattering from shapes such as spheres and cylinders which would represent globular aggregates and rods, respectively, are represented by models that are fit over the entire scattering profile. The simplest model used is a sphere, for which the following equation has been derived.

$$I(Q) = \frac{scale}{V}\left[3V(\Delta\rho)\frac{\sin(qr) - qr\cos(qr)}{(qr)^3}\right]^2$$

2-4

In equation 2-4, *r* is the radius of the sphere and *V* is the volume of the sphere. Figure 2-6 shows

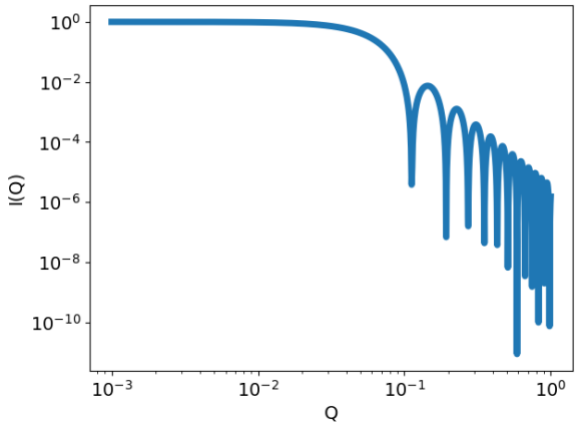

Figure 2-6: Plot of Equation 2-4 with sphere radius of 40

a plot of the sphere model. A more common model used with conjugated polymers is the parallelepiped which has been shown to model well the intensity profile given by P3HT nanofibers. The parallelopiped is a rectangular prism where *a*, *b* and *c* represent the dimensions of the parallelepiped shape, and is modeled by the equation:

$$P(Q) = \frac{2}{\pi}\int_0^{2\pi}\int_0^{2\pi}\left[\left(\frac{\sin\left(QAsin(a)\cos(b)\right)}{QAsin(a)\cos(b)}\right)\left(\frac{\sin\left(QBsin(a)\cos(b)\right)}{QBsin(a)\cos(b)}\right)\left(\frac{\sin\left(QC\cos(a)\right)}{QCcos(a)}\right)\right]^2 \sin(a)\,\delta a\delta B \qquad 2\text{-}5$$

Models and slope relationships are used to elucidate both the structures of the shapes in the blends and the sizes of those shapes. Additional models that are used throughout this work can be found in Appendix A[85].

Wide Angle Scattering

In the wide-angle regime, the features observed are of very small scale. Small enough that structures such as chains, spherical aggregates, etc. which are characterized by from factors *(P(Q))*, are not visualized. What is found at that scale are interatomic distances such as crystal and lamellar spacing. These distances give rise to structure factors (*S(Q)*) which manifest as peaks in the 1-

dimensional profile. Fully amorphous materials (e.g. PS) will show broad peaks that correspond to polydisperse correlation distances within the material. Semi-crystalline materials will display a combination of broad peaks from the amorphous phase and sharper peaks from the crystalline phase. An example is the wide-angle scattering profile of P3HT. In it, various crystalline peaks appear as shown by Figure 2-7[86]. The peaks at Q-values of approximately 0.35 and 1.7 $Å^{-1}$ correspond to the lamellar and pi-stacking distances of the crystal structure, respectively. By converting these Q-values into real space using equation 2-1, the crystal spacing can be extracted.

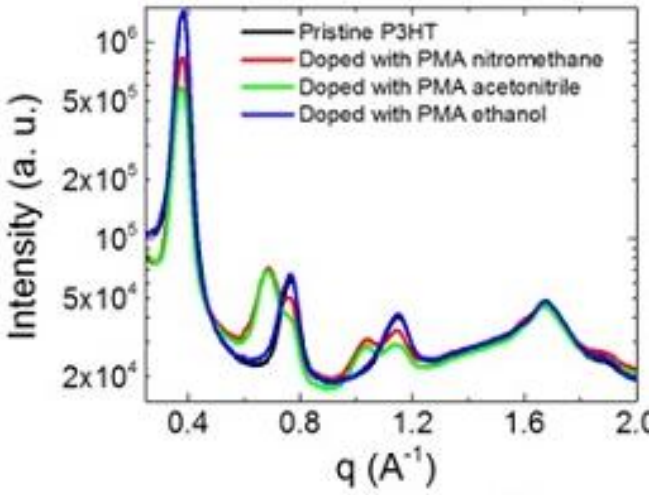

Figure 2-7: Out-of-plane linecut of GIWAXS of P3HT at various degrees of doping. Reproduced from Benavides *et al.*

Additional information about the nature of the crystalline regimes is contained within the peak characteristics. For example, the height of each of these peaks corresponds to the degree of crystallization in their respective directions. By comparing the relative heights of the lamellar and pi-stacking peaks across different samples, one can understand the preferred crystallization direction within a material. Additionally, the width of the peaks can be correlated to crystal properties such as crystallite size or coherence length[87]. It is important to note that form factors are not limited to the small-angle region and structure factors are not limited to the wide-angle

region. For example, in block copolymers, micelles often form. The micelles are spherical in shape and show a sloping profile that is like the one in Figure 2-6. Additionally, the micelles can arrange themselves in a repeated crystal-lattice type pattern. The result is peaks in the small angle region with a characteristic spacing related to the distance between arranged micelles[88].

2.2 Field Effect Mobility Measurements

2.2.1 Basic Theory

Field-effect mobility (μ) measures how quickly charge carriers (electrons or holes) can move through a semiconductor material under the influence of an electric field. It is a fundamental property that influences the performance of electronic devices, affecting their speed and efficiency[89]. In a field-effect transistor (FET), the mobility of the active layer can be measured

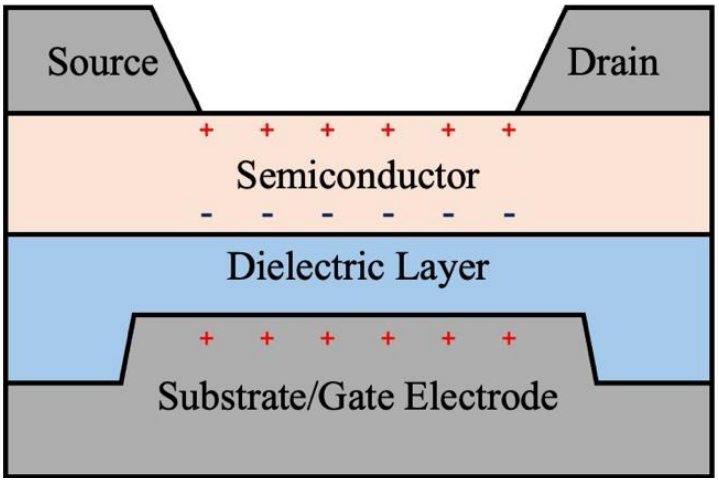

Figure 2-8: Schematic of an organic field effect transistor in top-contact bottom-gate configuration. The red charges in the gate electrode indicate a positive potential, which attracts negative charges to the bottom of the semiconductor, inducing a conductive layer between drain and source of positive charges (electron holes).

within the channel between source and drain terminals, under the gate (Figure 2-8). When a voltage is applied to the gate, it creates an electric field that modulates the conductivity of the channel by attracting charge carriers to the semiconductor/dielectric layer interface. This is what is known as the field effect. The ability of carriers to move through the channel material when a drain-source

voltage is applied is what is measured as mobility[90]. Several factors can affect the mobility in semiconductors. High interconnectivity between conducting domains and general isotropy in a material improves mobility. In certain instances, especially in CP, anisotropy that aids alignment in the direction of the OFET channel can also aid in increasing mobility[91]. On the other hand, inhomogeneities in conducting domains reduces charge transport and impurities and defects can scatter charge carriers, reducing mobility. There are factors outside of the material properties that may affect the measure field mobility. High carrier concentrations brought on by excessive doping or charge injection can lead to increased carrier-carrier scattering. At high electric fields, the carrier velocity may saturate due to increased scattering events, a phenomenon known as velocity saturation which is used as an advantage in measuring saturation mobility.

Mobility can be experimentally determined by directly measuring the current-voltage characteristics of a field-effect transistor. This measurement involves calculating the slope of the linear region of the transistor's transfer characteristics and applying the fundamental MOSFET operation equations which are covered in the analysis section below.[92] Understanding and optimizing field-effect mobility is essential for designing efficient electronic devices. Higher mobility allows for faster switching speeds in transistors and lower power consumption, crucial for high-performance computing and mobile devices. Measuring the field effect mobility in CP helps researchers understand not only the electronic performance of a given polymer structure, but fundamentally aids in understanding polymer packing and morphology.

2.2.2 Device Fabrication

There are many architectures of FET, but the most common one used for organic field effect transistors (OFET) is the one shown in Figure 2-8. It consists of 4 active layers: the bottom is a conductive electrode that serves as the gate. This is followed by a layer that serves as an

insulator to prevent charges from jumping from gate to active layer. After that is the active layer of the semiconductor in question, and lastly is the electrodes that serve as the source and drain charge injectors[93]. The process of fabricating an OFET follows the steps necessary to assemble each of these films on top of each other.

Starting from the bottom, the gate electrode and the dielectric layer are usually commercially available in the form of heavily doped single crystal silicon with a thermal oxide layer of silicon dioxide grown on top of it. Since these wafers are widely available[94], the single crystal growth, doping and thermal processes required to generate the oxide layer will not be covered in this work. On top of this layer, the active layer is spin coated. Typically, there are challenges associated with creating homogenous thin films of conjugated polymers on wafers. The first challenge is that of surface interaction. The surface of the silicon dioxide layer is decorated with hydroxyl groups, which are polar in nature. In contrast, conjugated polymers are decorated with alkyl side chains to aid in dissolving them and are nonpolar. The result is that hydrophobic conjugated polymers and their solvents do not interact well with the hydrophilic surface of the SiO_2. If CP are spin-coated on the pristine surface, they most likely spin off and if they do manage to adsorb to the SiO_2, the film will present holes and inhomogeneities. To solve this issue, the field has developed surface modifications with which to transform the hydrophilic surface into a hydrophobic one. Alkylsilanes are molecules developed to modify hydrophilic surfaces with alkyl chains[95,96]. They are composed of a nonpolar alkyl side chain connected to a silicon atom which has also chlorine groups that are very reactive to polar hydroxyl groups. When these chemicals are applied to pristine oxide surfaces, the Cl groups react with the hydrogen on the oxide layer, bonding the silicon atom, and the alkyl chain attached to it to the oxygen atoms of the oxide layer.

Figure 2-9 shows this process and the resulting structure[97]. Because this reaction is limited to only the surface atoms of the oxide layer, they form self-assembled monolayers (SAM). These thin layers do not get in the way of the OFET function and functionalize the oxide layer so that nonpolar

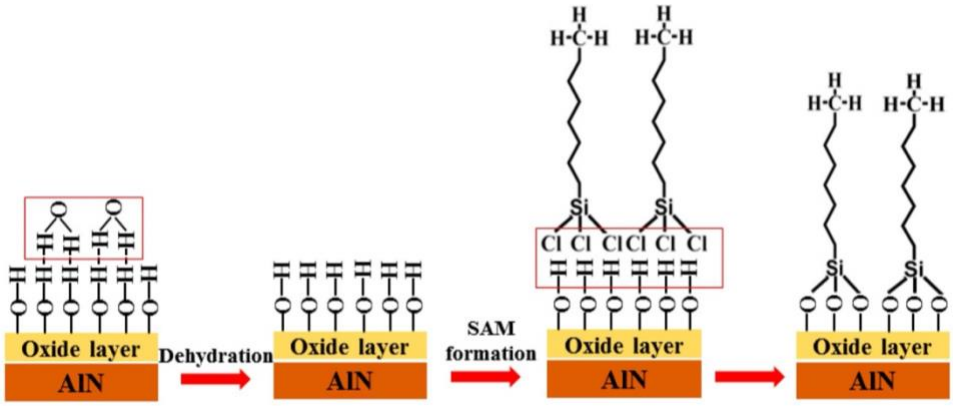

Figure 2-9: Diagram showing the modification of hydrophilic oxide layers by alkylsilanes to form hydrophobic self-assembled-monolayers (SAM).. Figure reproduced from Li *et al.*

solutions of CP can be spin coated into homogenous films to form an active layer. This work uses two different techniques to form an alkysilane monolayer. One uses vapor deposition to slowly form the layer on the oxide surface and the other uses solution spin-coating[98,99]. Both methods are covered more in detail in the methods sections of Chapter 3.

On top of the SAM, the active layer is deposited as a thin film using spin-coating. The morphology, thickness and contact resistance between the active layer and the surface electrodes all impact the mobility of the completed OFET. Additionally, films can be thermally, and solvent annealed after deposition to alter their morphology to improve charge mobility. To isolate just the impact of the film morphology, the film parameters are optimized by changing spin-coating parameters such as CP concentration, type of solvent, and spin speed. This work presents 4 papers in which materials are used as the active layer for OFET fabrication, and for each one, the parameters of the films were optimized by methodically varying each of the tunable parameters to

obtain the best possible mobility. The last layer of the stack is the source and drain electrode layer. For all the OFETs fabricated in this work, this layer was formed by thermally evaporating gold and depositing it slowly on the active layer surface which was covered by masks that had holes in the shapes of the OFET channels.

2.2.3 Measurement and Analysis

Once the OFET is fabricated, it is tested in a nitrogen environment, usually a glovebox. The testing setup consists of two source-measuring units (SMU). One SMU is used to apply a potential between the source and the drain electrodes and measure current between them. The other SMU is used to apply a potential between the gate and the drain electrodes. Typically, two types of measurements are made that result in characteristic transistor curves. The first type generates output curves which are obtained by sweeping the voltage between source and drain (V_{SD}) at a fixed gate voltage (V_G) and measuring the current between source and drain (I_{SD}). This type of measurement is useful for getting an idea for the threshold gate voltage and it informs of the saturation regime of the OFET. The saturation regime occurs when increasing V_{SD} no longer increases I_{SD}. This happens because a high V_{SD} causes a pinch-off point in the conducting region created by the field effect. Within this pinch-off point, electron velocity is limited by scattering events. This region can be clearly seen in Figure 2-10 as the region in which increasing source-drain voltage no longer increases current. The saturation and linear regimes display slightly different electron behavior, and so will have differing mobilities even in the same device. The other characteristic curve is called the transfer curve and can be obtained by sweeping the gate-source voltage at a constant drain-source voltage. This is usually set up to satisfy the conditions of either the linear regime or the saturation regime. The linear regime is the regime where an increase in V_{SD} correlates with increase in I_{SD}. Mathematically, the linear regime occurs when (V_G-V_T) >>

V_{SD} and the saturation regime when (V_G-V_T) < V_{SD}. In Figure 2-10, for the transfer curve, a high V_{SD} is selected so that the mobility extracted is a saturation regime mobility.

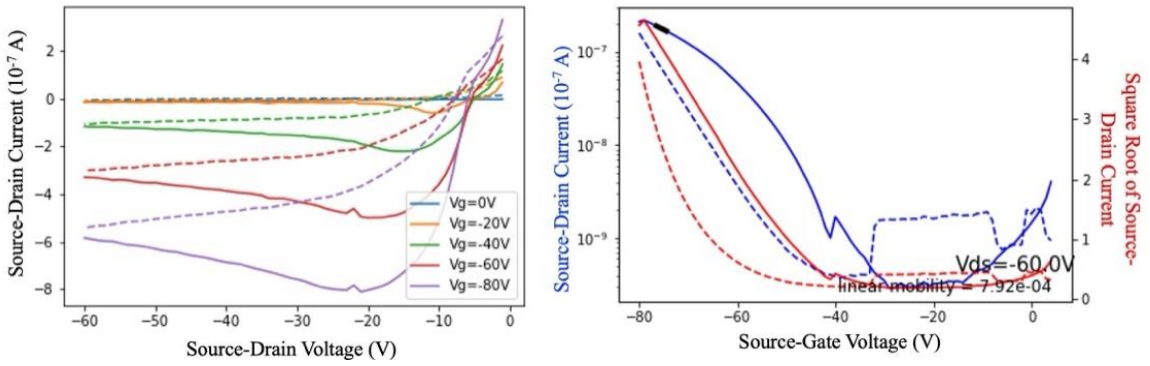

Figure 2-10: Characteristic curves of an OFET measurement: (left) output curves and (right) transfer curves.

Once the characteristic curves are measured, the mobility can be extracted using the following relationship, which is only valid in the saturation regime:

$$I_{SD} = \frac{WC\mu}{2L}(V_G - V_T)^2$$

2-6

In this equation, W and L are the channel width and length respectively, and C is the capacitance per unit area of the insulator, which for SiO_2 is 10 nF·cm^{-2}. By solving for mobility and re-equating for slope, one gets:

$$\mu_{Sat} = \left(\frac{2L}{WC}\right)\left(\frac{\delta\sqrt{I_{SD}}}{\delta V_G}\right)^2$$

2-7

Thus, the mobility can be extracted by fitting a linear slope of the square root of transfer curve in the saturation regime. There is an equivalent equation and derivation for the linear regime, but this work primarily uses the saturation mobility as a figure of merit. In addition to the charge mobility, the threshold voltage (V_T) is easy to extract using either the output curves or extrapolating the linear fit of the linear region in the transfer curve to the x-intersection. Lastly, on/off ratio (I_{on}/I_{off})

is a ratio of the current when the transistor is on to when it is on. It can be calculated by measuring the highest and lowest currents achieved in the transfer curve.

2.3 Ultraviolet-Visible Absorption Spectroscopy

2.3.1 Basic Theory

Ultraviolet-visible light absorption spectroscopy (UV-Vis) is a widely used analytical technique that measures the absorbance of light by a sample across the ultraviolet and visible regions of the electromagnetic spectrum. This technique is based on the principle that molecules absorb light energy, which excites their electrons from the ground state to higher energy states. The energy required for this excitation is specific to the molecular structure and bonding environment of the sample[100,101]. The UV-Vis region of the electromagnetic spectrum spans from approximately 100 to 780 nanometers (nm), with shorter wavelengths corresponding to higher energy. The technique involves measuring the absorbance of light by a sample as a function of wavelength, which is typically plotted as a spectrum. The absorbance is calculated using the Beer-Lambert Law, which relates the absorbance (A) to the concentration of the absorbing species (c), the path length of the sample (b), and the molar absorption coefficient (ε)[102].

$$A = \varepsilon bc \qquad \text{2-8}$$

The feature peaks of UV-Vis spectra occur because of optical transitions. Optical transitions refer to the electronic transitions that occur within a molecule when it absorbs light energy. These transitions involve the promotion of electrons from a lower energy state to a higher energy state, resulting in the absorption of light at specific wavelengths. There are several types of optical transitions that can occur in molecules. π - π^* transitions involve the promotion of an electron from a π bonding orbital to a π^* antibonding orbital. n - π^* transitions involve the

promotion of an electron from a non-bonding (n) orbital to a π* antibonding molecular orbital. σ - σ* transitions involve the promotion of an electron from a σ bonding molecular orbital to a σ* antibonding molecular orbital. Additionally, several factors can affect the optical transitions in a molecule. The molecular structure, including the presence of unsaturated bonds, lone pairs, and electron-donating or electron-accepting groups, can influence the types of optical transitions that occur. The solvent in which the molecule is dissolved can affect the optical transitions. For example, polar solvents can cause a blue shift (shorter wavelength) in the absorption spectrum, and non-polar solvents can cause a red shift (longer wavelength). Lastly, the presence of conjugated double bonds in a molecule can lower the band gap, leading to absorption at longer wavelengths. Understanding optical transitions is crucial in UV-Vis, as they determine the absorption spectrum of a molecule. The absorption spectrum can provide valuable information about the structure and properties of a molecule, including the presence of certain functional groups, the degree of conjugation, and the energy levels of the molecular orbitals.

The instrumentation used in UV-Vis spectroscopy typically consists of a light source, a monochromator or diffraction grating to select specific wavelengths, a sample holder or cuvette, and a detector to measure the transmitted light. The choice of cuvette material is important, as it can affect the absorbance cutoff, with quartz being a common choice due to its low absorbance cutoff of around 160 nm.

2.3.2 Model Fitting and Analysis

A typical CP UV-Vis spectra is shown in Figure 2-11. For many CP systems, specific

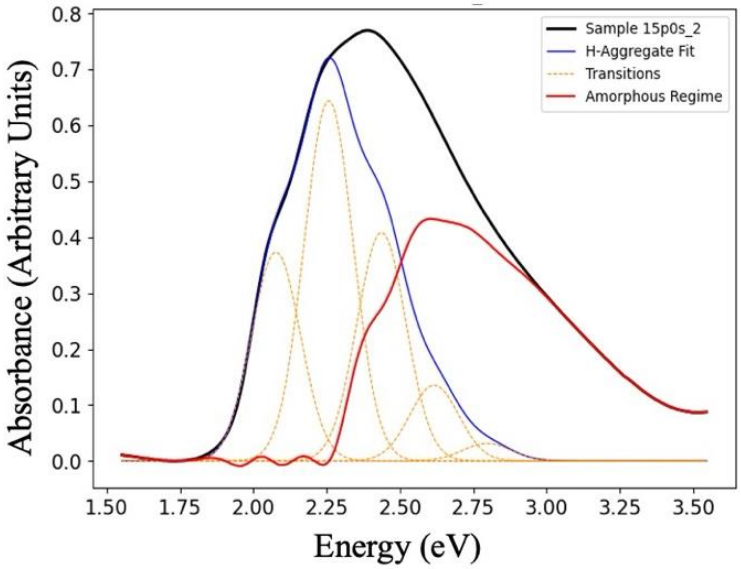

Figure 2-11: UV-Vis Spectra of a thin film of P3HT on glass. Additionally, an H-aggregate fit is shown representing the electronic transitions. The x-axis is usually wavelength in nm but was converted to energy in this representation.

models are designed to capture their vibronic transitions and gleam structural and order information from them. Shown in Figure 2-11, P3HT can be fit with a model developed by Spano *et al*. which represents a weakly interacting chains H-aggregate model from which important chain ordering parameters can be derived[103,104]. Other polymer systems can be analyzed by observing parameters such as the wavelength at maximum absorption,$\lambda_{max,}$ which indicates the degree of conjugation or that a CP may have. In the figure above, the model is composed of various gaussian curves, each of which represents one optical transition. Another parameter that is investigated in conjugated polymer is the ratio of the peak heights of the 0-0 and 0-1 transitions. This ratio is directly related with the exciton band width which can provide information about the general degree of chain disorder.[105,106]

Chapter 3. Using Electronic Properties of Conjugated Polymers to Understand their Structure-Morphology Relationships.

Field effect mobility and conductivity are important figures of merit commonly used to assess the electronic performance of semiconducting materials. Often, studies published in the field involve designing and synthesizing novel conjugated polymers (CP) and then extensively characterizing their properties including their electronic properties. The morphological characterization of the novel materials is used in these studies to explain the physical characteristics such as mechanical behavior and electronic performance. In contrast to that are studies that vary molecular structure or processing conditions in a known polymer system and use extensive characterization to gleam trends from the variation. These trends can then be used to understand more fundamental concepts of the structure-property relationships governing CP. This chapter visits three instances of using field effect mobility or conductivity to not only assess the electronic performance of the CP materials, but also to understand how their molecular structure impacts the morphology.

3.1 Using Particle Scattering and Conductivity to Determine the Impact of Weight Fraction and Solvent in Conjugated/Insulating Polymer blends.

This chapter section contains material from the following publication and the author would like to acknowledge the contributions of all coauthors:

Wolf, C. M.; **Guio, L**., Scheiwiller, S. C., O'Hara, R., Luscombe, C., Pozzo, L. D. Blend Morphology in Polythiophene-Polystyrene Composites from Neutron and X-ray Scattering. Macromolecules 2021 54 (6), 2960-2978. DOI: 10.1021/acs.macromol.0c02512

Statement on Distribution of Work: The work done herein was a combination of efforts by Dr. Caitlyn Wolf, Dr. Sage Scheiwiller, and I. Specifically, I was responsible for the synthetic component of one polymer used in this work, collection of the conductivity data, WAXS analysis, and helping with SANS data collection. Dr Caitlyn Wolf and Dr. Sage Scheiwiller also collected SANS and WAXS data. Dr Caitlyn Wolf performed the SANS data analysis and is the first author of this paper. We also discussed ideas and conclusions from the data collaboratively prior to the writing of this paper.

3.1.1 Introduction

Although P3HT has many excellent properties for use in organic electronic devices, it has its limitations. One of those limitations is its instability in the real-world environment. P3HT is known to degrade readily under air and sunlight exposure. Hintz *et al.* investigated the various environmental factors that affected the stability of P3HT films using fluorescence quenching to track the quantity of degradation products over time.[107,108] They derived that the degradation process starts with exposure to UV light, followed by photooxidation when exposed to sources such as air and water. The result of oxidation and the generation of other degradation products leads to a decrease in device performance in OPV's and OFET's. Furthermore, P3HT has a trade-off in terms of properties. Kim *et al.* investigated the effect of changing the regioregularity of P3HT on the mechanical properties of the material. As the regioregularity goes up, so does the crystallinity of the P3HT material, making it much more brittle, prone to cracks and not durable.[109] However, that also comes with an increase in device performance as higher regioregularity leads to higher crystalline regions and long-range crystalline order. The result is a tradeoff between a good electronic device and a device that can resist mechanical stresses and stretch to adapt to the human skin.

One of the available strategies to combat the weaknesses of polymers is blending various polymers together. Blending polymers is a technique that polymer scientists have been using since polymers were first formulated. Most commonly polymers are dissolved in a solvent that can solubilize both and then cast. Making polymer blends can result in materials with properties from both component and new properties that result from the interaction between them. Blends are classified as either miscible, where polymer components are homogenously dispersed down to the

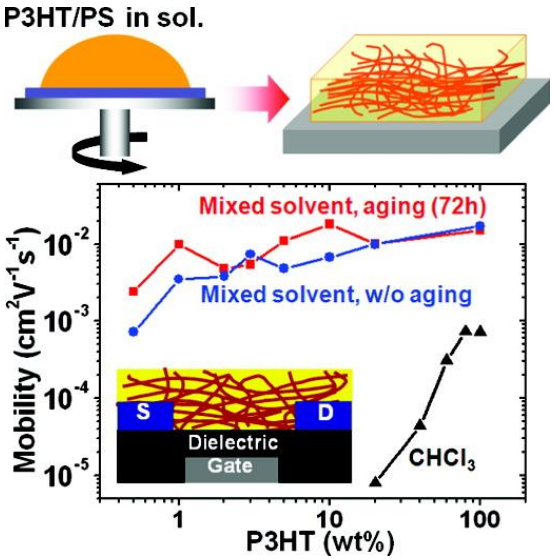

Figure 3-1: Improvement of OFET mobility of P3HT/PS blends using a marginal mixed solvent system to induce nanofiber formation.

molecular level, and immiscible where the two components form phase separated domains. Blends lie in a gradient between miscibility and immiscibility; where this is largely determines the interaction between them and the structures that are resulted from their phase segregation or lack thereof. The structures that form when polymer blends phase separate, like in pure polymers, give rise to the blend's macroscopic properties. To improve the environmental stability and mechanical durability of conjugated polymers, while keeping their electronic device abilities, researchers have investigated blends of CPs in a matrix of an insulating commodity polymer, such as polystyrene

or polyethylene. Goffri *et al*. blended high regioregularity P3HT with different types of commodity polymer to compare the effect of varying the matrix polymer. The group blended P3HT with commodity polymers of varying compatibility and crystallinity and measured their mobility using thin-film OFET devices. They found that they could maintain OFET mobility comparable to that of the neat P3HT by using amounts as low as 3 weight percent of conjugated polymer in the blends. They also found that blending the semicrystalline P3HT with amorphous polystyrene resulted in much lower hole mobilities than the semicrystalline polystyrene and polyethylene. They concluded that to maintain good charge mobility, the blends needed to consist of phase separating components that would allow the semiconducting component to form percolation networks. Lastly, they found that the best mobility came when there was also vertical phase separation, which is ideal for a thin film OFET device structure. Other researchers have similarly found success in maintaining good OFET performance by encouraging vertical phase separation, which enriches the surface of the active layer with the semiconducting material.[110]

Another successful strategy in introducing the electrical properties of the semiconducting CP into commodity polymer blends is creating an environment that leads to pre-aggregation and even nanowire formation of the CP in the solution state. Qiu *et al*. studied the influence of solvent quality on the final solid-state morphology in P3HT-PS blends. They discovered that, like in the neat films of CP, marginal solvents could be used to form P3HT nanofibers, which when dried in a thin film, assembled into networks dispersed in the PS matrix that still maintained device performance with a very low concentration of P3HT.[111] Han *et al*. also found that choosing a solvent with a high boiling point was useful for increasing the drying time of the blend and encouraging phase separation for improved devices.[112] The morphology of conjugated and insulating polymer blends directly impacts the electronic abilities of the material.

Ample research has been focused on improving material properties by creating blends. However, the morphological behavior of CP in these blends has not been completely understood. By investigating exactly how CP interact with the commodity polymer media and how processing conditions change the interactions, researchers will be able to tune parameters and improve the physical and electronic properties even further. There are numerous experiments focusing on P3HT/insulating polymer blends, with most studies focusing on creating thin films and testing their transistor performance. However, this figure of merit is useful only for the specific transistor type that is being tested. In fact, Hou *et al*. has shown that vertical phase separation aids in improved mobility only within 5-10 nm of the surface of the blend film. For this reason, it is important to investigate the morphology and the electrical properties of CP/insulating polymer blends within the bulk of the material and not just in very thin films. This is difficult to do with traditional characterization methods, which typically use photons and electrons to probe structures on the surface of materials. Probing bulk conformation also necessitates a technique that can distinguish polymer phases in the blends at multiple length scales.

In this paper, CV-SANS was used to characterize the bulk conformation and self-assembly behavior in polythiophene and polystyrene blends. For this chapter, the CV-SANS exploration is only sufficiently covered to understand the bulk conformation and relate it back to WAXS and the electronic characteristics. Polymers whose WAXS and Conductivity measurements are not used in this work are omitted for clarity. A set of semi-crystalline polythiophenes with differing chain packing properties were explored, including crystalline high regioregularity poly(3-hexylthiophene) (RRe-P3HT) and amorphous low regioregularity poly(3-hexylthiophene) (RRa-P3HT). The matrix polymer for all blends was an atactic (amorphous) PS. Solvents with a range of CP solubilities: toluene, chloroform, and bromobenzene, were used to understand the effect of

processing conditions on the final blend morphology in the solid-state. CV-SANS was first used to quantitatively define the CP structures formed in the matrix, such as nanofibers or globular aggregates. Wide-angle X-ray scattering (WAXS) was then used to determine the nature of crystalline phases within the blends. Finally, the bulk conformation was related back to the macroscopic performance of these materials by use of conductivity measurements.

3.1.2 Materials

A set of CP were purchased from Rieke Metals (Lincoln, NE USA): poly(3-dodecylthiophene) (P3DDT) (MW=39 kg mol-1, Đ=1.8, Product 4005-E), low regioregularity poly (3- hexylthiophene) (RRa-P3HT) (MW=63 kg mol-1, Đ=2.4, Product 4007), and high regioregularity poly(3- hexylthiophene) (RRe-P3HT-2) (MW=55 kg mol-1, Đ=2.4, Product 4002-EE). Hydrogenated polystyrene (PS-H8) (MW=278 kg mol-1, Đ=1.07, Product P8610-S) and fully deuterated polystyrene (PS-D8) (MW=305 kg mol-1, Đ=1.08, Product P19833-dPS) were purchased from Polymer Source (Dorval, Montreal, Quebec Canada). All polymers were used as received. For the preparation of solid samples, solvents of chloroform, toluene, and chlorobenzene were purchased from Fisher Chemical (Waltham, MA USA), bromobenzene was purchased form Aldrich Chemistry (St. Louis, MO USA), and fully deuterated toluene (toluene-D8) was purchased from Cambridge Isotope Laboratories, Inc. (Tewksbury, MA USA). All solvents were used as received. In addition to the purchase polymers, RRe-P3HT (MW=22.7 kg mol-1, Đ=1.2) was synthesized following literature procedure[113] with noted modifications:

Bromo(2-methylphenyl) bis(triphenylphosphine)nickel (II)

Nickel (II) Bromide (2.19 g, 10 mmol) and triphenylphosphine (5.25 g, 20 mmol) were added to a 3-neck flask with an attached condenser and dried under vacuum for 30 minutes. After drying, 15 mL anhydrous THF was added. The flask was brought to 70° C and the mixture was

refluxed for 2 h. Mg turnings (0.29 g, 12 mmol) were added to a Schlenk flask and flame dried under vacuum. After drying, 1 M 2-bromotoluene in anhydrous THF (10 mL, 10 mmol) was added dropwise to the Schlenk flask. The mixture was stirred for 1 h under darkness. The 3-neck flask was allowed to cool to RT and the Grignard solution was injected into it. The mixture was stirred for 20 minutes at RT and then quenched by pouring into methanol. The product was vacuum filtered with fine glass frit, washed with methanol, and dried under vacuum. ^{13}P NMR shifts: δ 21.97 (s, 2P)

High regioregularity Poly(3-hexylthiophene)

1,3-bis(diphenylphosphino)propane (41.25 mg, 0.05 mmol) and bromo(2-methylphenyl) bis(triphenylphosphine)nickel (II) (37.72 mg, 0.1 mmol) were added to a Schlenk flask, and dried under vacuum for 30 min. After drying, anhydrous THF (2 mL) was added, and the mixture was stirred for 2 h. 2-bromo-3-hexyl-5-iodothiophene (1.45 mL, 6.6 mmol) was added to a Schlenk flask and degassed under vacuum for 30 min. Anhydrous THF (66 mL) was added to the Schlenk flask, the flask was placed in an ice bath and 1.85 M isopropyl magnesium chloride in THF (3.24 mL, 6 mmol) was added dropwise over 30 min. Following addition, the flask was returned to RT, and stirred for 1 h under darkness. The catalyst mixture was injected rapidly to the monomer flask to start the polymerization. Immediately after injection, the flask was placed in an oil bath at 45C to prevent precipitation. The polymerization proceeded for 2 h. The polymerization was quenched with the addition of HCl (3 mL, 5 M). The polymer was precipitated into methanol (1000 mL) and collected by vacuum filtration. The polymer was purified using Soxhlet extraction with methanol, acetone, and hexanes. The polymer was extracted from the thimble with chloroform, then precipitated into methanol and collected via vacuum filtration. The polymer was dried under vacuum. ^{1}H NMR spectra were obtained on a Bruker AV-500 spectrometer using $CDCl_3$ as

solvent. Size exclusion chromatography (SEC) was performed using a Malvern Viscotek TDA 305 SEC with a UV and RI detector. Samples were run using THF as the eluent at a flow rate of 1 mL/min. The concentration of the polymer was 0.5 mg/mL. The molecular weight distribution is determined by SEC, and the M_n is obtained by NMR end-group analysis. Regioregularity was determined by comparing the ratio of integrations of the head-to-tail couplings against tail-to-tail and head-to-head couplings; these showed the polymers to have >99% regioregularity within the resolution of the NMR. 1H NMR Shifts: δ 7.43 (m, 2H), 7.24 (m, 2H), 6.98 (s, 1H), 2.80 (t, 2H (2H between the peaks at 2.8 and 2.61), J = 7.7 Hz), 2.61 (t, 2H (2H between the peaks at 2.8 and 2.61), J = 7.6), 2.49 (s, 3H), 1.71 (quint, 2H, J = 7.6 Hz), 1.48-1.38 (m, 2H), 1.37-1.30 (m, 4H), 0.91 (t, 3H, J = 7.2 Hz).

3.1.3 Methods

The complete sample preparation process for solid polythiophene-polystyrene blends is shown below in Figure 3-2. For each sample, a CP of either P3DDT, RRe-P3HT or RRa-P3HT was dissolved in solution with either PS-D8 or PS-H8 at a total polymer concentration of 50 mg/mL. The ratio of CP and PS varied to correspond to solid-state polythiophene concentrations. The fully deuterated PS-D8 was used to create sufficient contrast in samples that would be characterized using SANS. The solvents used were toluene, chloroform, and bromobenzene as they provided a range of solvent quality for the CPs. Toluene can be described as a moderate solvent for polythiophene, chloroform a good solvent, and bromobenzene an excellent solvent. These solutions were cast onto a watch glass on a hot plate at 50 °C to evaporate the solvent. Bromobenzene solutions took approximately 3 hours to dry, toluene solutions took approximately 30 minutes, and chloroform solutions took approximately 12 minutes. Additional residual solvent was removed by placing the sample in a 50 °C vacuum oven for 24 hours. Finally, the solid samples

were shaped with 2-3 cycles in a heat press at 150 °C, which was above the glass transition of the PS and below the melting temperature of RRe-P3HT. Precision metal shims were used as a spacer to ensure that any bubbles in the film would be removed, and the material would form a uniform

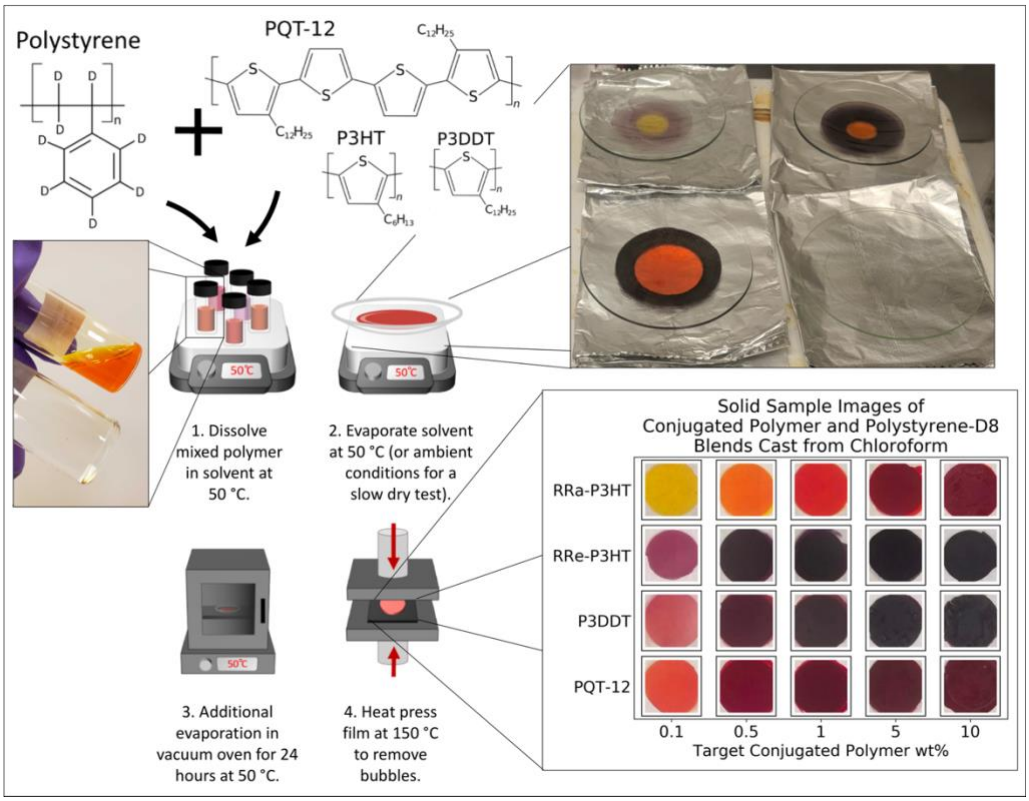

Figure 3-2: Sample preparation schematic for solid polymer blend films comprised of a CP with PS-D8 or PS-H8 (not shown). CPs used in this work included RRe-P3HT, RRa-P3HT and P3DDT. The concentration of CP in the solid blend was targeted between 0.1 – 50

disc with a thickness of 254 μm.

Small and Ultra-Small Angle Neutron Scattering

All SANS and USANS experiments were performed at the National Institute of Standards and Technology (NIST) Center for Neutron Research (NCNR) in Gaithersburg, MD. SANS data was collected using the NG-3 45m Very Small-Angle Neutron Scattering and the NG-7 30m Small-Angle Neutron Scattering instrument, both configured for a Q-range of 0.002 - 0.1 $Å^{-1}$. USANS data was collected using the BT-5 Ultra-Small-Angle Neutron Scattering instrument

configured for a Q-range of 0.00004 - 0.003 $Å^{-1}$. The NCNR SANS and USANS reduction macros[114] for Igor Pro were used to reduce the data, integrating 2D scattering images to 1D profiles, correcting for the instrument background, and to determine absolute scaling of scattering intensity. Further SANS/USANS analysis and modeling was performed using the SasView/sasmodels[115,116] and bumps[117] packages for Python. Solid samples were measured using titanium and cadmium sample frames that enabled the beam to pass through the sample only. Smearing of the USANS data for the solid samples was accounted for using the SasView/sasmodels[115,116] package, and so all USANS data for these samples is presented in the smeared form.

Small Angle Neutron Scattering Data Analysis

In multi-component systems, one can grab the scattering equation and define it with respect to the self- and cross-interaction terms between components[118,119]:

$$I(Q) = \Sigma_{i=1}^{N}[(\rho - \rho_0)^2 F_{ii}(Q)] + 2\,\Sigma_{i<j}\,[(\rho_i - \rho_0)(\rho_j - \rho_0)F_{ij}(Q)] \quad 3\text{-}1$$

where $F(Q)$ is the partial scattering function, and N is the number of components. In solid polymer blends, one can expect three potential sources for contribution to the overall scattering intensity that relate to (1) intrinsic PS-D8 density fluctuations, (2) isolated or 'free' CP chains and (3) phase aggregated or self-assembled CP structures (e.g., globular domains, nanofibers). Each of these contribute to the scattering intensity as they generate contrast with respect to the average PS-D8 SLD, ρ_0. To a first approximation, one can assume that the cross-interaction terms in the second part of equation 3-1 contribute negligibly to the total scattering intensity in comparison to the primary contributions that relate to the shape factors of each anticipated morphology. The cross terms only becomes significant to the intensity if the scattering domains are correlated.[119] This

would arise in our polymer blends if any of the structures contributing to the scattering intensity were dependent on another, e.g. if the positioning of aggregated or self-assembled CP structures were dependent on the position of the free polymer chains. However, in our samples we can expect these structures to be randomly distributed and independent of each other. Therefore, by applying a mass balance and removing the cross-term contributions, we generalize the scattering intensity for each sample as:

$$I(Q) = \phi_{CP}\Sigma_{k=1}^{K}[x_k I_{CP,k}(Q)] + (1-\phi_{CP})I_{PS}(Q) + background \quad 3\text{-}2$$

where x_k is the fraction of CPs present in form k of K total conformations and $\Sigma_{k=1}^{K} x_k = 1$, $I_{CP,k}(Q)$ is the scattering intensity due to conformation k (e.g. phase aggregated CP or free polymer chains), and $I_{PS}(Q)$ is the scattering intensity from the density fluctuations of the PS-D8 phase.

The PS-D8 contribution, $I_{PS}(Q)$, is well defined by the Guinier-Porod model[115,120,121] while the CP contribution, $\Sigma_{k=1}^{K}[x_k I_{CP,k}(Q)]$, was broken up into at most two contributions. Free polymer chains could not be identified from the scattering profiles, which suggests that phase separation dominates the morphology in most of these blends. It was possible, however, to model large-scale phase separation using spherical or ellipsoidal form factors for the globular domains and a long cylinder form factor for the nanofibers. Model names of 'sphere', 'ellipsoid', 'sphere+cylinder', and 'ellipsoid+cylinder' are used to indicate which form factors are included in the CP contribution while always maintaining a CP mass balance. While not explicitly stated in the naming convention, these combined models always include the intrinsic PS-D8 contribution as shown below. However, we note that there is no molecular justification for the specific form factors that were chosen (i.e. sphere vs. ellipsoid) to capture the globular domains of the conjugated

component. We simply used the simplest models that would accurately capture the shape and length scales of these globular domains. Therefore, in generalized terms, we will also refer to these fits as 'Globular Domains' or 'Globular Domains + Nanofibers'. To compare a common size parameter between the sphere and ellipsoid globular domains that are formed in the samples, we use the radius of gyration (R_g).

When fitting SANS and USANS data, the cylinder volume fraction of CP, ϕ_{CP} was allowed to vary following a normal distribution centered at the known CP concentration that is obtained from UV-Vis Spectroscopy. Other parameters allowed to vary included R_{sphere}, R_{polar}, $R_{equatorial}$, $R_{cylinder}$, and $L_{cylinder}$ when applicable. Finally, in the 'sphere+cylinder' and 'ellipsoid+cylinder' models, the fraction of CP present in either sphere/ellipsoid or cylinder form $x_k$was allowed to vary within a uniform distribution from 0 to 1. We fit the combined globular domain radius of gyration data to a logistic function to determine a critical concentration, C_{crit}, at the transition from small to large globular domains:

$$\ln(R_g) = B + \frac{H}{1 + \exp[-W(ln(m_{CP}) - ln(C_{crit}))]} \quad 3\text{-}3$$

where B is a vertical shifting parameter, H is the height of the transition, W is the width of the transition, m_{CP} is the mass fraction of conjugated polymer in the sample, and C_{crit} is the midpoint or inflection point of the transition. Other models used in this work are included in Appendix A.

Wide-Angle X-ray Scattering

SAXS and WAXS data for the samples containing PS-D8 were collected at the 9ID beamline at the Advanced Photon Source at Argonne National Laboratory.[122–124] The instrument used an X-ray source of 21 keV and a beam size of 0.8 x 0.8 mm with a flux density of approximately 5 x 10^{12} photons/second/mm^2. SAXS and WAXS data were collected with exposure times of 10 seconds each. Samples were mounted using custom designed 3D-printed 48-sample

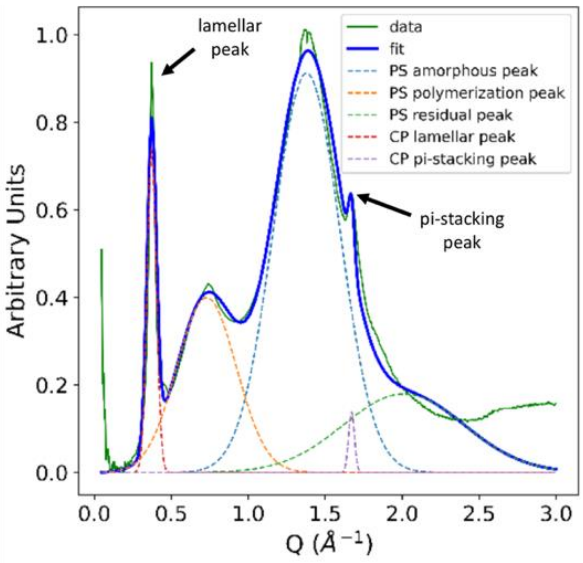

Figure 3-3: Example multi-gaussian fit of wide-angle X-ray scattering (WAXS) data for a solid blend of 10 weight percent of RRe-P3HT in PS-D8 cast from chloroform.

frames[125] that enabled execution of remote experiments during COVID-19 constrained access. SAXS and WAXS data were reduced, de-smeared, and corrected to absolute intensity using the Nika package[126] for Igor Pro. This package was also used to combine the data from the SAXS and WAXS detectors to produce datasets that will be referred to as 'WAXS data' for the remainder of the work.

WAXS data for additional samples batches containing either RRe-P3HT-2 or RRa-P3HT in PS-H8 were measured using an Anton-Paar (Graz, Austria) SAXSess X-ray scattering instrument. The instrument was operated in line collimation mode with a Cu-Kα source (wavelength of 1.54 Å). Solid polymer blends were placed in a custom, 3D-printed frame to hold

the sample in place and ensure the X-ray beam passed through the middle of the sample. The sample chamber was held under vacuum at ambient temperature (approx. 20 °C) during all measurements. Data was collected using Fujifilm (Greenwood, SC USA) image plates and read using a PerkinElmer Cyclone (Covina, CA USA) image plate reader. The Anton-Paar SAXSQuant software was used to reduce data from 2D scattering images to 1D plots of scattering intensity (I) versus scattering vector (Q), remove contributions from the background and desmear the data.

Analysis of WAXS data was performed using the SasView/sasmodels[115,116] and bumps[117] packages for Python. The PS-D8 peaks were first fit using three gaussian distributions for the polymerization peak, amorphous peak, and a trailing background peak.[127] For blend samples, peaks relating to the [100] and [010] reflections of the polythiophene crystal were fit in the 0.25-0.35 $Å^{-1}$ and 1.6-1.7 $Å^{-1}$ ranges, respectively. These reflections pertain to the lamellar and π-stacking directions of the crystal, respectively, and are shown in Figure 3-3 with an example of these fits.

UV-vis Spectroscopy

A Thermo Scientific (Waltham, MA USA) Evolution 300 UV-Visible Spectrophotometer was used for all measurements. UV-Vis spectroscopy was used to determine the final concentration of CP in the solid polymer samples. This was important to accurately determine the actual concentration in the final blend sample, after all processing steps, rather than relying solely on the 'target' concentration. An accurate concentration was also critical to modeling of experimental SANS profiles by minimizing adjustable parameters and subjecting model fits to constraints that will meet the mass-balance of components in all phases. For all SANS modeling, the corrected concentration in wt% was first converted to a volume fraction using a CP density of 1.1 g/mL and a PS-D8 density[128–130] of 1.13 g/mL. Although the volume fraction was used for

SANS modeling, all CP concentrations will be discussed here in units of wt% to be consistent with relevant works[131–136] in the literature.

Conductivity Measurements

Conductivity measurements were performed on an Ametek (Berwyn, PA, USA) Parstat 4000a Potentiostat using RHD Instruments (Darmstadt, Germany) TSC SW closed measuring cell. The samples were first prepared by blade coating square electrodes on each side of the films with silver paste. The square electrodes had a side length of roughly 2mm. The DC current was measured across the thickness of the samples (254 um) as potential was applied ranging from 1-10 V. The conductivity was then derived using geometric calculations. For high resistance samples, the entire measuring cell was enclosed in an aluminum mesh lined enclosure to shield from electromagnetic interference.

3.1.4 Results

Bulk Phase Morphology of Polythiophene/Polystyrene Blends

We modeled the data over the entire range of USANS and SANS to quantitatively describe the CP structures that are formed within the PS-D8 matrix. We first account for the contribution to the scattering due to the PS-D8 phase using the Guinier-Porod model. By performing simultaneous fits of several pure PS-D8 samples and by using the Porod exponent from the previously performed Porod analysis (not covered in this text), we can find a dimensional parameter of $s = 2.5$, a radius of gyration of 180 Å and a scale of 2.1×10^{-4} that adequately capture the natural density fluctuations of the samples that give rise to $I_{PS}(Q)$. $I_{PS}(Q)$ is scaled appropriately for each sample based on the known volume fraction of CP as obtained from UV-Vis while all other parameters of the Guinier-Porod model are held constant.

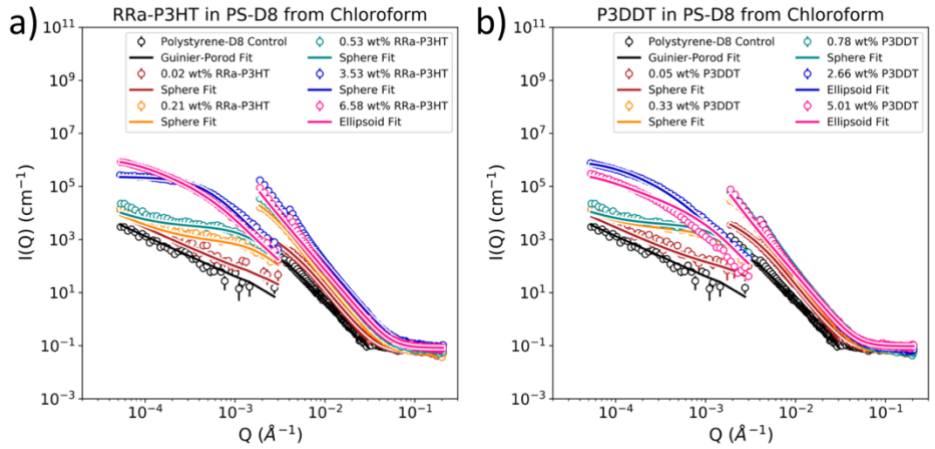

Figure 3-5: SANS and USANS data for blends made from (a) RRa_P3HT and (b) P3DDT in PS-D8 cast from solutions in chloroform. The CP phase was modeled using sphere or ellipsoid fits. All combined models include a common Guinier-Porod fit to account for the PS-D8 phase, and a representative Guinier-Porod fit for a PS-D8 control sample is shown.

To account for the CP scattering contribution, $I_{CP,k}(Q)$, we utilize sphere, ellipsoid and/or cylinder form factors to model the SANS and smeared USANS data for each sample. For blends comprised of RRa-P3HT or P3DDT in PS-D8 cast from solutions of chloroform, a sphere or ellipsoid model adequately captures the CP phase for all samples as shown in Figure 3-5. For these samples, the overall intensity increases, and we observe the Guinier region shifting to lower Q-values as the concentration of the CP increases. This suggests that there is growing phase

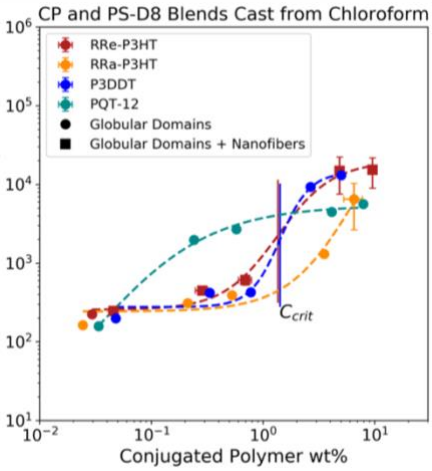

Figure 3-4: Radius of gyration for the globular domain phase (spheres, ellipsoids) in all replicate blends cast from chloroform. A fit of the logistic function is provided as a trendline to guide the eye and estimate. Vertical and horizontal error bars correspond to the standard deviation of and CP concentration.

separation as the CP loading increases and this is confirmed by plotting the globular domain radius of gyration in Figure 3-4. For each sample, we note a significant jump in domain size at a critical concentration (C_{crit}) unique to each conjugated polymer. We approximate these transitions with a log function to be at least 6.5 wt% for RRa-P3HT samples, 1.4 wt % for P3DDT samples, and 1.4 wt% for RRe-P3HT. The RRa-P3HT displays larger globular domains and a lower interfacial concentration, indicating more phase separation.

WAXS measurements allow us to probe the crystallinity in these phase-separated structures within the polythiophene-polystyrene blends. Shown in Figure 3-6 is the WAXS data for blends comprised of RRa-P3HT and P3DDT in PS-D8 cast from solutions of chloroform. There are three broad peaks that correspond to the PS-D8 phase. In the RRa-P3HT samples, the WAXS profiles only show broad peaks across all length scales that indicate a fully amorphous form in both the RRa-P3HT and PS-D8 phases. However, the P3DDT show the presence of additional sharp peaks that appear above the PS-D8 background, indicative of crystalline regimes within the CP phase. WAXS measurements confirm the conformation change that we observed with visual inspection

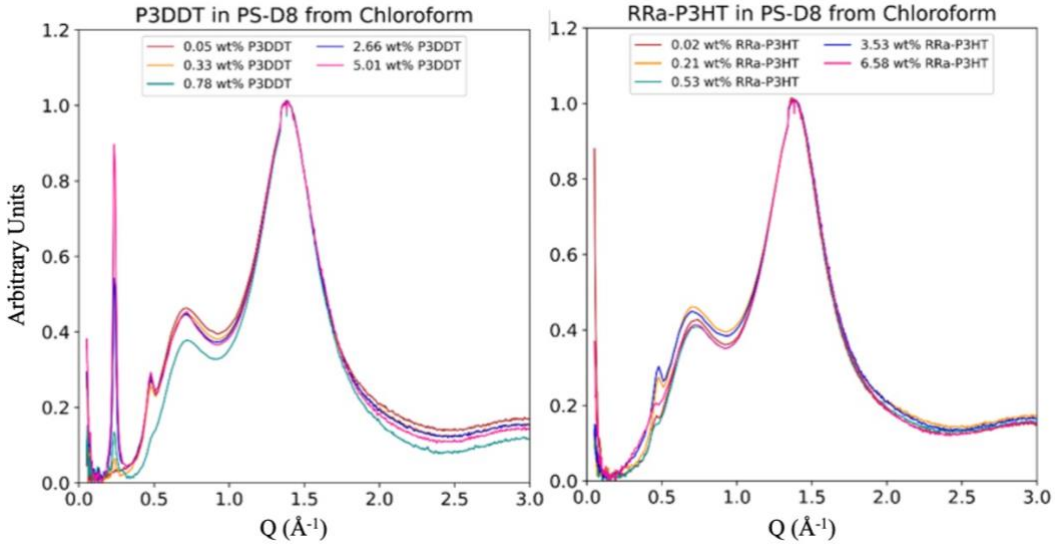

Figure 3-6: WAXS data for blends made from P3DDT (left) and RRa-P3HT (right) in PS-D8 cast from solutions in chloroform.

of the color changes in these samples. As they dried, they formed stiffer chains that phase separated into CP-domains with both crystalline and amorphous regimes.

Solvent Effects of Nanofiber Formation

The SANS profiles for the P3DDT/PS-D8 blends across samples cast from solutions in bromobenzene, chloroform, and toluene, are shown in Figure 3-7. A sphere or ellipsoid model is adequate for capturing the growing, globular phase domains of P3DDT as the CP concentration increases. When plotting the radius of gyration of the globular domains we again find a significant jump in the size of these domains at a critical concentration. The domains in samples cast from chloroform are typically smaller than in samples cast from bromobenzene or toluene at the same P3DDT concentration.

WAXS results for P3DDT blends cast from solutions in bromobenzene, chloroform, or toluene are shown in Figure 3-7. A prominent lamellar peak at approximately 0.25 $Å^{-1}$ grows larger with increasing weight fraction but is minimally affected using different solvents. However, we also note that at no condition is a π-stacking peak observed (expected at approximately 1.7 $Å^{-1}$). This indicates suppression of crystal growth in the π-stacking direction and confirms the SANS results that showed no indication of nanofiber formation.

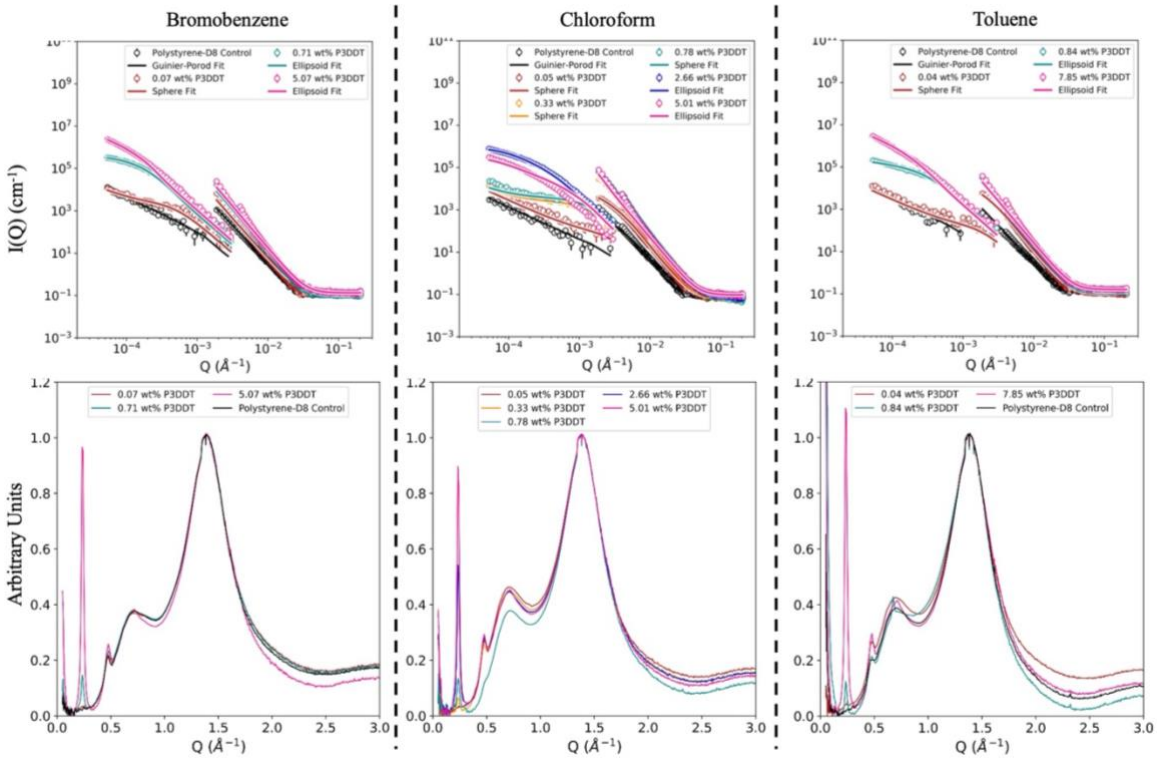

Figure 3-7: (Top row): SANS and USANS data for blends made from P3DDT and PS-D8 cast from solutions in bromobenzene, chloroform, toluene. The conjugated polymer phase was modeled using sphere or ellipsoid fits. All combined models included a common Guinier-Porod fit to account for the PS-D8 phase. A representative Guinier-Porod fit for a PS-D8 control sample is also shown on all plots. (Bottom row): WAXS data for blends comprised of P3DDT and PS-D8 cast from solutions of the same solvents.

For most of the blends comprised of RRe-P3HT and PS-D8, a globular domain model alone (i.e. spheres or ellipsoids) was found to be insufficient to adequately model the data of the CP phase. Given that RRe-P3HT has a high propensity for self-assembly into nanowires, a model for elongated nanostructures was necessary to adequately model the data. Although it is well-established that P3HT nanowires form with a rectangular cross-section[104,137–139], we find that a simpler cylindrical model was also sufficient to model the nanofiber structures while limiting the variables of our fit. Thus, we use sphere+cylinder or ellipsoid+cylinder models to capture the CP that is present in either large globular domains (i.e. spheres or ellipsoids) or in a nanofiber structure (i.e. cylinder). The presence of cylindrical nanostructures is most evident in slope changes occurring at mid- to high-Q in the scattering profiles of RRe-P3HT and PS-D8 blends as shown in

Figure 3-8. When considering the RRe-P3HT that is present in globular domains with or without the presence of nanofibers, we again observe growing aggregates that are similar in size to those created by the RRa-P3HT and P3DDT. We also see again a critical concentration associated with the size of these domains that we estimate at less than 0.097 wt% for RRe-P3HT samples cast from toluene, 1.4 wt% for samples cast from chloroform, and at least 10 wt% for samples cast from bromobenzene shown in Figure 3-9a. The model fits also allow us to further investigate the relative

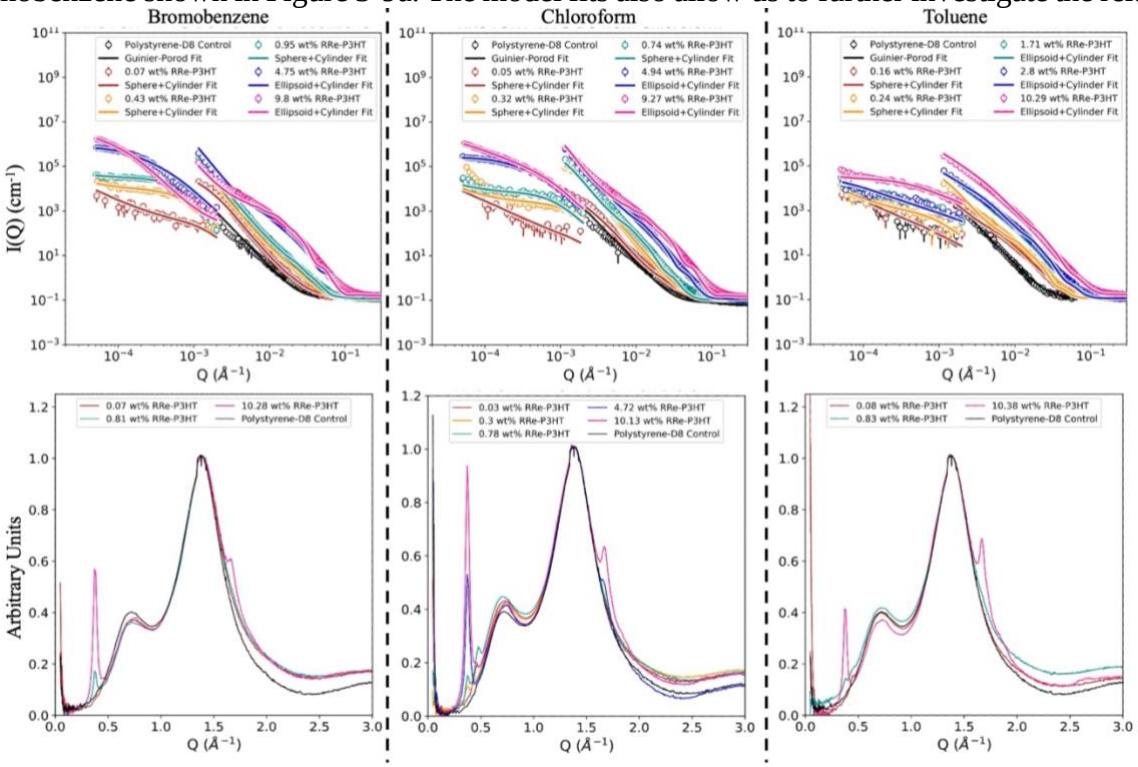

Figure 3-8: (Top row): SANS and USANS data for blends made from high regioregularity RRe-P3HT and PS-D8 cast from solutions in solvents indicated. The CP phase was modeled using sphere, ellipsoid, sphere+cylinder or ellipsoid+cylinder fits. All combined models included a common Guinier-Porod fit to account for the PS-D8 phase, and a representative fit for a PS-D8 control sample is also shown. (Bottom row): WAXS data for blends comprised of RRe-P3HT and PS-D8 cast from solutions in solvents indicated.

amounts of RRe-P3HT that was present in the nanofiber form, as shown in Figure 3-9b. As the solvent evaporates during the drying stage of these blends, the effective polymer concentration in solution increases and allows for RRe-P3HT to self-assemble into nanofibers. This process can be affected by the polymer-solvent interactions (i.e. solubility, polarity) and by the time allowed for

self-assembly. Chloroform and bromobenzene were respectively the fastest and slowest solvents to evaporate from the blends, but both types of samples result in approximately the same amount of nanofiber formation. The toluene samples, however, show the highest concentrations of nanofibers at the same total CP concentrations across most of the range, suggesting that the less favorable interaction between RRe-P3HT and toluene, a known moderate solvent, is the dominating factor in this process, not the time allowed for self-assembly.

WAXS can characterize the preferred growth direction for crystals within the CP phase. Also shown in Figure 3-8 is the WAXS data for a set of RRe-P3HT and PS-D8 blends cast from solutions in bromobenzene, chloroform, and toluene. The broad amorphous peaks at approximately 0.75 and 1.4 $Å^{-1}$ correspond to scattering from the PS-D8 phases. The peaks at approximately 0.4 $Å^{-1}$ and 1.7 $Å^{-1}$ can be attributed to the lamellar and π-stacking distances

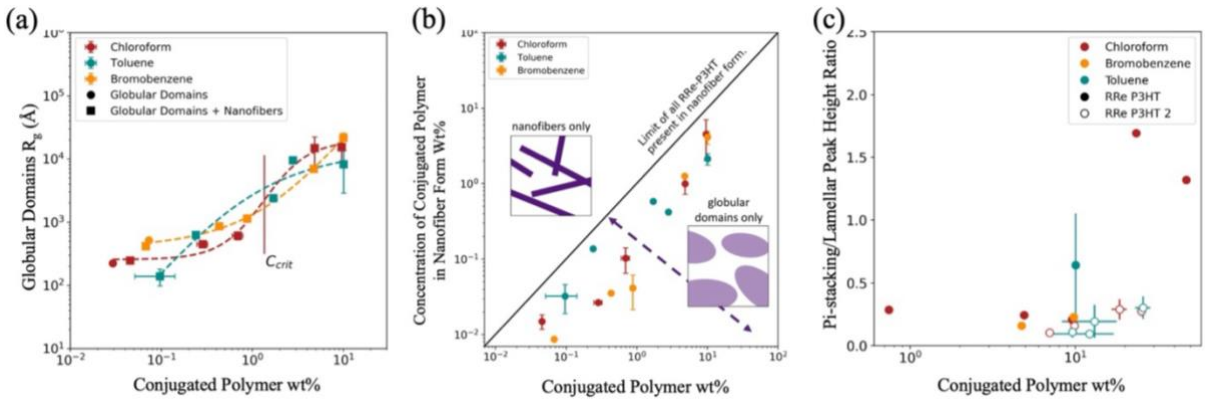

Figure 3-9: (a) Radius of gyration for the globular domain phase (spheres, ellipsoids) in blends of RRe-P3HT in PS-D cast from chloroform, toluene, or bromobenzene. A fit of the log function is provided as a trendline and to estimate. (b) Concentration of CP present in the nanofiber form versus CP concentration in the blends of RRe-P3HT and PS-D8 cast from solutions in chloroform, toluene or bromobenzene. Dashed lines show polynomial fits to guide the eye only. (c) Pi-stacking: lamellar peak height ratio for all replicates of RRe-P3HT and PS-D8 or RRe-P3HT-2 and PS-H8 blends cast from solutions in bromobenzene, chloroform, and toluene.

within the P3HT crystal structure. Many works in the literature[137,140,141] have found that P3HT nanofibers prefer to grow lengthwise in the π-stacking direction, rather than the lamellar direction. As solvent quality is reduced from bromobenzene to chloroform and to toluene, we observe that

the π-stacking peak height is increasing relative to the lamellar peak height. This is quantitatively captured in Figure 3-9c by plotting the lamellar to π-stacking peak height ratio as a function of RRe-P3HT concentration and solvent quality. This plot, however, also shows this same analysis applied to samples of RRe-P3HT-2 and PS-H8 and we do not observe the same effect of solvent on the degree of crystallization in the π-stacking direction. This suggests that nanofiber formation is also dependent on the conjugated polymer's molecular weight. Nevertheless, these results also suggest that nanofiber formation begins while the samples are still in the solution phase and confirm the direct influence of solvent quality on the morphology in the final solid film state.

Blend Conductivity

We aim to relate the nano-scale morphology of CP/PS blends to their performance metrics. Conductivity results for bulk films are provided in Figure 3-10. Many of our samples were found

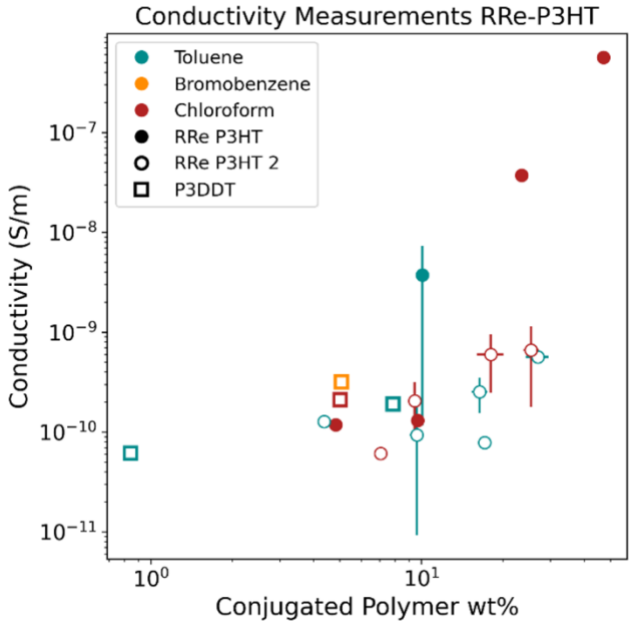

Figure 3-10: Conductivity data for blends comprised of RRe-P3HT or P3DDT in PS-D8 or blends comprised of RRe-P3HT-2 in PS-H8 cast from solutions in toluene, bromobenzene or chloroform.

to be highly insulating, likely due to the use of relatively thick samples (~254 μm), which reached the sensitivity limits of the instrumentation. Additionally, our samples are not doped, a common

approach for increasing the electronic conductivity of CPs.[142] Overall, as we increase the concentration of the conjugated component, we observe a marked improvement in the conductivity for all measurable samples. For RRe-P3HT and RRe-P3HT-2 blends, the conductivity appears to correlate with a higher π-stacking: lamellar peak height ratio, suggesting that the nanofibers improve electronic performance of the bulk material. For P3DDT blends, only minimal conductivity was observed.

3.1.5 Discussion

An advantage of utilizing combined neutron and X-ray scattering analyses is we can gather a rich, quantitative description of the bulk phase morphology in these polythiophene-polystyrene blends that would not be accessible with microscopy methods due to the opaque nature of the samples and the limited contrast between the two organic phases. To aid in visualization of the different observed morphologies, we provide in Figure 3-11 a schematic of the proposed bulk structure for the CP phase in these blends. The CP is shown as either free polymer chains, amorphous/crystalline phases, or nanofibers. The SANS data for all RRa-P3HT and P3DDT and blends were fit with either sphere or ellipsoid models to characterize 'globular' domains, which suggests a strongly phase-separated network of CPs is formed within the PS-D8 matrix. However, the crystalline peaks present in the WAXS data for P3DDT blends indicate that although these materials are not self-assembling into structures such as cylinders, they are still forming coexisting amorphous and crystalline regimes within the CP phase, which is like the behavior observed in pure CP solid-state materials. We find a purely amorphous blend morphology in RRa-P3HT samples and a semi-crystalline blend morphology in the P3DDT blends. As CP concentration increases, we see for each CP component a unique critical concentration at the transition from

small spherical globular domains to larger ellipsoidal domains. Moreover, these transitions show

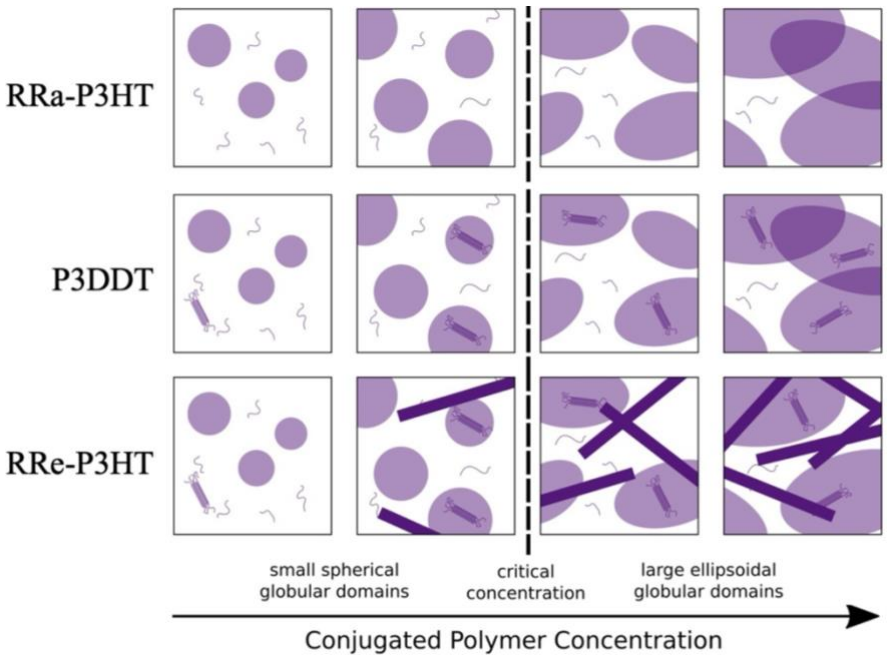

Figure 3-11: Proposed morphology of the CP phase in blends of RRe-P3HT, RRa-P3HT, and P3DDT with PS-D8

that blends of polymers form smaller globular domains, P3DDT form moderate globular domains, and RRa-P3HT form the largest globular domains.

For all RRe-P3HT blends, however, we find that a nanofiber structure coexists with phase-separated semi-crystalline 'globular' domains within the PS-D8 matrix. The proportion of nanofibers increases as the RRe-P3HT concentration increases and as the solvent quality decreases. This nanofiber morphology of the RRe-P3HT blends can form a dense network that facilitates charge transport pathways across the bulk of the film, as shown by the WAXS peak analysis and conductivity results. This is most evident in the samples of RRe-P3HT and PS-D8 cast from solutions in chloroform where we observe a significant increase in the π-stacking/lamellar peak height ratio (indicative of more nanofiber formation) that correlates with an improvement of conductivity by multiple orders or magnitude. The blends created from RRe-P3HT-2 and PS-H8 did not show a clear effect of solvent on the degree of nanofiber formation in

the blend or the conductivity of the sample. However, the degree of folding of the RRe-P3HT chain, which increases with molecular weight, has been shown to play a role in the dimensionality and exciton coupling of nanofibers.[104,137,143]

The neutron scattering data uncovered another important behavior in these blends. We find that a critical concentration (C_{crit}) develops to delineate a sharp transition between 'small' and 'large-scale' phase-separated globular domains. We hypothesize that at this critical concentration, smaller globular aggregates of the CP phase begin to coalesce with others forming the larger aggregates. For RRe-P3HT samples, C_{crit} systematically increases with solvent quality. As solvent quality decreases, it is more favorable for these globular domains to aggregate resulting in a lower critical concentration. However, the critical transition (C_{crit}) in globular domains for RRa-P3HT and P3DDT samples does not appear to trend simply with the expected polymer-solvent interactions.

The use of different solvents in the RRe-P3HT blends also showed a significant impact on the degree of nanofiber formation in these samples. Conversely, we did not observe any nanofiber formation in the P3DDT blends, only globular domains of the CP phase that were minimally affected by solvent choice. This suggests that there are complex interactions occurring in the solution phase, not only between the CP and solvent but also between the CP and PS-D8 phases, that affect the final, solid-state morphology. Nanofiber formation has been shown in the literature to occur across a range of poly(3-alkylthiophenes),[144–146] with formation influenced by side-chain length, molecular weight of the polymer, and the solvents used to encourage the fiber formation. The solvents chosen in this work have varying ranges of solubility for P3HT specifically. Due to the higher molecular weight of our P3DDT material, as well as its increased solubility (due to the longer alkyl side chains), we expect processing to result in less nanofiber formation compared to

RRe-P3HT. It is also worth noting that, although we see the most nanofiber formation in RRe-

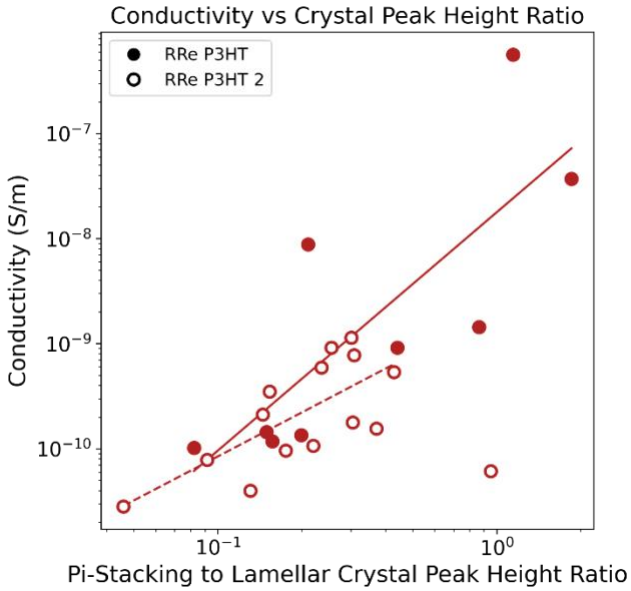

Figure 3-12: Correlation plot between conductivity and the ratio between the peak heights of the lamellar and π-stacking peaks RRe-P3HT and RRe-P3HT-2 blends cast from chloroform. Solid and dashed lines overlaid on the data are linear fits with R-values of 0.796 and 0.715 of PS blends with RRe-P3HT and RRe-P3HT-2, respectively.

P3HT samples cast from toluene (a moderate solvent), we still observe significant nanofiber formation in samples cast from bromobenzene and chloroform (good solvents). In a pure solution of RRe-P3HT in either of these solvents, we would expect nanofiber formation to be difficult and limited. However, there are additional factors in the solution state to consider, such as CP-PS interactions, solvent drying time, and starting concentrations, that can significantly affect self-assembly and the solid-state morphology. In our RRe-P3HT blends, we found that higher nanofiber formation resulted in higher π-stacking/lamellar peak height ratios extracted from the WAXS data, indicating a preferred crystal growth direction in the π-stacking direction. When we investigate the conductivity in these same samples, we find that the higher π-stacking/lamellar peak height ratios can be directly correlated to increased conductivity. P3DDT blends which displayed no nanofiber growth resulted in conductivities that were comparable to RRe-P3HT, and RRe-P3HT-

2 blends that showed the least amount of nanofiber formation (low π-stacking/lamellar peak height ratios). However, the performance in these blends is multiple orders of magnitude lower than that of the blends with significant nanofiber formation and was only minimally within the sensitivity of our instruments, emphasizing the importance of the crystallization in the π-stacking direction and formation of nanofiber networks in these systems. To further highlight this relationship, Figure 3-12 shows a correlation plot between conductivity and the π-stacking/lamellar peak height ratio from WAXS for RRe-P3HT blends with PS-D8 cast from chloroform. The P3DDT blends did not show a visible π-stacking peak. The preferred growth of crystallization (π-stacking) is in-fact shown to have a significant influence on the performance in these systems.

3.1.6 Conclusions

In this work, we have used both SANS and WAXS to characterize blends comprised of RRe-P3HT, RRa-P3HT, and P3DDTin PS-D8. These conjugated and commodity polymer blends are advantageous for reducing costs of the material and improving mechanical stability while also maintaining charge transport properties of the conjugated component. A combined neutron and X-ray scattering approach enabled access to the bulk morphology in these systems that are not accessible with common microscopy methods. Model fitting of the SANS data found the CP to phase separate from the PS-D8 and form various, complex structures within the matrix component. RRa-P3HT formed an amorphous globular phase separation morphology while P3DDT displayed similar globular phases with both amorphous and crystalline regimes, as confirmed by WAXS (semi-crystalline morphology). Finally, RRe-P3HT samples were found to form both semi-crystalline globular domains and nanofibers. Fitting of the SANS data also found a critical concentration at which the blends make a significant transition from smaller to larger globular

domains, a behavior that has not yet, to the best of our knowledge, been observed in these conjugated and non-conjugated polymer blends.

By comparing RRe-P3HT blends cast from solutions in different solvents (bromobenzene, chloroform, or toluene), we were able to determine that the less favorable interactions between the CP and toluene, a moderate solvent, were a primary driving force in the formation of nanofibers. Samples cast from toluene showed a constant and higher percentage of RRe-P3HT in nanofiber form when compared to samples cast from chloroform and bromobenzene, indicating that nanofiber formation begins to occur in the solution phase.

Finally, we relate the phase morphology to performance in these blends with conductivity measurements. The π-stacking to lamellar peak height ratio from WAXS results, which is indicative of nanofiber formation, was found to be directly correlated to the blend conductivity indicating that these nanofiber networks were critical to forming sufficient charge transport pathways across the bulk of the RRe-P3HT blends. As CP blends are increasingly explored in flexible device applications, it is important that fundamental relationships between processing decisions (e.g. solvent, temperature, evaporation rate), the blend morphology, and charge transport are well understood so that they may be used to improve and control material and device performance.

3.2 Trends in mobility help elucidate the interdigitating behavior of side chains in IDT based conjugated polymers.

This chapter section contains material from the following publication and the author would like to acknowledge the contributions of all coauthors:

Sommerville, P. J. W., Balzer, A. H., Lecroy, G., **Guio, L.,** Wang, Y., Onorato, J. W., Kukhta, N. A., Gu, X., Salleo, A., Stingelin, N., and Luscombe C. K. Influence of Side Chain Interdigitation on Strain and Charge Mobility of Planar Indacenodithiophene Copolymers. ACS Polymers Au 2023 3 (1), 59-69. DOI: 10.1021/acspolymersau.2c00034

Statement on Distribution of Work: The work done herein was a combination of efforts by all the authors. Specifically, I was responsible for the fabricating and testing organic field effect transistors and collection of hole mobility data. The first author, Dr. Sommerville, synthesized the polymers used in this paper and performed the overall analysis. Dr. Garrett Lecroy collected the GIWAXS data and aided in analysis and peak assignments. We also discussed ideas and conclusions from the data collaboratively prior to the writing of this paper.

3.2.1 Introduction

Increased interest in deformable electronic devices such as e-skin, wearable sensors, stretchable organic photovoltaics, soft robotics, and stretchable organic field effect transistors warrants the development of intrinsically deformable electronic materials[11,19,147,148]. Π-conjugated polymers (CPs) can be utilized as a semiconducting material within deformable devices because of their tunable electronic properties and wide variance of mechanical properties[23]. As is the case for commodity polymers and their applications, a single CP often does not satisfy the various optoelectronic, semiconducting, or mechanical requirements imposed by a given deformable

electronic application. Polymers with different elastic moduli, elongation at breaks, rheological properties, stress-strain profiles, solubilities, optoelectronic profiles, and hole mobilities are, thus, required to fulfill the various needs of certain applications. This warrants the further development of structure-property relationships for CP systems to guide the design of new intrinsically deformable CPs to address this need.

Side chain substitution has been shown to impact the materials properties of semicrystalline CPs. For both poly(3-alkylthiophene) (P3ATs) and DPP-based CPs it has been shown that increasing the length or increasing branching of side chains results in increased extensibility and decreased elastic modulus.[149–151] This is caused primarily because of a resultant decrease in both glass transition temperature (T_g) and the amount of load bearing interactions that occur between polymer backbones during deformation, with both effects affording these materials an enhanced ability to reorganize polymer chains during strain[148]. It is important to consider however that the side chain modifications can also lead to changes in the overall polymer assembly and the resulting thin-film microstructures that manifest differences in hole mobility.[152,153]

Poly(indacenodithiophene-benzothiazdiazole) (PIDT$_{C16}$-BT) (Figure 1) is the most studied IDT-copolymer and has displayed charge mobilities of up to 10 $cm^2\ V^{-1}\ s^{-1}$.[154] In terms of mechanical properties, PIDT$_{C16}$-BT, like most polymers, is brittle at low molecular weight (M_n = 12 kg/mol) with a crack onset strain (*CoS*) of just 3%,[155] extensible up to 22% of its original length at significantly higher molecular weight (M_w = 295 kg/mol);[156] and it has elastic moduli ranging from 150-750 MPa depending on molecular weight.[155,156] Similarly to PIDT$_{C16}$-BT, poly(indacenodithiophene-thiopyrollodione) (PIDT$_{C16}$-TPD$_{C1}$) (Figure 1) has a highly coplanar backbone, limited long-range order, a *CoS* of 3%, an elastic modulus ranging between 110 to 410 MPa; and it displays μ_{hole} equal to that of PIDT$_{C16}$-BT when processed under the same

conditions.[155] In contrast to both PIDT$_{C16}$-BT and PIDT$_{C16}$-TPD$_{C1}$, the more torsioned IDT-copolymer poly(indacenodithiophene-benzopyrollodione) (PIDT$_{C16}$-BPD$_{C1}$) is much more extensible than PIDT$_{C16}$-BT, displaying a *CoS* of 75% at low molecular weight (M_n = 14 kg/mol).[155] The backbone torsion in PIDT$_{C16}$-BPD$_{C1}$ has the positive effect of generating a 360° side chain extension profile which allows the system to undergo plastic deformation, but the backbone disorder negatively impacts charge mobility.[157] Comparing the mechanical and electronic properties of these IDT-copolymers highlights the necessity of backbone planarity for low energetic disorder and thus high μ_{hole}, as well as the impact that side chains have on the mechanical deformation of IDT-copolymers. Therefore, altering the side chains of PIDT$_{C16}$-BT and PIDT$_{C16}$-TPD$_{C1}$, which are both coplanar, is a potential strategy to endow each polymer system with increased extensibility and decreased elastic moduli without significantly altering their μ_{hole}.

Five distinct IDT-copolymer systems are synthesized and investigated herein to determine the impact that side chain substitution has on the mechanical and electronic properties of planar IDT copolymers. The structures of these polymers are shown in Figure 3-13. There are two polymer samples with the PIDT$_{C16}$-BT backbone structure. They differ in the length of the alkyl side chain on the IDT unit of backbone. These two polymers, which are referred to as the BT-containing IDT-copolymers, are PIDT$_{C16}$-BT and PIDT$_{C20}$-BT due to the hexadecane (C_{16}) and isodecane (C_{20}) side chains covalently bound to the IDT monomer unit. Three polymer systems were synthesized with the PIDT$_{C16}$-TPD$_{C1}$ conjugated backbone structure. These systems, which are referred to as TPD-containing IDT copolymers, differ in the length and degree of branching of alkyl side chains stemming from the TPD monomer unit. These TPD-containing systems are referred to as PIDT$_{C16}$-TPD$_{C1}$, PIDT$_{C16}$-TPD$_{C8}$, and PIDT$_{C16}$-TPD$_{C13B}$ due to the methyl (C_1), octyl (C_8), and (6-ethyl)-undecane (C_{13B}) side chains that are covalently bound to the TPD monomer

unit of each respective polymer. The "13B" notation of $PIDT_{C16}$-TPD_{C13B} signifies that the side

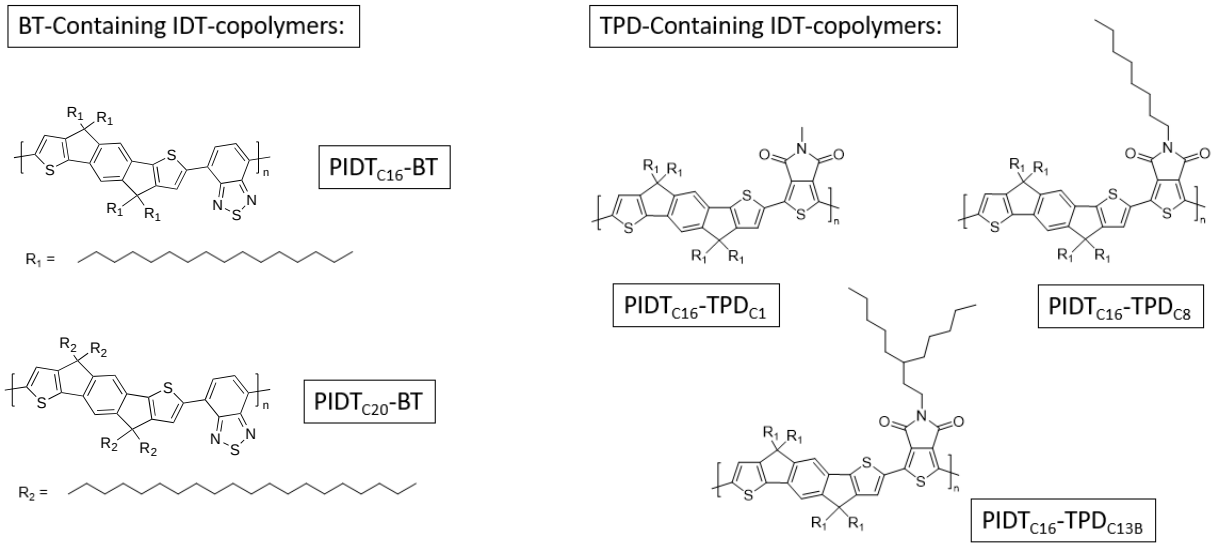

Figure 3-13: The structures of the BT-containing IDT copolymers which vary in the length of each side chain extending from the IDT monomer (left) and the TPD-containing IDT-copolymers which have the same side chains at the IDT monomer and vary side chain character at the TPD-position (right).

chain contains 13-carbons in total and is branched. Each of the TPD-containing systems have IDT monomers with linear C_{16} side chains.

We observe that IDT-copolymers with no or methyl side chains on their acceptor unit ($PIDT_{C16}$-BT, $PIDT_{C20}$-BT, and $PIDT_{C16}$-TPD_{C1}) display a (001) scattering peak in their GIWAXS profile that is representative of parallel alignment of polymer backbones with translational order within their thin films. For this arrangement of polymer backbones to occur, we hypothesize that it is necessary for the long and linear side chains stemming from the IDT unit to interdigitate with the side chains of neighboring chains. The lengthened and branched side chains on the TPD-monomer unit in $PIDT_{C16}$-TPD_{C8} and $PIDT_{C16}$-TPD_{C13B} prohibit interdigitation and side chain ordering, affecting in turn the backbone assembly. Due to the lack of side chain interdigitation, $PIDT_{C16}$-TPD_{C8} and $PIDT_{C16}$-TPD_{C13B} seem to show improved ductility and decreased elastic moduli. However, while these polymers retain their backbone planarity, they display reduced μ_{hole}

– an observation that provides further evidence for the importance of parallel alignment of IDT-copolymer backbones with translational order to achieve high μ_{hole}. In contrast, $PIDT_{C16}$-BT, $PIDT_{C20}$-BT, and $PIDT_{C16}$-TPD_{C1} have higher μ_{hole} but are more brittle. These results demonstrate that side chain substitution of IDT-copolymers affects their ability to interdigitate causing them to be more disordered. As a result, IDT-copolymers with a denser side chain attachment display reduced μ_{hole}, reduced elastic modulus, and increased elongation at break.

3.2.2 Materials

Full details are provided in the published article supporting information. A representative polymerization procedure is described below. All other polymerizations were carried out using a similar procedure.

Synthesis of $PIDT_{C16}$-BT

Poly(4-methyl-7-(4,4,9,9-tetrahexadecyl-7-methyl-4,9-dihydro-s-indaceno[1,2-b:5,6-b']dithiophen-2-yl)benzo[c][1,2,5]thiadiazole)

This was performed as reported previously.[155] A mixture of IDT_{C16} (58.2 mg, 0.05 mmol), $BT\text{-}Br_2$ (14.7 mg, 0.05 mmol), tris(dibenzylideneacetone)dipalladium(0) (2.3 mg, 5 mol%), tris(*o*-anisyl)phosphine (1.8 mg, 10 mol%), cesium carbonate (81 mg, 0.25 mmol) and pivalic acid (2.6 mg, 0.025 mmol) in *o*-xylene (1 mL) was degassed and filled with nitrogen in a pressure reaction tube. The tube was sealed and the mixture was heated at 100 °C for 16 h, then cooled to room temperature and precipitated into methanol (100 mL). The precipitate was filtered through a Soxhlet thimble and then purified by Soxhlet extraction with methanol, acetone, and hexanes. The hexanes fraction was collected, and the solvent was removed by rotary evaporation. The residue was dissolved in chloroform and precipitated into methanol. The precipitate was collected by filtration and dried under vacuum to afford a deep blue solid in 68% yield. (500 MHz, $CDCl_3$, δ,

ppm): 8.10 (s, 2H), 7.95 (s, 2H), 7.39 (s, 2H), 2.08 (s, 4H), 1.96 (s, 4H), 1.17 (m, 112H), 0.85 (t, 12H).

Five different IDT-copolymer samples were prepared using direct arylation polymerization (DArP). Unalkylated IDT- and TPD-monomers, and the alkylated monomers IDT_{C16} and TPD_{C1}, were synthesized as previously reported.[155] The monomer IDT_{C20} was synthesized by alkylating the IDT core with 1-bromoicosane instead of 1-bromohexadecane. The TPD_{C8} and TPD_{C13B} monomers were synthesized by alkylating the TPD core with 1-bromooctane and 6-(bromoethyl)-undecane, respectively, in place of methyl iodide. Following our previously utilized procedures, direct arylation polymerization was used to synthesize $PIDT_{C16}$-BT, $PIDT_{C20}$-BT, $PIDT_{C16}$-TPD_{C1}, $PIDT_{C16}$-TPD_{C8}, and $PIDT_{C16}$-TPD_{C13B}.[157] These polymers were subjected to ^{1}H NMR spectroscopy and size exclusion chromatography at 30 °C to characterize their chemical structure and M_n. The degree of polymerization (DP) can be used to compare the size of each polymer system, given the fact that the mass of the donor-acceptor (D-A) repeat unit varies greatly due to the variation in alkyl chain content in each system. Based on DP, all polymers can be designated as belonging to the low-molecular weight regime (Table 3-1).

Table 3-1: Molecular weight, polydispersity, degree of polymerization and combined molecular weight of comonomer units for each IDT-based copolymer used in this study.

Polymer Sample	M_n (g/mol)	Đ	Combined M.W. of Comonomer Units (u)	DP
$PIDT_{C16}$-BT	11000	1.8	1297	8
$PIDT_{C20}$-BT	21000	2.8	1521	14
$PIDT_{C16}$-TPD_{C1}	9000	1.7	1326	7
$PIDT_{C16}$-TPD_{C8}	11000	1.8	1426	8
$PIDT_{C16}$-$TPDC_{13B}$	14000	2.1	1496	9

3.2.3 Methods

NMR Characterization

^{1}H NMR and ^{13}C NMR spectra were collected on a 500 MHz Bruker AV500 NMR spectrometer. $CDCl_3$ was used as solvent and the measurements were conducted at room temperature.

SEC Characterization

The polymer molecular weights (vs. narrow dispersity polystyrene standards) were determined using a Viscotek TDA 305 gel permeation chromatography (GPC) system with combined UV detector at 30 °C, using chlorobenzene at a flow rate of 0.5 mL/min as the eluent.

Optoelectronic measurements

UV-Vis absorption and PL spectra were measured on a Varian Cary 5000 UV-Vis-NIR spectrometer and a Horiba Fluorolog FL-3 spectrometer, respectively. Solution measurements were performed in chloroform solutions with a polymer concentration of 0.05 mg/mL. Thin films used for measurement were spin cast from a chloroform solution with a polymer concentration of 5 mg/mL onto cut glass substrates.

Crystallographic measurements

Grazing incidence wide-angle X-ray scattering (GIWAXS) measurements are conducted at Stanford Synchrotron Radiation Lightsource, SLAC National Accelerator Laboratory, Beamline 11-3. An incident X-ray energy of 12.7 keV was used. The incidence angle α of the X-ray beam was 0.1°. Scattering intensity was detected with a Rayonix MX225 CCD 2D area detector, and sample to detector distance was calibrated with a LaB6 polycrystalline standard. Data is reported in terms of the scattering vector, $q = (4\pi/\lambda)\sin(\theta)$, where θ is the angle of scattering. GIWAXS raw data was corrected for distortions introduced by the area detector with Nika 1D SAXS[158] and WAXStools[159] software packages in Igor Pro. Polymer films for GIWAXS were prepared in the same method as those prepared for CMS described above.

Field Effect Mobility Measurements

Heavily boron-doped silicon substrates with a 300 nm (± 5 nm) thick thermal oxide layer (University Wafer) as a gate dielectric were used for the thin-film field-effect transistors (FETs). Substrates were first scrubbed with detergent and water and then sonicated in DI water, acetone, and IPA for 15 min per solvent, followed by drying under a stream of compressed nitrogen. The substrates were then cleaned in a plasma cleaner for 15 min using air plasma. To passivate the thermal oxide, a vacuum vapor deposition of octadecyl trichlorosilane (ODTS) on the cleaned substrates was used. After the ODTS deposition, the substrates were rinsed with chloroform ($CHCl_3$) and IPA to remove any physiosorbed ODTS from the surface. The polymer layer was then spin-coated from a 5 mg/mL solution of each polymer in $CHCl_3$ at 1500 RPM for 60 s onto the ODTS passivated substrates in a N_2 environment. Gold electrodes were thermally evaporated onto the active layer to a thickness of 100 nm at a rate of 0.5 Å s^{-1} . The gold was evaporated from an alumina coated Mo boat and the electrodes were deposited through a shadow mask. After electrode deposition, the devices were tested for charge mobility, threshold voltage and current on/off ratio. The devices had a top-contact bottom-gate architecture with a channel width of 1000 µm and a channel length of 50 µm. They were tested in a nitrogen atmosphere using a Signatone Probe Station and two Keithley 2400 Source-Measure units. The transfer curves were collected in the saturation regime, where the linear section of the curve was fitted to estimate the charge mobility using the following equation:

$$I_D = \frac{WC\mu}{2L}(V_G - V_t)^2$$

where I_D is the drain-source current; µ is the charge mobility; W is the channel width; L is the channel length; C is the capacitance per unit area of the insulator (SiO_2, 300 nm, 10 $nF \cdot cm^{-2}$). V_G is the gate voltage; and V_t is the threshold voltage. The threshold voltage was obtained by

fitting the linear region of the $I_D^{1/2}$ vs V_G curve and extrapolating to $I_D = 0$. Measurements were averaged from at least five transistors across three substrates and devices.

Pseudo free-standing tensile tests

Thin film tensile tests were performed on the water surface through pseudo-free-standing tensile tester. Details about the tensile stage setup can be referred to our previous publication.[160] Briefly speaking, the polymer thin films (≈90 nm) were patterned into dog-bone shape by oxygen plasma etching process and floated on top of water before being further unidirectionally pulled at a strain rate of 5×10^{-4} s^{-1} until the film fractures. At least six independent samples were measured for each conjugated polymer to provide statistically averaged mechanical properties. The elastic modulus was obtained from the slope of the linear fit of the stress–strain curve using the first 0.5% strain (elastic region).

3.2.4 Results and Discussion

As is expected for IDT copolymers, GIWAXS for each polymer displayed broad and diffuse crystallographic signals as shown in Figure 3-14. The pi-stacking peak (010) is expected in the 1.6-1.65 Å-1 region. Its absence and the broad peak at 1.2 – 1.5 Å-1 suggest disordered side chains, short coherence lengths and reduced crystallinity[21] for all the polymers and can therefore

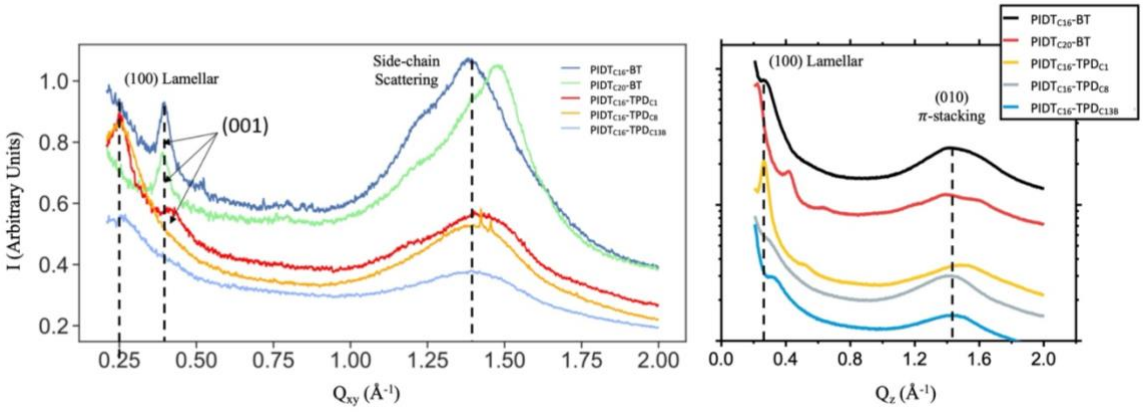

Figure 3-14: Linecuts of the 2D GIWAXS spectra in the Q_{xy} direction (in-plane, left) and Q_z direction (out-of-plane, right) of each IDT-copolymer is shown. The (001) signal is labeled for clarity. The full 2D spectra can be found in the SI of the published article.

be lacking long-range crystalline order[17]. The in-plane (100) signal can be seen for the TPD-copolymers at 0.25 Å-1 indicating interlamellar spacing of ~24-25 Å. Additionally, the out-of-plane (100) signal is observable in both the BT and TPD copolymers suggesting that all polymers have some parallel alignment with the BT series being oriented more edge-on. PIDT$_{C16}$-BT, PIDT$_{C20}$-BT, and PIDT$_{C16}$-TPD$_{C1}$ displayed an in-plane (001) backbone signal, which indicates translational order of rigid IDT-copolymer segments,[161] while PIDT$_{C16}$-TPD$_{C8}$ and PIDT$_{C16}$-TPD$_{C13B}$ do not show this peak. The (001) peak position of the BT-containing systems is at a slightly higher Q-value than observed for PIDT$_{C16}$-TPD$_{C1}$ due to slight differences in the backbone repeat-unit length. It has been observed in scanning tunneling microscopy measurements that side chains of PIDT$_{C16}$-BT interdigitate tightly when aligned in parallel.[162] The interdigitation of alkyl side chains is perhaps a necessary condition for the translational order, or precise intermolecular shifts, of IDT copolymer backbones, and thus for the appearance of the (001) reflection. Having long side chains on every monomer rather than every other monomer is effectively increasing the side chain attachment density, which has been shown to inhibit side chain interdigitation in CPs.[163] Thus, it is reasonable to suggest that the absence of a (001) signal in PIDT$_{C16}$-TPD$_{C8}$ and PIDT$_{C16}$-TPD$_{C13B}$ thin films is due to the long (and branched in the case of PIDT$_{C16}$-TPD$_{C13B}$) alkyl side chains extending from the TPD monomers, which disrupts the uniform pattern by which side chains extend away from the IDT copolymer backbone when only the IDT monomer is alkylated. The regular extension of alkyl chains from the IDT monomer unit alone, provides sufficient space for interdigitation with side chains of neighboring, and parallelly aligned, macromolecules. Representations of interdigitating IDT-copolymers with lower side chain attachment density and IDT-copolymers with increased side chain attachment density are shown in Figure 3-15. While the presence of the (001) signal in a thin film arises from just a fraction of polymer chains, the

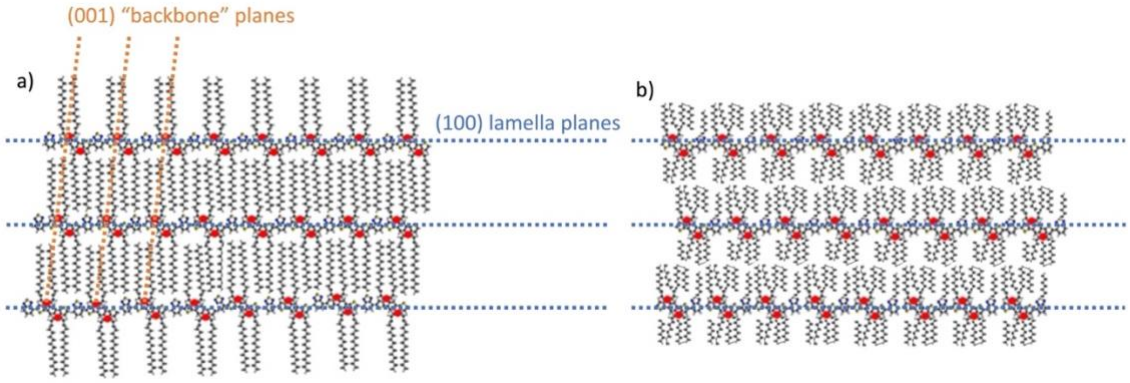

Figure 3-15: IDT-copolymers with side chains on only the IDT subunit (blue block) are able to interdigitate side chains and show translational order between the chains (a) and IDT-copolymers with side chains on the IDT-monomer and TPD-monomer cannot interdigitate t heir side chains and therefore do not align as precisely (b).

alignment of IDT copolymers is an arrangement that does impact the electronic properties of resultant thin films,[161] and may impact the mechanical properties of IDT-copolymer thin films studied herein.

The UV-Vis absorption spectra of all polymers in solution and thin films are shown in Figure 3-16. BT-containing IDT-copolymers exhibit more pronounced redshifts in absorbance maximum than TPD-containing systems upon casting into thin films from solution suggesting that they adopt a higher degree of planarization in the solid state. In solution the BT-containing polymers have visible but less pronounced 0-0 transitions compared to the TPD-containing polymers, for which the transition is strongly pronounced. All polymers studied herein display a pronounced 0-0 transition in thin films. This 0-0 transition is indicative of J-aggregation behavior,[164] and has been observed in PIDT$_{C16}$-BT and PIDT$_{C16}$-TPD$_{C1}$ previously.[155,157] The

Stokes shift of the TPD-containing IDT copolymers in solution is approximately half that of the BT-containing IDT copolymers. This suggests that the TPD-containing systems may in fact be more planar and rigid than the BT-containing systems,[165] which is in agreement with previously

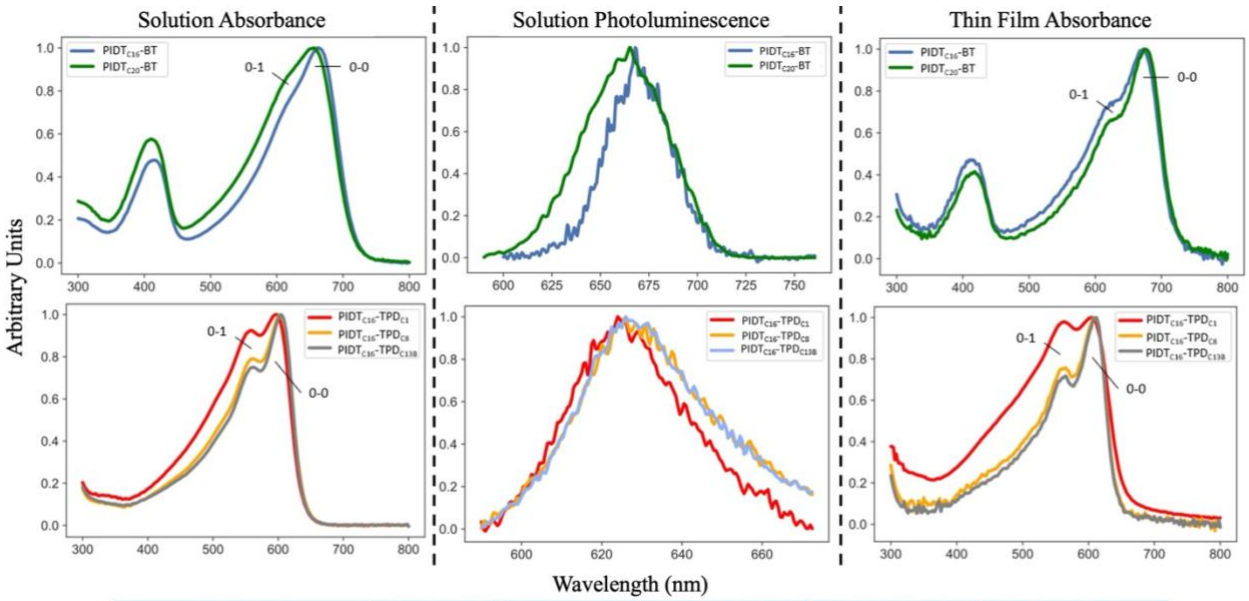

Sample (Solution)	$PIDT_{C16}$-BT	$PIDT_{C20}$-BT	$PIDT_{C16}$-TPD_{C1}	$PIDT_{C16}$-TPD_{C8}	$PIDT_{C16}$-TPD_{C13B}
λ max absorbance (nm)	662	656	598	604	604
Stokes Shift (nm)	46	49	26	22	22

Figure 3-16: (Top)Solution and thin film absorption spectra and solution photoluminescence spectra for each IDT-copolymer. (Bottom): Table showing wavelength at maximum absorption and the stokes shift for each polymer.

performed density functional theory calculations comparing $PIDT_{C16}$-BT to $PIDT_{C16}$-TPD_{C1}.[155] The similarity in Stokes shift between $PIDT_{C16}$-TPD_{C1}, $PIDT_{C16}$-TPD_{C8}, and $PIDT_{C16}$-TPD_{C13B} suggests that the planarity and rigidity of the polymer backbone is not altered by side chain substitution. Within each IDT copolymer family, the optoelectronic properties are strikingly alike, suggesting that the side chain substitution at these positions minimally impacts the optoelectronic properties of IDT copolymers.

Film-on-water thin film tensile measurements were performed to quantify and compare the mechanical properties of the IDT-copolymers.[166] The stress-strain curves of all polymer systems except $PIDT_{C16}$-TPD_{C1} are shown in Figure 3-17. Five samples were tested for each polymer and

the thickness of the films ranged from 50-61 nm. PIDT$_{C16}$-TPD$_{C1}$ was too fragile to load onto the strain stage for reliable measurement. Comparing PIDT$_{C16}$-BT to PIDT$_{C20}$-BT, a slight increase in extensibility is observed when increasing the length of the alkyl side chains on the IDT subunit. The PIDT$_{C16}$-BT sample is very brittle and fractured within 1% of strain at this low molecular weight. The PIDT$_{C20}$-BT sample did elastically deform until fracture was observed at 2% strain. We suggest that the needed molecular reorganization is inhibited by the interdigitation of this polymer's side chains, which leads to embrittlement of the material by preventing plastic flow.[167,168] We ascribe the slightly larger elongation at break of PIDT$_{C20}$-BT system compared to PIDT$_{C16}$-BT to the former's higher average molecular weight. Moreover, we find that increasing the length of the IDT-unit side chain does not lead to a significant decrease in elastic modulus,

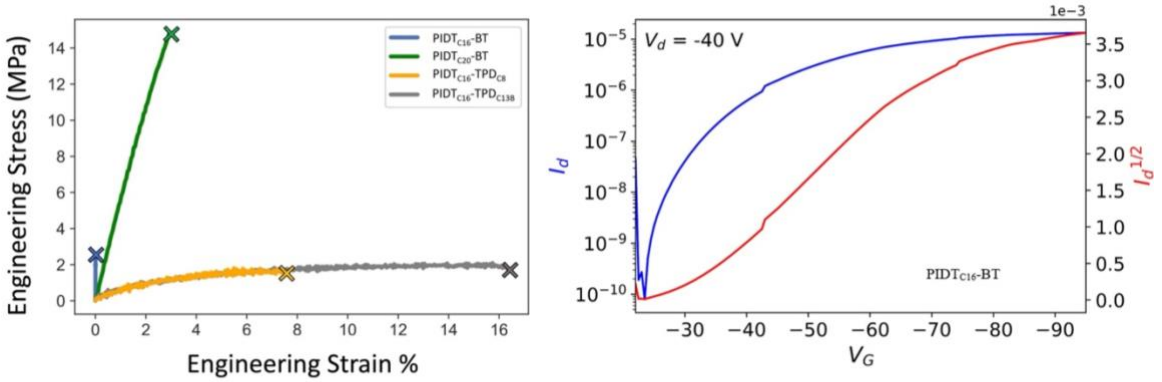

Sample (Solution)	PIDT$_{C16}$-BT	PIDT$_{C20}$-BT	PIDT$_{C16}$-TPD$_{C1}$	PIDT$_{C16}$-TPD$_{C8}$	PIDT$_{C16}$-TPD$_{C13B}$
Elastic Modulus (MPa)	NA	520 ± 70	NA	14 ± 2	56 ± 5
% Elongation at Break	0	2 ± 1	NA	7 ± 2	16 ± 4
OFET Hole Mobility (cm²/Vs)	0.068 ± 0.020	0.023 ± 0.003	0.051 ± 0.030	0.007 ± 0.005	0.006 ± 0.002
OFET Threshold Voltage	-30	-60	-57	-60	-34
GIWAXS (001) Reflection Present?	✅	✅	✅	❌	❌

Figure 3-17: (Top Left): Representative stress-strain curves obtained through film-on-water elongation measurements for all IDT-copolymers except PIDT$_{C16}$-TPD$_{C1}$, which was too brittle to be tested. The colored 'X' on each line denotes the elongation at break of each material for clarity. (Top Right): Representative OFET transfer curve. (Bottom): The mechanical properties and hole mobility of each IDT-copolymer are tabulated. The elastic moduli of PIDT$_{C16}$-BT is effectively infinite because of the verticality of the stress strain curve.The PIDT$_{C16}$-TPD$_{C1}$ material was too fragile to be loaded onto the strain stage for measurement.

supporting the view that increasing side chain length does not have a significant plasticizing effect.

In contrast, both PIDT$_{C16}$-TPD$_{C8}$ and PIDT$_{C16}$-TPD$_{C13B}$ were able to undergo plastic deformation during elongation, despite low molecular weight. As a result, these polymers displayed average elongation at break values of 7% and 16% for PIDT$_{C16}$-TPD$_{C8}$ and PIDT$_{C16}$-TPD$_{C13B}$, respectively. Side chain substitution at the TPD-position led to reductions in elastic moduli, with PIDT$_{C16}$-TPD$_{C8}$ and PIDT$_{C16}$-TPD$_{C13B}$ displaying elastic moduli of 14 MPa and 50 MPa respectively. The elastic moduli, when compared to other reported polymers (e.g., diketopyrrolopyrrole (DPP)-based polymers have elastic moduli ~150 – 480 MPa;[149] P3HT has been reported to have elastic moduli ~200-300 MPa[169]) are remarkably small despite these two polymers' backbone rigidity. These attributes increase their suitability in wearable or e-skin devices due to a modulus which is more closely related to that of skin.[170] We moreover suggest that the decreased elastic moduli of PIDT$_{C16}$-TPD$_{C8}$ and PIDT$_{C16}$-TPD$_{C13B}$ and the ability to plastically deform, is due to the lack of side chain order caused by the inclusion of longer side chains on the TPD unit.[171] From a structural perspective, it is the increased density of alkyl side chains on PIDT$_{C16}$-TPD$_{C8}$ and PIDT$_{C16B}$-TPD$_{C13B}$ that hinders side chain order (i.e., side chain interdigitation), which in turn provides these materials with a greater ability for backbone reorganization upon plastic deformation.[163] Intriguingly, inclusion of the branched side chain leads to an increase in elastic modulus, suggesting that there may be increased interactions between the branched side chains on the TPD monomer and other side chains in the system. The higher elongation at break of PIDT$_{C16}$-TPD$_{C13B}$ compared to PIDT$_{C16}$-TPD$_{C8}$ is potentially due to the larger and branched side chain on the TPD$_{C13B}$ monomer shielding the backbone more than the linear side chain of the TPD$_{C8}$ monomer, enabling backbone motions. Moreover, by increasing the attachment density of alkyl side chains from every other to every monomer repeat unit, through inclusion of long alkyl side chains on the TPD unit, IDT copolymers can be made more extendable and make them feature a significantly

decreased elastic moduli. This may occur because of limited or hindered side chain interdigitation and thus more facile reorganization of the polymer backbone during elongation.

OFETs were fabricated so that the electronic properties of each IDT copolymer could be assessed. Measurements were averaged from at least five transistors across three substrates and devices, and the film thickness ranged from 20-30 nm. These results are shown in Figure 3-17. We believe that the high uncertainty seen in μ_{hole} in some samples reflects inhomogeneities in film thickness. All polymer samples display threshold voltages similar to our previous reports on IDT-copolymers.[157] When assessing average μ_{hole}, lengthening of alkyl side chains decreases the μ_{hole} and on/off current ratio in every case. The μ_{hole} of PIDT$_{C20}$-BT and PIDT$_{C16}$-BT remain on the same order of magnitude. In contrast, the μ_{hole} of PIDT$_{C16}$-TPD$_{C8}$ and PIDT$_{C16}$-TPD$_{C13B}$ are reduced by an order of magnitude compared to PIDT$_{C16}$-TPD$_{C1}$. It is observed that PIDT$_{C16}$-TPD$_{C1}$ and PIDT$_{C16}$-BT have the same OFET characteristics, which corroborates our previous reports.[155] One interpretation of decreases in μ_{hole} is that arrangements that enhance p-orbital overlap and facilitate intermolecular charge transport, including parallel chain alignment as found for PIDT$_{C16}$-TPD$_{C1}$, PIDT$_{C20}$-BT and PIDT$_{C16}$-BT, are hindered in PIDT$_{C16}$-TPD$_{C8}$ and PIDT$_{C16}$-TPD$_{C13B}$.[161] Accordingly, our data suggest that the inability of polymer side chains to interdigitate, and thus form 2D aligned structures, may be responsible for the decrease in μ_{hole} of PIDT$_{C16}$-TPD$_{C8}$ and PIDT$_{C16}$-TPD$_{C13B}$.

3.2.5 Conclusion

Increasing the side chain attachment density of IDT-copolymers from every other monomer unit to every monomer unit has widespread effects on electronic and mechanical properties of their thin films. With increased side chain attachment density comes an inability for side chains to interdigitate. This is supported by the absence of the (001) reflection in PIDT$_{C16}$-

TPD_{C8} and $PIDT_{C16}$-TPD_{C13B}. Consequently, these systems display order of magnitude less μ_{hole} than $PIDT_{C16}$-BT, $PIDT_{C20}$-BT, and $PIDT_{C16}$-TPD_{C1}, which do exhibit interdigitation of their side chains and thus display parallel and translational ordering of their backbones. In contrast, because of the lack of side chain interdigitation, $PIDT_{C16}$-TPD_{C8} and $PIDT_{C16}$-TPD_{C16} thin films can dissipate strain through plastic deformation; exhibiting greatly improved elongation at breaks and remarkably low elastic moduli. This suggests that side chain interdigitation is a major contributor to preventing polymer chain reorganization of IDT-copolymers while under strain. Inhibition of interdigitation can endow planar IDT-copolymers with reduced elastic moduli and the ability to deform plastically under strain.

3.3 The Impact of extended conjugation of IDT-based copolymers on strain charge mobility.

This chapter section contains material from a publication that is in preparation for manuscript submission and the author would like to acknowledge the contributions of all coauthors:

Lin, A., Lecroy, G., Sharif, A., **Guio, L**., Tran, H., Luscombe, C. K. Synthesis of thienopyrrolodione-based donor-acceptor polymers via direct arylation polymerization for improved mechanical and electrical properties. *Under Preparation*

Statement on Distribution of Work: The work done herein was a combination of efforts by all the authors. Specifically, I was responsible for the fabricating and testing organic field effect transistors and collection of hole mobility data and analysis. Angela Lin synthesized all polymers and collected polymer characterization data unless otherwise specified. Garrett Lecroy collected GIWAXS data and provided analysis. Adnan Sharif collected film-on-elastomer strain measurements. We are collaborating in the writing of the manuscript together.

3.3.1 Introduction

In the study in Chapter 3.2, the molecular structure of IDT-based copolymers was modified to increase the polymer deformability with the aim of also retaining good hole mobility. The acceptor unit was varied from BT to TPD, and alkyl side chains of various lengths were decorated on the TPD acceptor unit. The result was an increased side chain density on the backbone chain which disrupted side chain interdigitation. This disruption successfully caused an increase in deformability but came at the cost of electronic performance via hole mobility. A material that could retain and enhance both a low elastic modulus and high charge mobility is desirable.

One of the modifications to the IDT-based copolymer structure that has been used to tune the parameters of the polymer is that of the IDT backbone unit itself. One strategy employed is extending the pi-conjugated system of the fused ring structure by adding more fused aromatic rings. This has been done in multiple studies to modify IDT when coupled with a BT acceptor unit[162,172,173]. The impact of additional fused rings depended on the size of the addition and the order. For the polymer in which benzothiophene was added to the IDT core, the charge mobility decreased compared to the unmodified IDT_{C16}-BT. It was expected that the addition of more fused planar rings would increase the backbone planarity of the chain and reduce backbone chain disorder. However, it was found that the decrease in the side chain density created free volume leading to impurities in the side chains that lead to increased disorder. For the polymer in which only a thiophene ring was added to each side of IDT, there was a slight increase in hole mobility. It was found that there was no significant decrease in backbone disorder, except when the polymer films were annealed. In fact, after annealing at high temperatures, the chain disorder substantially decreases and the hole mobility increases. It appears that extending the IDT core unit by one thiophene does not disrupt the sweet spot of side chain density between too packed which disrupts interdigitation and too loose which introduces disorder. This paper takes inspiration from that work to improve the ordering of the $PIDT_{C16}TPD_{C8}$.

Another modification commonly employed in CP to improve their properties is controlling the molecular weight. Increasing molecular weight has been shown in various IDT-based polymers to increase both crack-onset strain and hole mobility. For those polymers, these improvements also came with an increase in the modulus of elongation, which is not desirable for elastic electronics. The polymers studied thus far for increased molecular weight all included the BT acceptor unit; the study has not been attempted at higher molecular weights with a TPD_{C8} unit which already

shows promise as a more elastic polymer (previous paper). The desire to maintain atom efficiency by using direct arylation polymerization (DArP) has traditionally limited the molecular weights achieved by the reaction. Recently, Lizuka *et al.* attained increased molecular weight and decreased defect formation in DArP reactions of donor acceptor copolymers by using a mixed-ligand approach[174].

In this study, the synthesis of IDT-based polymers by DArP is improved upon by using TMEDA as an additional ligand that allows the reaction to achieve much higher molecular weights. Two distinct IDT-copolymer systems are synthesized and investigated herein to determine the impact that an extended conjugated IDT core and increased molecular weight has on the strain characteristics and charge mobility of planar IDT-copolymers. The study aimed to decrease the side chain density displayed by $PIDT_{C16}$-TPD_{C8} with the addition of a core spacer in the form of fused thiophenes on each end of the IDT donor unit. It was expected that this modification would create additional space along the backbone, effectively decreasing the side chain density that was disrupting side chain interdigitation. It was expected that better interaction between polymers would improve hole mobility while at the same time still allowing the polymer to retain high deformability. Additionally, the increased molecular weight was expected to augment both hole mobility and deformability of the polymer as has been demonstrated for similar IDT-based systems. It was found that the increased molecular weight improves elasticity in the polymer systems as well as hole mobility. The extended IDT core system displayed increased chain ordering indicative of interdigitation, but it did not lead to a marketable increase in the hole mobility.

3.3.2 Materials

Chemicals used in this study were purchased from Sigma-Aldrich and Combi-Blocks and were used as received. The donor units (IDT and IDTT) were purchased from Derthon OPV Co Ltd and used as received. All reactions were carried out in air unless specified. Figure 3-18 shows

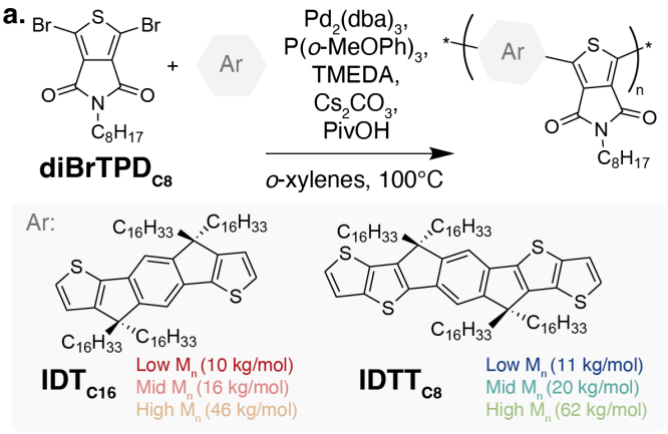

Figure 3-18: Reaction Scheme and molecular structure of TPD_{C8} (top). Molecular structures of the core donor unit of each polymer system and the synthesized molecular weights (bottom).

the typical DArP reaction scheme for IDT-based polymers with the notable addition of a TMEDA ligand. Higher molecular weights were achieved with a simple reaction scheme. Also shown are the molecular structures of the donor and acceptor units as well as the molecular weights achieved for each polymer system. Figure 3-19 shows the size exclusion chromatography (SEC) characterization and NMR spectra indicating the degree of polymerization along with images of the dry polymers. Synthetic details including monomer synthesis are omitted in this work and will be in the supporting information of the published article.

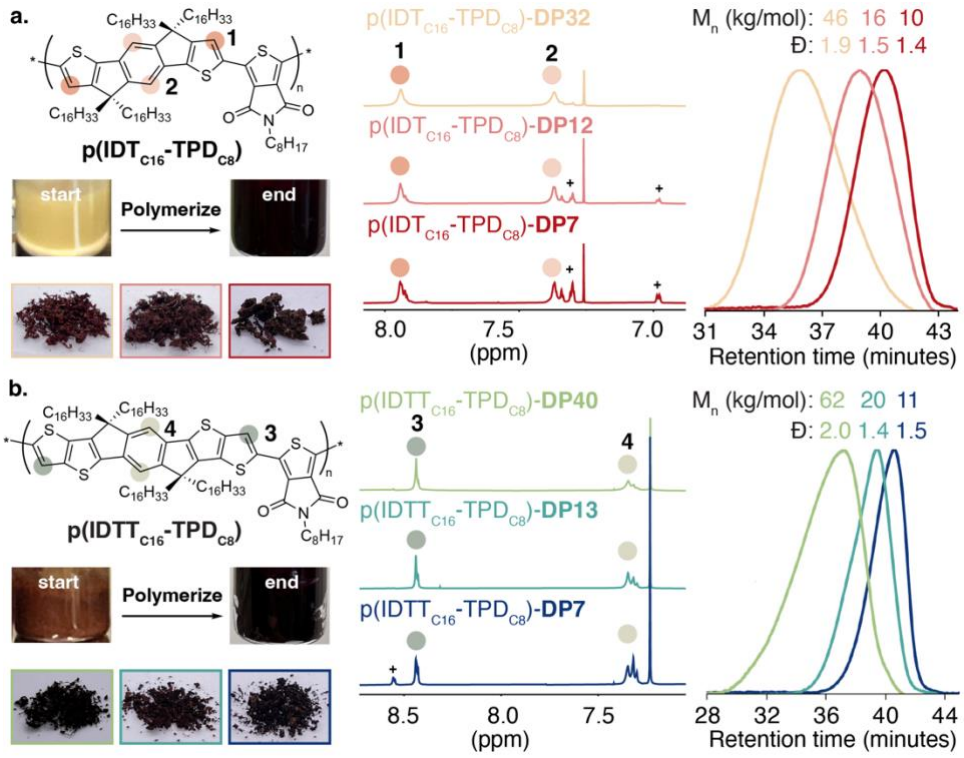

Figure 3-19: Pictures of the start and finish of the polymerization as well as pictures of the dry polymers at each molecular weight synthesized (left). Aromatic region of the NMR spectra for each polymer (middle). SEC profiles indicating molecular weight for each polymer (right).

3.3.3 Methods

NMR characterization

^{1}H NMR, HSQC, and HMBC spectra were collected on an Agilent DD2 NMR 500 MHz spectrometer with a dual resonance (OneNMR) probe and ^{13}C NMR spectra were collected on an Agilent DD2NMR 500 MHz spectrometer at 25°C equipped with a cryoprobe. HSQC spectra were collected with a gHSQC pulse sequence and the HMBC spectra were collected with a gc2HMBC pulse sequence. Quantitative ^{1}H NMR spectra for polymers were recorded on an Agilent DD2 NMR 500 MHz spectrometer at 25°C with a pulse angle of 90°. Quantitative ^{1}H NMR spectra was acquired after first performing an inversion-recovery T1 experiment (array = 15) to determine T1s for p(IDT-BT) (longest T1 = 3.6 seconds) and then setting the d_1 of consequent ^{1}H spectra to at least five times the length of the highest T1 measured to ensure full relaxation of signals

(p(IDTBT): d_1 = 20 seconds; p(IDTT-TPD$_{C8}$), p(IDT-TPD$_{C8}$): d_1 = 25 seconds). Chemical shifts for all NMR spectra are reported in parts per million (ppm) and referenced to residual protonated solvent ($CDCl_3$: δ 7.26 for ^1H and δ 77.16 for ^{13}C).

SEC characterization

The polymer molecular weights (vs. narrow dispersity polystyrene standards) were determined using a Tosoh EcoSEC High Temperature GPC system equipped with an RI detector at 135 °C, using 1,2,4-trichlorobenzene stabilized with BHT (0.015%) as the eluent at a flow rate of 0.5 mL/min. The polystyrene standards were purchased from Tosoh Bioscience LLC (oligomer kit) and a calibration curve built using A-2500, A-5000, F-1, F-2, F-4, F-10, F-20, F-40, F-80, and F-128. Data processing was performed using the EcoSEC Data Analysis software (version 1.14).

Optoelectronic measurements

UV-vis absorption spectra were measured on Agilent Cary 7000 UV-Vis-NIR Universal Measurement spectrophotometer (spectral range 170 - 3000 nm, double beam instrument) and a 100% transmittance sample was recorded as a blank using chloroform in a quartz cuvette. PL spectra were measured on a Horiba Fluorolog-3 spectrofluorometer with an excitation wavelength of 420 nm and emission spectra collected from 500 to 800 nm. Solution measurements were performed in chloroform solutions (polymer concentration: p(IDTT-BT) - 0.01 mg/mL; p(IDT-BT) and p(IDTT-TPD$_{C8}$) - 0.02 mg/mL; p(IDT-TPD$_{C8}$) - 0.06 mg/mL. Thin films used for solid-state absorption measurements were spin cast from a chloroform solution with a polymer concentration of 5 mg/mL onto 5 by 5 mm glass substrates.

Crystallographic measurements (GIWAXS)

Samples for GIWAXS measurements were prepared by spin-coating 5 $mgmL^{-1}$ polymer solutions in $CHCl_3$ onto lightly doped n-type silicon substrates with a native oxide layer. Polymer

solutions were stirred at 55°C overnight and filtered with 0.45-micron PVDF filters prior to spin-coating. Spin-coating was performed at 1500 rpm for 60 seconds, yielding films of ~50-60 nm thick. All sample preparation was performed in a nitrogen glovebox (O_2 < 0.5 ppm).

GIWAXS measurements were performed at Stanford Synchrotron Radiation Lightsource, SLAC National Accelerator Laboratory, Beamline 11-3. A flat area detector (Rayonix MAR-225) was used. The X-ray incident energy was 12.7 keV and an incident angle of 0.1° was used. GIWAXS data was corrected for geometric distortions imposed by the flat area detector and reduced/analyzed using a combination of Nika 1D SAXS and WAXStools software packages in Igor Pro.[1,2] All data is reported in terms of the scattering vector, Q where $Q = 4\pi \sin(\theta)/\lambda$ where θ is the scattering half angle and λ is the incident X-ray wavelength. All GIWAXS measurements were performed in a helium purged chamber to minimize X-ray air scatter and sample beam damage.

Charge transport property measurements

Heavily boron-doped silicon substrates with a 300 nm (± 5 nm) thick thermal oxide layer (University Wafer) as a gate dielectric were used for the thin-film field-effect transistors (FETs). Substrates were first scrubbed with detergent and water and then sonicated in DI water, acetone, and IPA for 15 min per solvent, followed by drying under a stream of compressed nitrogen. To passivate the thermal oxide, a self-assembled monolayer of octadecyl trimethoxy silane (OTMS) was deposited on the cleaned substrates using a literature technique with slight modifications.[3] The substrates were cleaned in a plasma cleaner for 15 min using air plasma. They were then quickly spin coated with a solution of 3 mM OTMS in trichloroethylene. The substrates were placed in a chamber that was being fed nitrogen through a bubbler with saturated ammonium hydroxide into the chamber overnight at room temperature and ambient pressure. The substrates were rinsed with

toluene and then isopropyl alcohol for 5 minutes each to remove any physiosorbed ODTS from the surface, followed by drying under a stream of compressed nitrogen. Polymer solutions were stirred at 55°C overnight and filtered with 0.45-micron PVDF filters prior to spin-coating. The polymer layer was then spin-coated from a 5 or 10 mg/mL solution of each polymer in $CHCl_3$ at 2000 RPM for 60 s onto the OTMS passivated substrates in a nitrogen environment. Gold electrodes were thermally evaporated onto the active layer to a thickness of 100 nm at a rate of 0.5 Å s^{-1}. The gold was evaporated from an alumina coated molybdenum boat and the electrodes were deposited through a shadow mask. After electrode deposition, the devices were tested for charge mobility, threshold voltage and current on/off ratio. The devices had a top-contact bottom-gate architecture with a channel width of 1000 µm and a channel length of 50 µm. They were tested in a nitrogen atmosphere using a Signatone Probe Station and two Keithley 2400 Source-Measure units. The transfer curves were collected in the saturation regime, where the linear section of the curve was fitted to estimate the charge mobility using the following equation:

$$I_D = \frac{WC\mu}{2L}(V_G - V_T)^2$$

where I_D is the drain-source current; µ is the charge mobility; W is the channel width; L is the channel length; C is the capacitance per unit area of the insulator (SiO2, 300 nm, 10 nF·cm^{-2}). V_G is the gate voltage; and V_T is the threshold voltage. The threshold voltage was obtained by fitting the linear region of the I_D vs V_G curve and extrapolating to $I_D = 0$. Measurements were averaged from at least five transistors.

Film-on-elastomer: Crack onset strain and buckling measurements

PDMS (Sylgard 184, Dow Corning) was prepared by vigorously mixing the base resin and the curing agent in 20:1 (by weight) ratio, pouring into a Petri dish, and leaving under dynamic

vacuum at ambient temperature for 2 hours before curing at 65 °C for 12 h in an oven. The PDMS strips were then cut (4 cm x 1 cm x 0.5 cm) with a scalpel.

Bare Si wafers were cleaned with acetone, MeOH, and DI water and then dried under vacuum before being plasma treated (ambient air, 150 mTorr, 3 minutes; PE-50 Plasma Etcher). The substrates were then spin coated with 3 wt% PSS (aq. DI water, 120 uL) at 4000 rpm for 60 seconds and annealed at 80°C for ~10 seconds to drive off remaining water. Polymer solutions were prepared by dissolving in anhydrous chlorobenzene at a 10 mg/mL concentration and stirred on a hot plate with a magnetic stirrer at 50°C for 2-4 hours before filtering through a 0.22 μm PTFE filter. Filtered polymer solutions were spin cast onto the Si wafers (drop on and then spin coat, not annealed) at 1500 rpm for 60 seconds.

For crack onset strain measurements, the polymer thin films were transferred to the PDMS by pressing the Si wafer onto the PDMS strip and then submerging it into a DI water bath. After 5-30 minutes (depending on sample), the PDMS sample was removed from the water bath and the Si wafer carefully removed with tweezers to give the thin film polymer on the PDMS. The sample was dried in a desiccator under dynamic vacuum for 2 hours before loading onto a homemade strain stage. The formation of cracks was observed using an optical microscope (Zeiss Axio Imager.A2m) incrementally from 0 to 100 % strain to relaxation.

For buckling measurements, the same protocol for film transfer was followed except the PDMS was pre-strained to 2% strain before transferring the polymer thin film. The strain was removed right before imaging to avoid potential stress-relaxation and/or reduction in amplitude of the buckles. The thickness of each polymer film (d_f) was measured using AFM (Bruker, ICON). The elastic modulus of the PDMS was measured using a CellScale Univert S Mechanical Test

System (4.5 N load cell) and obtained from the slope of the linear fit of the stress-strain curve in the elastic region. The average elastic modulus (E_f) was calculated from the equation below:

$$E_f = 3E_s\left(\frac{1-v_f^2}{1-v_s^2}\right)\left(\frac{\lambda_b}{2\pi d_f}\right)^3$$

Where v is Poisson's ratio, E is the elastic modulus, and λ_b is the measured wavelength of the buckles in the film. *S* and *f* denote the values for the film and the substrate (PDMS).

3.3.4 Results and Discussion

GIWAXS measurements allow us to probe the crystalline and lamellar morphology as well as small spatial interactions between polymer chains such as evidence of interdigitation. Figure 3-20 shows the 2D GIWAXS curves for both sets of materials along with in-plane and out-of-plane linecuts. Both sets of materials display broad out-of-plane π-stacking scattering peaks arising from (0k0) planes. In-plane π-stacking is difficult to deconvolute from the diffuse scatter apparent

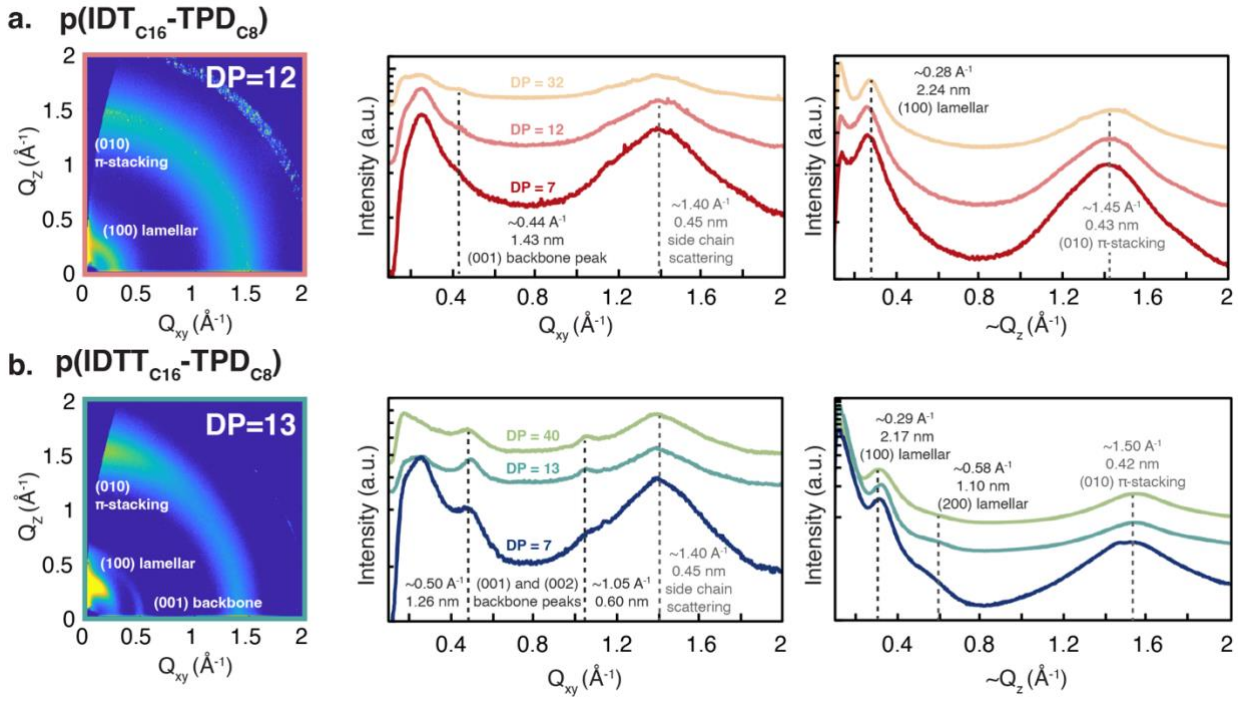

Figure 3-20: 2D GIWAXS spectra (left) and linecuts of the 2D GIWAXS spectra in the Qxy direction (in-plane, middle) and Qz direction (out-of-plane, right) of each IDT-copolymer is shown. Major peaks are labeled for clarity.

at ~1.4 $Å^{-1}$ for both sets of materials. This has been attributed to scattering arising from the disordered alkyl side chains[40]. PIDTT$_{C16}$-TPD$_{C8}$ shows π-stacking scattering peaks in the out-of-plane direction at 1.54 $Å^{-1}$, indicative of d-spacing of ~4.1 Å, matching closely with the reported π-stacking distance for PIDT$_{C16}$-BT[40,65]. PIDT$_{C16}$-TPD$_{C8}$ shows broad out-of-plane π-stacking scattering peaks at a reduced Q of ~1.42-1.45 $Å^{-1}$, corresponding to spacing of ~4.3-4.4 Å) in line with study in section 2 of this chapter[175]. The predicted π-stacking of IDT-based polymers occurs as a crisscrossing of polymer chains at the acceptor unit. The extension of the IDT core was expected to decrease side chain density, allowing for more closer interactions between chains. The reduced π-stacking is a promising indication. The π-stacking distance decreases slightly going from the low to the high molecular weight batches in PIDT$_{C16}$-TPD$_{C8}$. π-stacking structural coherence is low for both PIDTT$_{C16}$-TPD$_{C8}$ and PIDT$_{C16}$-TPD$_{C8}$ (~3-5 pi-stacks), indicating little long-range interchain ordering as is expected from IDT-based polymers.

Lamellar structural coherence is low as well for both PIDTT$_{C16}$-TPD$_{C8}$ and PIDT$_{C16}$-TPD$_{C8}$. PIDT$_{C16}$-TPD$_{C8}$ out-of-plane lamellar spacing of ~22-23 Å is larger than that of PIDTT$_{C16}$-TPD$_{C8}$ (~20 Å), and both sets of material have smaller lamellar spacing than that of PIDT$_{C16}$-BT[40,65,176], possibly indicating less volume occupied by the side chains in PIDTT$_{C16}$-TPDC8 and PIDT$_{C16}$-TPD$_{C8}$. The lamellar peak is also present in the in-plane linecuts, indicating that both polymer systems have no preferential orientation relative to the film plane. The reduced lamellar spacing in the extended core polymer system could be indicative of increased interdigitation caused by decreasing side chain density as interdigitation would allow the polymer chains to come slightly closer together. Interestingly, there is a broad shoulder out-of-plane at ~0.58 $Å^{-1}$ in PIDTT$_{C16}$-TPD$_{C8}$ that is most prominent in the medium molecular weight batch that possibly arises from a 2nd order lamellar feature.

PIDTT$_{C16}$-TPD$_{C8}$ displays strong in-plane scattering features at ~0.50 Å^{-1} and ~1.05 Å^{-1}, corresponding to a spacing of 12.6 Å, assigned to scattering from polymer backbone ordering along (00l) planes. This ordering is most pronounced in the medium molecular weight batch as evidenced by the largest estimated structural coherence (~4.7 scattering planes). PIDT$_{C16}$-TPD$_{C8}$ shows a weak in-plane scattering feature at 0.44 Å^{-1} (14.1 Å) in the high molecular weight batch also assigned to scattering from polymer backbone ordering. Scattering arising from backbone ordering requires some degree of *inter*chain registry, and thus does not necessarily arise from scattering features that correspond precisely to monomer-monomer repeat distances. The re-appearance of this peak, which is missing in the low molecular weight non-extended core polymer system was attributed to translational order for the polymer systems in the previous section of this work and is indicative of increased interdigitation. The assignment of exact physical features to the backbone scattering is highly dependent on how polymer chains are aligned relative to each other[65,177]. Given the larger monomer units of PIDTT$_{C16}$-TPD$_{C8}$ compared to PIDT$_{C16}$-TPD$_{C8}$, but *shorter* backbone scattering feature of $D_{(001)}$ = 12.6 Å for PIDTT$_{C16}$-TPD$_{C8}$ compared to $D_{(001)}$ = 14.1 Å for PIDT$_{C16}$-TPD$_{C8}$, it is a reasonable hypothesis that PIDTT$_{C16}$-TPD$_{C8}$ might have preferential interchain crossing angles that are more shallow than those of PIDT$_{C16}$-TPD$_{C8}$.

The UV-Vis absorption and photoluminescence (PL) spectra of all polymers in solution and thin films are shown in Figure 3-21. The maximum absorption wavelength for each spectrum as well as the calculated Stokes shift, $I_{0\text{-}1}/I_{1\text{-}1}$ ratio, and aggregation shift are presented in Table 3-2. The 0-1 transition and 0-0 transition are related to aggregated and unaggregated chains,

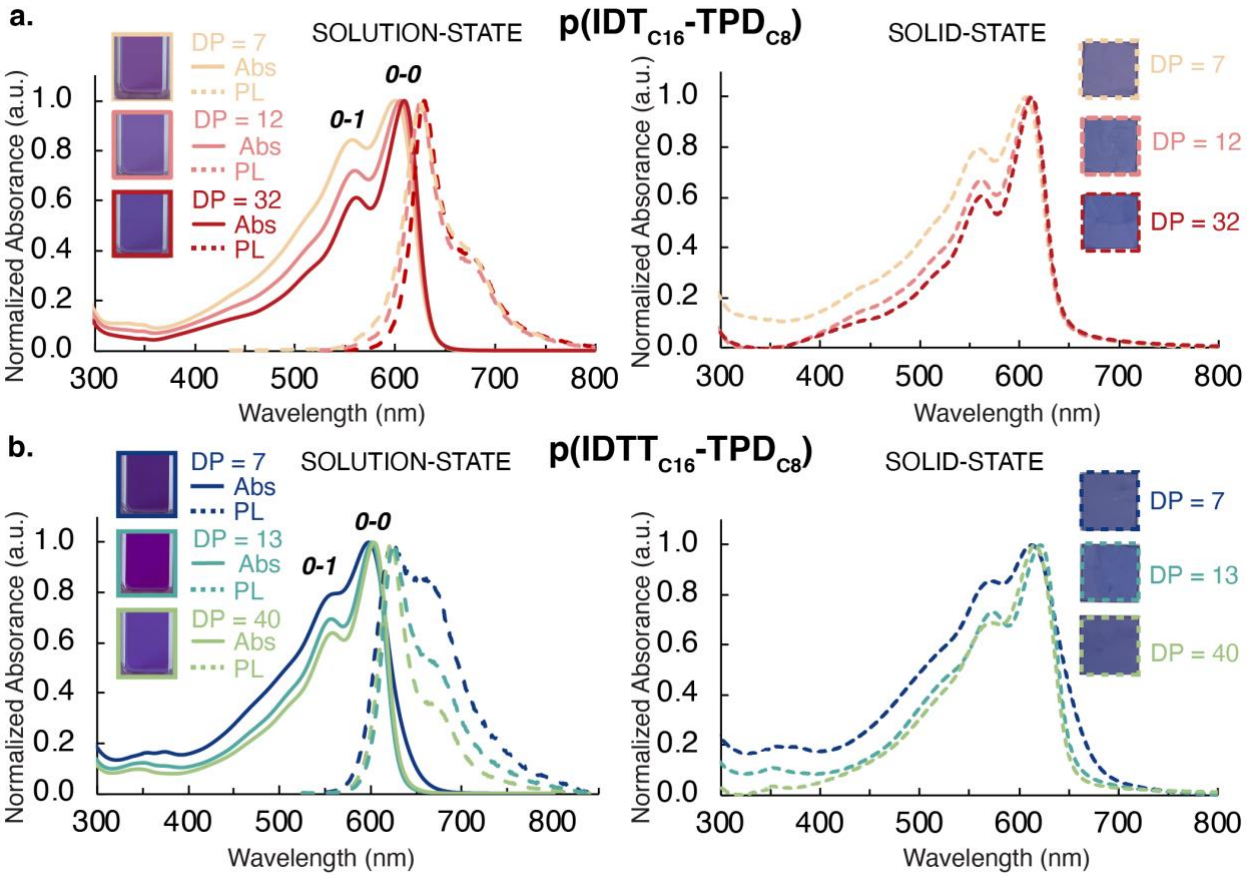

Figure 3-21: (Left) Absorption and photoluminescent spectra for polymers in solution marked by solid and dashed lines, respectively for (a) PIDT$_{C16}$-TPD$_{C8}$ and (b) PIDTT$_{C16}$-TPD$_{C8}$. (Right) Absorption spectra of cast thin films for each polymer system.

respectively ,and the ratio of their intensities ($I_{0\text{-}1}/I_{1\text{-}1}$) is related to the degree of interchain aggregation present[178]. For all polymers the 0-0 transition is pronounced, indicative of heavily favored J-aggregation behavior. The peak wavelength of the 0-0 transition sees a slight blueshift in PIDTT$_{C16}$-TPD$_{C8}$ compared to PIDT$_{C16}$-TPD$_{C8}$ which can be attributed to a change in the donor-acceptor hybridization levels brought on by the extension of the IDT core. There is also a slight

redshift in both polymer systems according with increasing molecular weight, indicating an increase in the effective conjugation length. The Stokes shift is related to the relaxation of the molecular excited state and the electronic-vibrational modes. This means that a higher molecular rigidity leads to smaller Stokes shifts[179]. For both polymer systems the Stokes shift is lower than that of PIDT$_{C16}$-BT as established in the previous study. For both systems, there is a slight decreasing of the Stokes shift with increasing molecular weight indicating a slight increase in backbone rigidity with longer chains. Compared to each other, however, there is no significant change in the stokes shift, and therefore the extended conjugation of the IDT core does not significantly later backbone rigidity. $I_{0\text{-}1}/I_{1\text{-}1}$ for PIDTT$_{C16}$-TPD$_{C8}$ compared to PIDT$_{C16}$- TPD$_{C8}$ across the same molecular weights is identical in the solution state, indicating little difference in aggregation. However, for both systems, the increasing molecular weight leads to increasing

		Solution-state				Solid-state	
	DP	$\lambda_{max,abs}$ (nm)[a)]	$\lambda_{max,PL}$ (nm)[b)]	Stokes shift (nm)	$I_{0\text{-}0}/I_{0\text{-}1}$	$\lambda_{max,abs}$ (nm)[c)]	$\Delta_{solution\ to\ thin\ film,\ abs}$ (nm)
PIDT$_{C16}$-TPD$_{C8}$	7	601	624	23	1.2	607	6
	12	606	625	19	1.4	611	5
	32	609	629	20	1.7	613	4
PIDTT$_{C16}$-TPD$_{C8}$	7	597	623	26	1.3	613	16
	13	601	622	21	1.4	621	20
	40	603	626	23	1.6	616	13

Table 3-2: Optical spectroscopy peak characteristics and calculated figures for each polymer system and molecular weight derived from the optical spectra shown in Figure 3-21: (Left) Absorption and photoluminescent spectra for polymers in solution marked by solid and dashed lines, respectively for (a) PIDT$_{C16}$-TPD$_{C8}$ and (b) PIDTT$_{C16}$-TPD$_{C8}$. (Right) Absorption spectra of cast thin films for each polymer system.

aggregation in the solution state, which agrees with the general trend of high molecular weight polymers inducing more aggregation in solution. The most interesting feature of the optical

characterization is the shift in peak absorption wavelength when going from solution to thin film, referred to here as aggregation shift. The aggregation shift for the extended core polymers is twice that of the unmodified PIDT$_{C16}$- TPD$_{C8}$, indicating that they adopt a much higher degree of planarization in the solid state. This behavior is very similar to that seen in the thiophene extension of the IDT core for PIDT$_{C16}$-BT[172], where the extended core led to a polymer that would improve its aggregation upon being annealed. A future study probing the effects of high temperature annealing of PIDTT$_{C16}$-TPD$_{C8}$ on strain and charge mobility would help in expanding on this

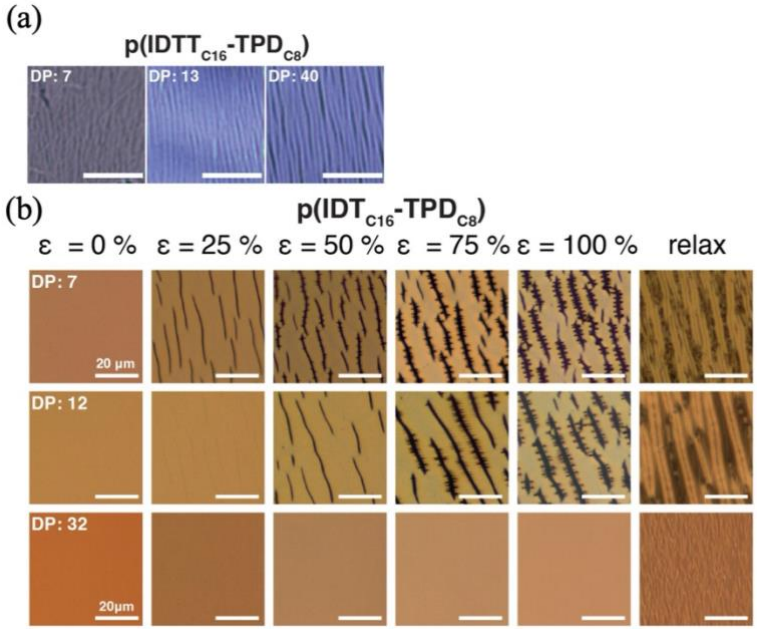

Figure 3-22: Representative optical microscopy images of buckling for elastic modulus determination (a) and cracks for determination of crack-onset-strain (b). All scale bars are 20 micrometers. ε is the strain of each film upon capturing the image.

finding.

Film-on-elastomer tensile measurements were performed to quantify and compare the mechanical properties of the IDT-copolymers. Figure 3-22 shows representative optical microscopy images of the film-on-elastomer characterization from which the data in Table 3-3 are extracted. Both PIDT$_{C16}$-TPD$_{C8}$ and PIDTT$_{C16}$-TPD$_{C13B}$ were able to undergo plastic deformation during elongation at all molecular weights. For PIDT$_{C16}$-TPD$_{C8}$, the low and middle molecular

weights displayed very little elongation at break, which is surprising given that the same moelcualr weight polymer achieved CoS of 7% in the previous study. It is possible that better measurements are obtained using the film-on-water measurements used previously. The high molecular weight PIDT$_{C16}$-TPD$_{C8}$ CoS of >100% is a significant improvement and accomplishes the elasticity that this study set out to achieve. The elastic moduli of the PIDT$_{C16}$-TPD$_{C8}$ polymer system and the PIDTR$_{C16}$-TPD$_{C8}$ system at all molecular weights are low and consistent with the previously attained figures. Increasing molecular weight for both polymer systems is correlated with an increasing elastic modulus which was expected given the results with other IDT-based polymers in the literature. PIDRT$_{C16}$-TPD$_{C8}$ maintains a low elastic modulus even at high molecular weight. However, the CoS of less than 2% at low and medium molecular weights and only 40% at the high molecular weight are indicative of a much more brittle film. From a structural perspective, it is the decreased density of alkyl side chains on PIDTR$_{C16}$-TPD$_{C8}$ that allows for side chain order (i.e., side chain interdigitation), which in turn reduceds the material's ability for backbone reorganization upon plastic deformation.

Polymer	DP	E (MPa)	CoS (%)
PIDT$_{C16}$-TPD$_{C8}$	7	7 ± 2	ca. 2
	12	12 ± 1	ca. 5
	32	16 ± 3	> 100
PIDTT$_{C16}$-TPD$_{C8}$	7	22 ± 1	< 2
	13	29 ± 6	< 2
	40	40 ± 6	ca. 40

Table 3-3: Calculated mechanical properties for all polymers extracted from film-on-elastomer optical microscopy images.

OFETs were fabricated so that the electronic properties of each IDT copolymer could be assessed. Measurements were averaged from at least five transistors across three substrates and devices, and the film thickness ranged from 20-30 nm. Box plots of the measured devices are shown in Figure 3-23. The hole mobility of the low molecular weight PIDT$_{C16}$-TPD$_{C8}$ was unable

to be measured in the fabricated devices due to a low signal to noise ratio due to the hole charge mobility. When assessing average μ_{hole}, the extension of the IDT core shows no change when comparing equivalent molecular weights, and the charge mobility of both polymers is significantly

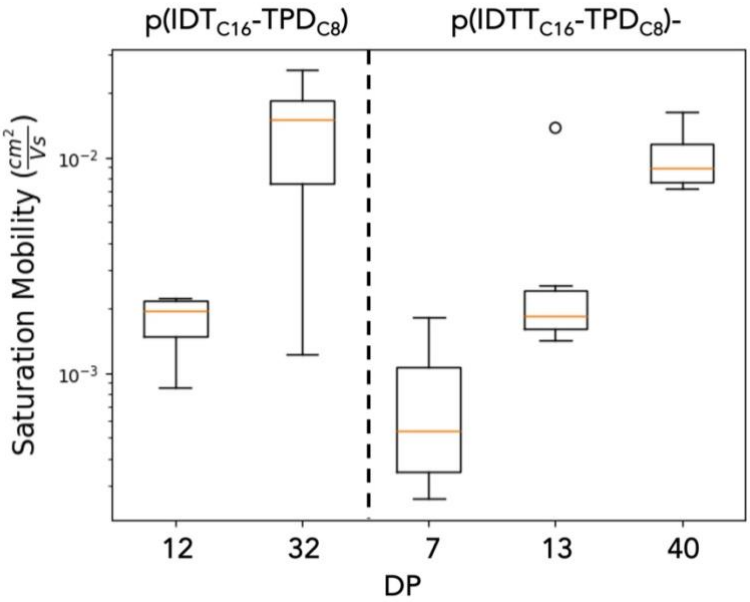

Figure 3-23: OFET hole mobility (μ_{hole}) for the polymer systems explored in this work. The low molecular weight (DP = 7) PIDT$_{C16}$-TPD$_{C8}$ displayed such low mobility that it could not be measured with our instruments.

reduced compared to that of PIDT$_{C16}$-BT in the previous study. For both polymers, the increase in molecular weight is accompanied by a significant increase μ_{hole} indicating that extended chain lengths for all IDT based polymers improves electronic performance. Arrangements that enhance p-orbital overlap and facilitate intermolecular interactions, including parallel chain alignment which was improved in PIDTT$_{C16}$-TPD$_{C8}$ were expected to improve μ_{hole}. The lack of improvement in μ_{hole} is indicative that there is another molecular arrangement besides improved interdigitation that plays a more important role in the overall charge transport in IDT-based polymers. A reasonable hypothesis is that the primary driver for interchain charge transport is the crisscrossing overlap pi-stacking of the acceptor units as indicated by molecular dynamic simulations. The addition of the side chain on the acceptor unit would thus hinder this interaction and lead to

decreased interchain charge transport. However, because of the infrequent and difficult to detect nature of this interaction, it cannot be confirmed with the characterizations presented in this paper.

3.3.5 Conclusions

Two molecular structure modifications of an IDT-based polymer were explored in this study. $PIDT_{C16}$-TPD_{C8} was altered in molecular weight using a ligand additive to the traditional DArP synthesis. The IDT core was extended in conjugation by adding a fused thiophene ring to each side in the monomer synthesis. The impact of increased molecular weight led to improved electronic performance for both polymer systems, which was accompanied by an increased elastic modulus. Increasing chain length leads to more entanglements with other chains which augments the number of π-stacking interactions, while also requiring less of them for long-range charge transport. However, decoupling the increase in chain entanglement with increasing elastic modulus is difficult, leading to stiffer polymers with increasing molecular weight. The impact of the decreased side chain density caused by increasing the monomer length was felt in the molecular ordering of the backbones. GIWAXS indicated an increase in interdigitation, and translational order. This was met with a drastic decrease in the % elongation at break of the films, although the elastic modulus was not as heavily impacted. Lastly, the charge transport of the extended core polymers did not improve, indicating that the disruption to overall charge percolation may be caused by another source, namely the steric hindrance of the side chain on the acceptor unit. Future work remains to further understand this mechanism, as well as exploring film processing techniques that have been shown to modify the morphology of other IDT-based polymers with increased conjugation monomers.

Chapter 4. The Impact of Processing Conditions on the Aggregation Behavior and Charge Mobility of Indacenodithiophene Semiconducting Polymers.

This chapter section contains material from a publication that is under preparation for journal submission and the author would like to acknowledge the contributions of all coauthors:

Guio, L., Sommerville, P., Pozzo, L. D. Luscombe, C. The Impact of Solvent Processing on the Aggregation Behavior and Charge Mobility of Indacenodithiophene Semiconducting Polymers. *Macromolecules, Under Preparation.*

Statement on Distribution of Work: The work done herein was largely done by me. Dr. Parker Sommerville synthesized the polymers used in this study.

4.1 Introduction and Motivation

The morphological characteristics of conjugated polymers are directly linked to their performance. The mechanisms by which processing conditions impact the final material microstructure will in turn impact its properties. Developing an understanding of these mechanisms will help guide design better processes for tailored material properties to address specific application needs. It has been shown for many semiflexible CP such as P3HT and DA copolymers such as poly[2,5-(2-octyldodecyl)-3,6-diketopyrrolopyrrole-alt-5,5-(2,5-di(thien-2-yl))thieno[3,2b]thiophene] (DPPDTT) that processing conditions significantly alter film morphology and therefore physical properties of the material[180–184]. For CP, the chain conformation and aggregation state in dilute solution (and intermediate structures formed during solution processing) transfer to the solution-cast films, affecting the optoelectronic properties. P3HT can be aged in marginal solvents to develop nanowires with increased crystallinity and long-range order which improves its charge transport[181]. The Pozzo group studied the aggregate

structures of DPPDTTT as a function of solvent interactions[184]. By mixing a poor solvent into the DA copolymer solution originally composed of good solvent, they were able to induce the formation of nanofibrils. Interestingly, this formation of nanoribbon aggregates would only occur when the poor solvent used was polar, as nonpolar poor solvent addition resulted in amorphous aggregates. The electronic performance of OFETs fabricated from nanoribbon solutions showed improved hole mobility. Through these and other developments, certain microstructural properties have been identified as impactful in CP morphology: chain conformation and packing, orientation and coherence length of the nanoscale domains and aggregation structures and sizes. More importantly, research has shed light on the impact of critical solution processing parameters such as solvent polarity and aromaticity, aging time, and dissolution temperature[185].

A better understanding of possible aggregation structures such as nanowires and the dynamics by which they are formed have paved the way for other techniques that have allowed further improvements. For example, the understanding of the nucleation and growth mechanism by which P3HT nanowires form has paved the way for other techniques such as the ultrasonication of polymers in solution which generates pre-aggregated crystals that serve as nanowire growth sites. It has also been shown that variations in the kinetics of aggregation lead to different morphologies, and in turn, different functional properties. The crystal domain sizes of P3HT nanowires are dependent on the temperature in which they are aged, indicating a direct dependance on growth kinetics and thermodynamics[183]. DA copolymers share a similar correlation with aggregation kinetics. It has been shown that higher boiling point solvents improve the charge mobility of films fabricated from donor acceptor copolymers. This is due to an increased time to aggregation that allows the polymers to better self-assemble. However, this relationship is material

dependent as other polymers have shown improved performance when the solution is rapidly aggregated.

Poly-Indacenodithiophene-Benzothiadiazole ($PIDT_{C16}$-BT) is an exemplary polymer in a new class of rigid and planar donor-acceptor copolymers which have demonstrated high field effect mobility without requiring high crystallinity and identifiable long-range order. The rigid and planar polymer chain conformation induced by intrachain molecular interactions makes $PIDT_{C16}$-BT resistant to morphological changes. The UV-Vis spectra of the polymer in solution compared to the thin film spectra is significantly less redshifted when compared to other polymers such as P3HT and even DA copolymers such as DPPDTT which indicates that it doesn't change conformation significantly upon aggregation[176]. Scott et al. studied the chain stiffness of a variety of donor-acceptor copolymers using small angle scattering[186] including $PIDT_{C16}$-BT. It was shown that the intermolecular interactions between the donor and acceptor units leads to a persistence length that is orders of magnitude higher than that of typical rigid rod donor acceptor polymers. A lower degree of conformational freedom (associated with high persistence length) hinders the chain segments in achieving higher crystallinity.

Recently, progress has been shown in developing processing methods by which the morphology of IDT-based polymers can be controlled. Typically, solvent interactions with the polymer are tuned to develop favorable solution aggregates for final film structure. Various studies have changed solvent properties such as polarity, aromaticity and even used Hansen solubility parameters to understand how the solvent-polymer interactions lead to different morphologies. However, these works typically observe the overall interaction between polymer and solvent. Recently, research has begun to observe the interactions between the solvent and the polymer backbone and side chains separately. Jin et al. studied the impact that various solvents have on the

solution aggregation of PIDT$_{C16}$-BT. They picked solvents based on the difference between their interaction with the polymer side chains and the backbone, separately. The study showed that solvents with intermediate interaction between side chain and backbone lead to a rapid chain aggregation during casting which resulted in improved charge mobility in the final solution-cast films.

The impact of solution conditions of IDT-based polymers on their aggregation behavior has not been sufficiently studied and could lead to significant improvements in their use for flexible electronic applications. This study investigates the solution state conformation of IDTC$_{16}$-BT and the aggregation behavior of the polymer as it transitions from dilute solution to aggregation to the solid film. Solvents were chosen based on the calculated interaction parameter using the Hansen solubility parameters. The chain state and aggregation behavior were observed at three concentration regimes. Absorption spectroscopy was used to probe the chain state in dilute solutions. Small angle X-ray scattering (SAXS) was used to probe the aggregation state in the semi dilute and aggregated regimes. It was found that solvent interactions significantly impact aggregation speed and sizes in all regimes. However, these structures showed no significant impact on the charge mobility of the final solution-cast films.

4.2 Materials and Methods

PIDT$_{C16}$-BT was synthesized by direct arylation polymerization (DArP) and purified according to the synthetic procedure and work up specified in Chapter 3.2. Polymer molecular weight was measured by GPC using THF as the eluent and polystyrene as the standard. The number-average molecular weight (M_n), weight-average molecular weight (M_W), and polydispersity index (M_W/M_n) were 16 kDa, 27 kDa, and 1.69, respectively. Anhydrous toluene,

tetrahydrofuran, chloroform, and anisole were purchased from sigma Aldrich. All solvents were used as received.

4.2.1 Small Angle X-Ray Scattering

Polymer thermal history plays a major role in the aggregate structures that persist in solution and in the final film morphology. Due to this, it is important that all samples be treated with the same thermal history. Varying amounts of $PIDT_{C16}$-BT were weighed in individual vials and dissolved in anhydrous solvent by heating the sealed vials to 90% of the solvent's boiling point for 2 hours. Because of the variety in compatibility between solvent and solute, it is possible that larger aggregates persist in the solution state even after heating dissolution, so care was taken to not filter out these potentially larger aggregates. Different concentrations of solution were made that ranged from 1 to 5 weight percent of $PIDT_{C16}$-BT in three solvents: anisole, tetrahydrofuran, and toluene. The capillaries used were 1.5 mm quartz Charles Supper capillaries. SAXS experiments were performed on a XEUSS 3.0 (Xenocs, Grenoble, France) using Cu Kα radiation. Care was taken to align the beam and detector to a specific point on the capillaries to reduce capillary thickness differences. Since the X-ray beam spot is not a point, the actual beam path length through the capillary is not the diameter of the capillary and is not trivial to define. More accurate estimation of the thickness (averaged beam path length) of water in the capillary can be done by measuring the transmissions of water in the capillary and empty capillary and using the known mass attenuation coefficient of water. The transmission of a homogenous sample can be described as

$$T = \frac{I_0}{I_t} = e^{\varepsilon \rho d}$$

where I_o and I_t are the intensities of incident beam and transmitted beam, respectively. ρ and d are the density and thickness of the sample, and ε is the mass attenuation coefficient of the

sample. The mass attenuation coefficient for water at a photon energy of 8 Kev is 10.37 (cm^2/g) according to http://physics.nist.gov/PhysRefData/XrayMassCoef/ComTab/water.html. The density of water is $1g/cm^3$. Capillary measurements with and without water were taken and the calculated thickness for each capillary was used in the reduction of the 2-dimensional scattering data prior to solvent subtraction. To obtain temperature dependent SAXS measurements, a Linkam HSFX350 high-temperature stage was used. Data reduction was performed with XSACT software (Xenocs) by azimuthally integrating 2D images to obtain 1D scattering profiles. The data was normalized to thickness and corrected for background. The absolute intensity solvent measurement was subtracted from the solution measurement after correcting for displaced volume effects.

4.2.2 UV-Vis Absorption Spectroscopy

UV-Vis absorption spectra were measured on a Perkin Elmer Lambda 950. Solution measurements were performed in each solvent with polymer concentration of 0.05 weight percent. The solutions were made by first dissolving the polymer at 90% of the solvents' boiling point and then allowing to cool. Temperature dependent absorption spectra were obtained by using the Quantum Northwest CD 250/E temperature-controlled cuvette holder. Measurements were taken using a 1mm path length quartz cuvette and the polymer solutions were corrected for background by subtracting the pure solvent spectra before analysis.

4.2.3 Charge Transport Measurements

OFET devices were made from 1.0 weight percent solutions of IDTBT in each solvent. The polymers were dissolved in each solvent by being brought to 90% of the solvent's boiling point for 2 hours in a nitrogen atmosphere before allowing to cool and subsequent spin coating onto the treated substrates. The full procedure and characterization are the same as mentioned for Chapter 3.3.

4.3 Results and Discussion

4.3.1 Aggregation Behavior

Temperature varying UV-Vis absorption spectra were taken of the polymer dissolved in various solvents to understand the chain aggregation behavior in the dilute regime. Figure 4-1 shows the temperature dependent spectra for a solution of 0.05 weight percent PIDT$_{C16}$-BT in Toluene. The solutions were first taken to the highest temperature which was 90% of the boiling

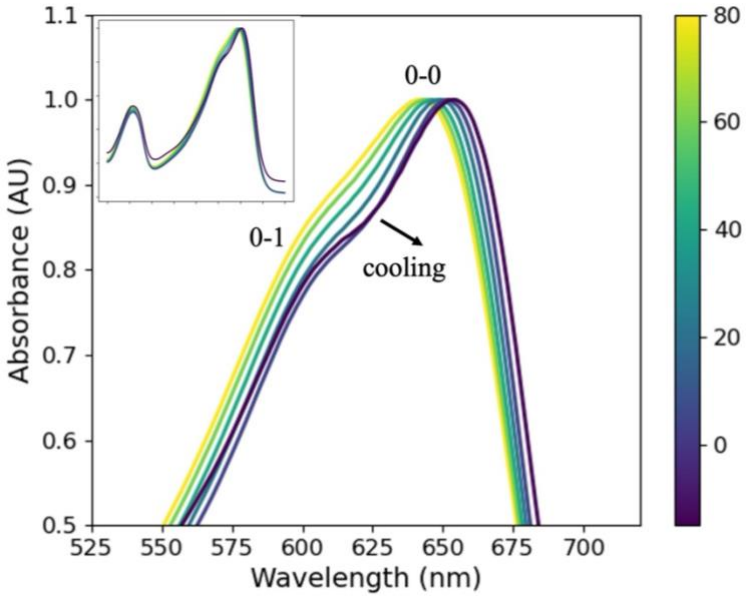

Figure 4-1:UV-Vis Spectra of 0.05 weight % of IDT$_{C16}$-BT dissolved in Toluene at various concentrations. The spectra were first taken at high temperature for full dissolution and then cooled. The inset image shows the full spectrum. The 0-0 and 0-1 transitions are labelled, respectively.

point of the solvent and held for 5 minutes before taking measurements. As the solution cools, the chains begin to planarize as indicated by a redshift in the wavelength at peak maximum (λ_{max}). The 0-1 transition shoulder also becomes more prominent, indicating a higher degree of aggregation. Figure 4-2 shows the comparison of the UV-Vis spectra for different solvents. At every temperature, the λ_{max} of THF is higher than that of toluene. This would indicate a higher degree of planarization of the polymer in that solvent. One would expect this to coincide with a more prominent 0-1 transition. However, toluene shows a more prominent transition peak than

THF. This could be indicative of aggregation structures beginning to form in Toluene, although the chains are not as planar. To understand how the solvent impacts the degree of aggregation, λ_{max} was plotted as a function of temperature for each solvent, and a linear model fit to the points. The resulting slope indicates the impact of decreasing thermodynamic solubility that the polymer experiences in each solvent. As expected, due to it being a poorer solvent, the polymer dissolved

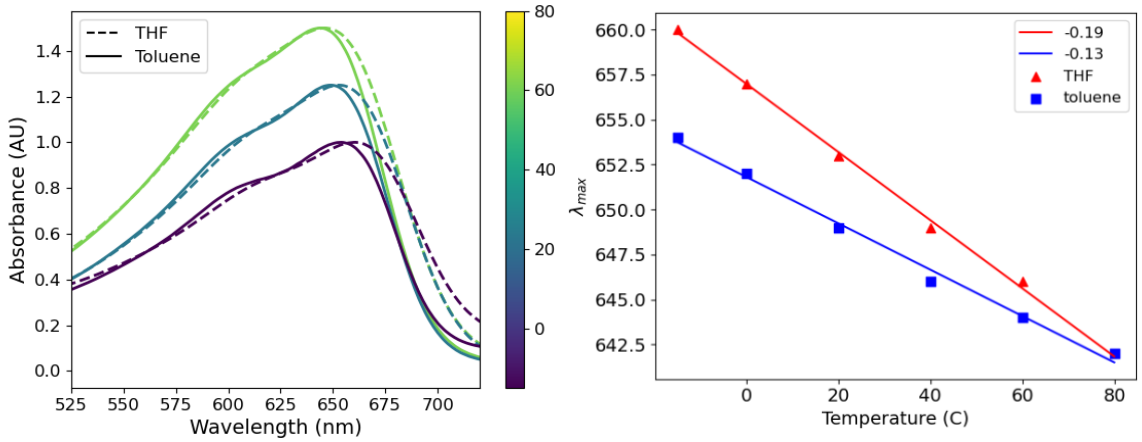

Figure 4-2: UV-Vis Absorption Spectroscopy data comparing select temperatures of 0.05 weight percent PIDT$_{C16}$-BT in toluene and THF (left). λ_{max} plotted as a function of temperature for each solvent. The fitted lines' slope is indicated in the legend (right).

in THF experiences increased aggregation as a function of decreasing temperature.

Temperature varying SAXS profiles were taken to determine the aggregation structures and behavior of PIDT$_{C16}$-BT in semi dilute and aggregated regimes. Figure 4-3 shows the temperature varying SAXS profiles in log-log plots of 1.0 weight percent PIDTC$_{16}$-BT in toluene solutions with temperatures ranging from -15 C to 80 C. In the middle-*Q* region, rigid rods are present due to scattering closely following a Q^{-1} dependance. Previous studies have demonstrated the rigidity of the polymer chain to be extremely high so a semiflexible cylinder model was fit to determine the physical parameters of the rigid chains. The model can be found in Appendix A. The resulting contour length of 200 Å, extremely high Kuhn length (>1000 Å), and radius of 9 Å agree closely with the chain parameters calculated by density functional theory (DFT) and

molecular dynamics (MD) simulations in previous studies[186]. Because of the high Kuhn length, all subsequent fits of the high-*Q* region were done using a randomly oriented cylinder model. In the

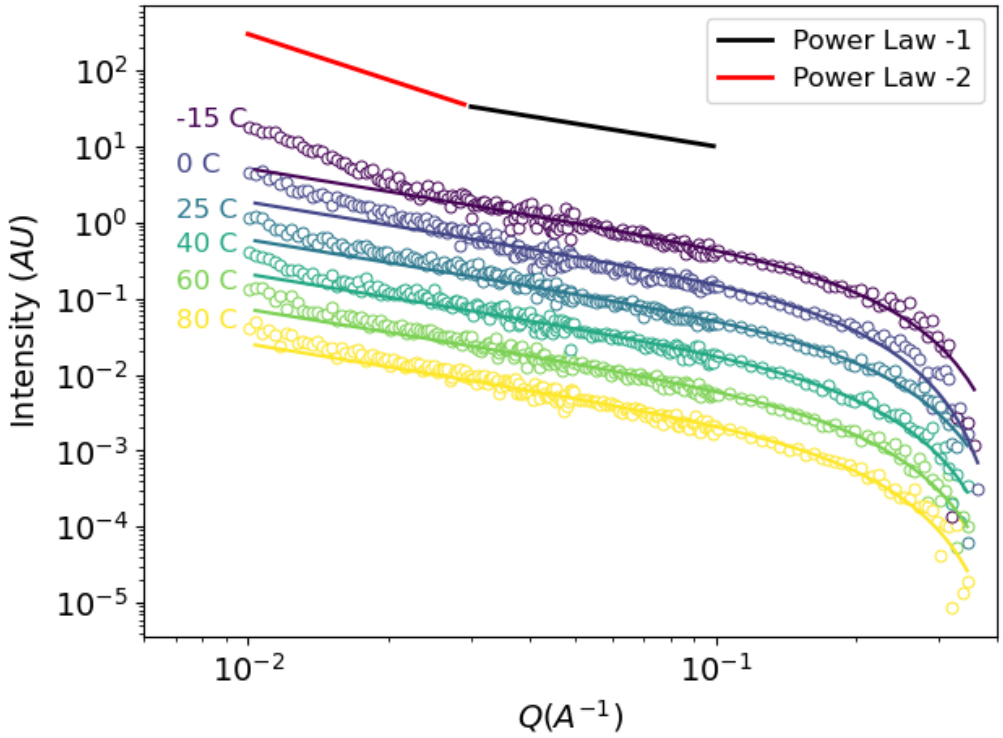

Figure 4-3: 1 weight percent PIDT-BT_{C16} in toluene at varying temperatures. Also shown are the semiflexible cylinder model fits for each profile. The profiles are adjusted along y-axis for clarity and do not reflect the absolute intensity.

low-*Q* region, there is an upturning feature that follows a Q^{-2} dependance. This feature becomes more prominent as the temperature decreases, indicating that aggregation is occurring. The -2 Q dependance is indicative of 2D structures like sheets. As discussed in Chapter 3.2, PIDT$_{C16}$-BT has been found to display side chain interactions akin to interdigitation and form aligned polymer backbones. Aggregates displaying sheet-like behavior can be interpreted as the result of aligned rods due to side chain interactions in solution. Hammouda *et al.* used a combined model to characterize cluster aggregates of polymer chains of PEO and is represented by:

$$I(Q) = \frac{A}{Q^N} + \frac{C}{1 + (QL)^M}$$

4-1

where the first term describes Porod scattering from clusters, and the second term is a Lorentzian function describing scattering from polymer chains. The study defined the clustering strength as A/Q^N where Q is a low value (0.004 $Å^{-1}$) to determine a more realistic measurement of the degree of aggregation. To characterize the aggregates, a combined model was fit that included a cylinder to capture the rigid rods at high-*Q* and a power law, which is of the same form as term 1 in equation

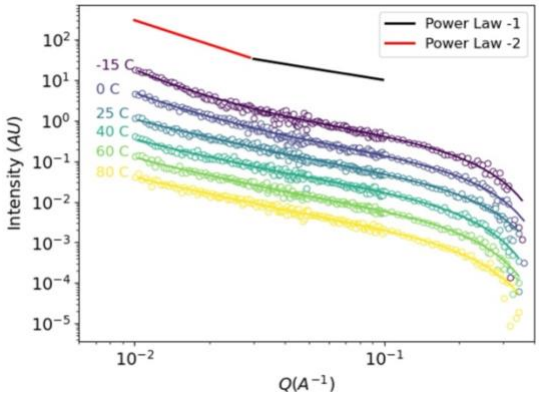

T (°C)	R_{rod} (Å)	Porod Exponent	Clustering Strength
80	8.51	2.12	0.20
60	8.40	2.46	0.28
40	8.45	2.48	0.26
25	7.83	2.28	0.24
0	7.88	2.72	0.59
-15	7.52	3.00	0.97

Figure 4-4: 1.0 weight percent $PIDT_{C16}$-BT in toluene with combined fits (left). Parameters of the combined model fits (right).

4-1 that would model the aggregates. The results of the fits including the fit parameters are shown in Figure 4-4. The porod exponent and the clustering strength increase with decreasing temperature and the onset of aggregation.

The SAXS profiles of 1 weight percent of $PIDT_{C16}$-BT in THF are shown in Figure 4-5. As expected, the poorer solvent leads to more induced aggregation in solution. This is evident by the more pronounced upturn of the profiles at low *Q* as well as the indication of aggregation even at high temperature. Like the profiles of $PIDT_{C16}$-BT in toluene, the scattering intensity at low *Q* follows a Q^{-2} dependance indicative of disk-like aggregates. The same model was fit for these profiles and the parameter fit results are also shown in Figure 4-5. Like the samples of polymer

dissolved in toluene, the decreasing temperature increases the porod exponent and the clustering strength of the aggregates.

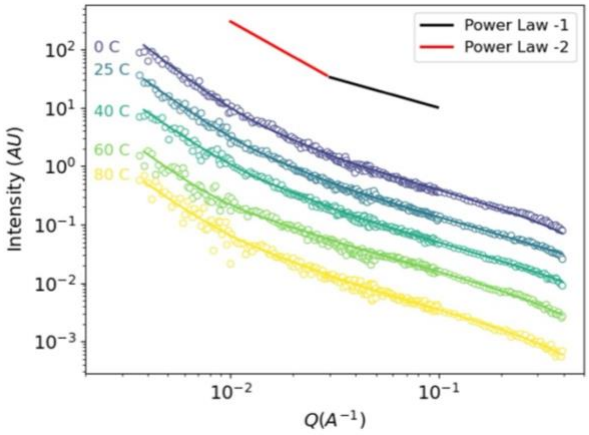

T (°C)	Porod Exponent	Clustering Strength
80	2.56	0.46
60	2.74	0.53
40	2.63	0.94
25	2.80	1.09
0	2.82	1.26

Figure 4-5: 1 weight percent PIDT$_{C16}$-BT in THF along with the combined cylinder and aggregate fits (left). Fit parameters (right). The profiles were adjusted along the y axis for clarity.

SAXS profiles were taken of 5 weight percent polymer dissolved in different solvents to explore the aggregated regime behavior. Figure 4-6 shows the SAXS profiles of solutions using toluene as the solvent. At the low-Q (0.004-0.01 A^{-1}), the profiles exhibit an aggregate structure with a dimension according with $Q^{-2.5}$, indicating formation of 2 dimensional, approaching 3 dimensional aggregates. In the middle-Q region (0.02-0.1 A^{-1}), the profiles continue to exhibit a power law according with Q^{-1} pertaining to the polymer chains. The combined model of cylinder and aggregate term was fit to this data to compare the degree of clustering. Figure 4-6 **Error! R eference source not found.**shows the parameters determined by model fitting of the temperature curves. Interestingly, the clustering strength and power law remain largely unchanged until the lowest temperature. The increase in fractal dimension of the low-Q aggregates indicates an increase in dimensionality from disk-like structures to more 3 dimensional loose clusters as would be expected form aggregates of this polymer.

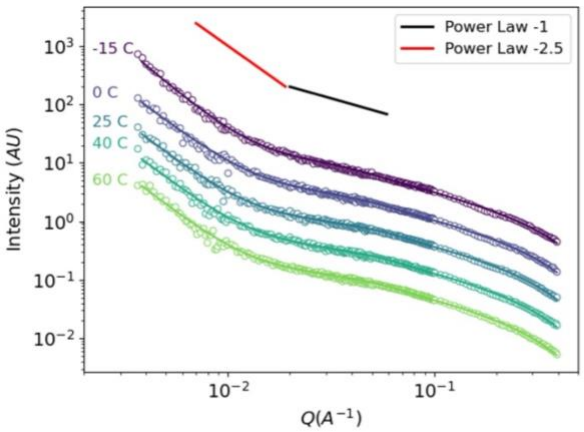

T (°C)	Porod Exponent	Clustering Strength
60	2.72	1.14
40	2.73	1.12
25	2.72	0.98
0	2.70	1.13
-15	3.00	1.76

Figure 4-6: 5 weight percent PIDT$_{C16}$-BT in toluene at varying temperatures along with the cylinder and aggregate fits (left). Parameters of the fits (right). The profiles were adjusted along the y-axis for clarity.

4.3.2 Solvent Effects

The Hansen solubility parameters (HSP) have been used as a tool for understanding solvent-polymer interactions[187,188]. Studies have shown that solvent aggregation is impacted not only by the relative interaction parameter between a solvent and solute, but also by specific parameters that may not be considered such as polarity and aromaticity. HSP, although not a complete or ideal picture of solubility, breaks down solvent-solute interaction into 3 parameters that aid in better understanding solvent-solute interactions. Through the parameters of dispersity, polarity and hydrogen bonding, solvent-polymer interactions can be investigated with increased detail when compared to simply comparing a χ interaction parameter as has been traditionally done. The parameters for each component of a system are experimentally or computationally determined and used to compare similarities and differences. To predict the solubility of a polymer in a solvent, or the miscibility between two solvents, their distance in HSP space is calculated. The smaller the distance, the better the interaction and better solubility between solvent and polymer. This distance is given by:

$$R_a^2 = 4(\delta D_1 - \delta D_2)^2 + (\delta P_1 - \delta P_2)^2 + (\delta H_1 - \delta H_2)^2$$

Where R_a is the relative distance between component 1 and component 2, δD_1 is the parameter for dispersity for component 1, and the rest of the parameters follow suit. Inspired by the work of Jin et al, the HSP distance were determined not only between the solvents and the

Solvent	δDispersity	δPolarity	δH-Bonding	R_a Polymer	R_a Backbone	R_a Side Chain
Toluene	18.00	1.40	2.00	**4.34**	**11.60**	**4.79**
THF	16.80	5.70	8.00	**5.16**	**12.04**	**9.85**
Anisole	19.20	6.30	3.30	**2.30**	**8.45**	**9.60**
Hexane	14.90	0.00	0.00	**9.20**	**18.16**	**2.00**

Table 4-1: calculated HSP distances between the polymer, side chain and backbone, respectively and each of the solvents.

polymer but also the solvents and the polymer backbone and side chains separately. Table 4-2 shows the calculated distances between each solvent and PIDTBT$_{C16}$-BT, PIDT$_{C16}$-BT backbone alone and PIDT$_{C16}$-BT sidechains alone. The HSP parameters for the solvents were obtained for the Hansen solubility handbook[188], the parameters for the polymer were obtained from literature[66] and the parameters for the side chains and backbone also from literature[189]. Because of the importance of the side chains in morphology and solubility of IDT-based polymers, attention should be given to the distance between solvents and PIDT$_{C16}$-BT side chains. According to the calculated distances, toluene is predicted to be a good solvent and THF a marginal solvent.

When comparing the aggregation behavior of PIDT$_{C16}$-BT in the two solvents in the dilute regime, although THF shows earlier onset of aggregation, the structures that formed in toluene are of higher fractional dimension and cluster strength. To examine the impact of this diverging aggregation behavior on the final morphology, SAXS profiles were taken at the solubility limit for each solvent. The concentration of polymer in each solvent was increased and the SAXS scattering intensity taken for each concentration until the pattern did not increase in intensity, indicating that there could be no more polymer dissolved or suspended in solution. The scattering curve for

toluene and THF at the solubility limit is shown in Figure 4-7 along with the parameter fits. The clustering strength and porod exponent are significantly larger for the clusters formed from toluene

Solvent	Porod Exponent	Clustering Strength
THF	3.05	4.73
Toluene	3.58	10.34

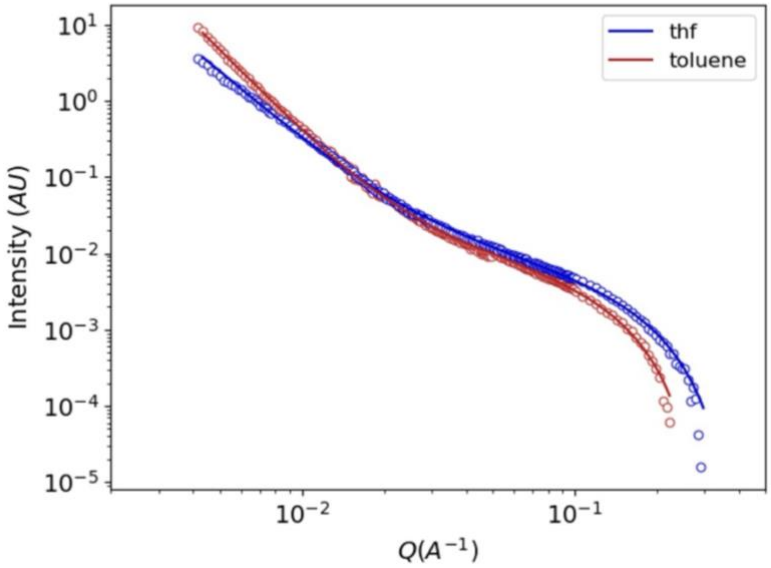

Figure 4-7: SAXS scattering profiles for PIDT$_{C16}$-BT in toluene and THF at their solubility limit. The table shows the parameter fits for the fitted models.

than THF. Together with the earlier onset of THF aggregation indicates that the poorer solvent leads to less dense and more weakly clustered aggregated domains that precipitate into the solid state. Toluene, on the other hand, maintains polymer chains in solution to form larger, more strongly aggregated clusters.

4.3.3 Impact on Charge Mobility

To determine the impact of solvent on network effects of aggregation, organic field effect transistors (OFETs) were fabricated using an active layer made from spin-coated 1 weight % solution of PIT_{C16}-BT dissolved in each solvent. Figure 4-8 shows the combined results from the extracted hole mobility. As can be seen in the overlap of the uncertainties, the difference in aggregation behavior displayed in each of the different solvents does not translate to improved or decreased field effect mobility. Improved certainties and perhaps a higher degree of impact on the

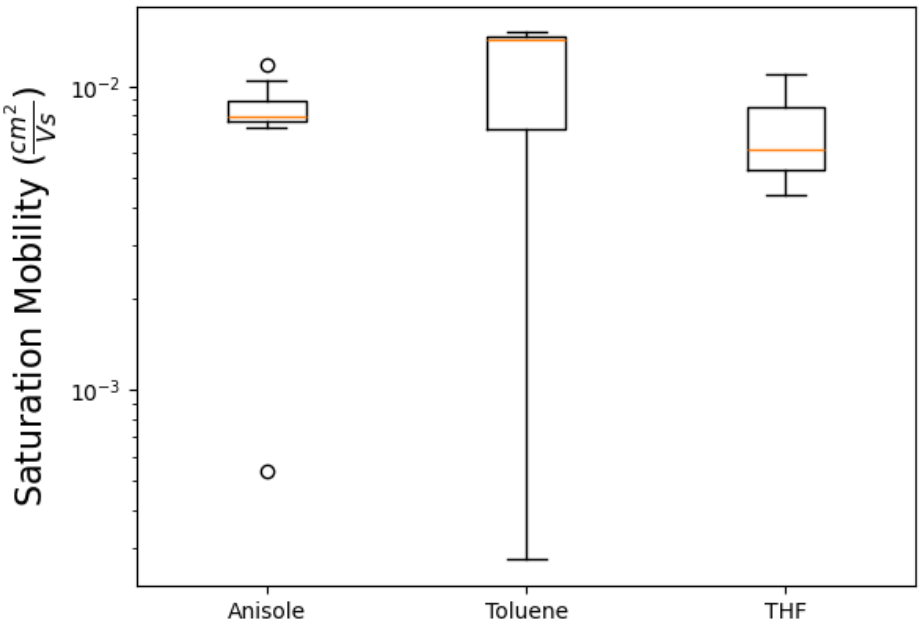

Figure 4-8: OFET saturation mobilities from devices fabricated using each solvent to deposit the active layer.

charge mobilities may be obtained by using higher molecular weight polymers. This will increase the saturation mobility in general, leading to more certain figures. Higher molecular weight IDT-based polymers have also been shown to be more affected by the solvent used[189].

4.4 Conclusions

IDTBT's aggregation behavior is threefold: First, isolated rod-like chains exist in solution in the dilute regime. As the concentration increases or temperature decreases, the chains planarize

and begin to show signs of pre-aggregation. In the semi dilute regime, the chains remain isolated from each other in solvents that display good interactions with the polymer sidechains. In poor

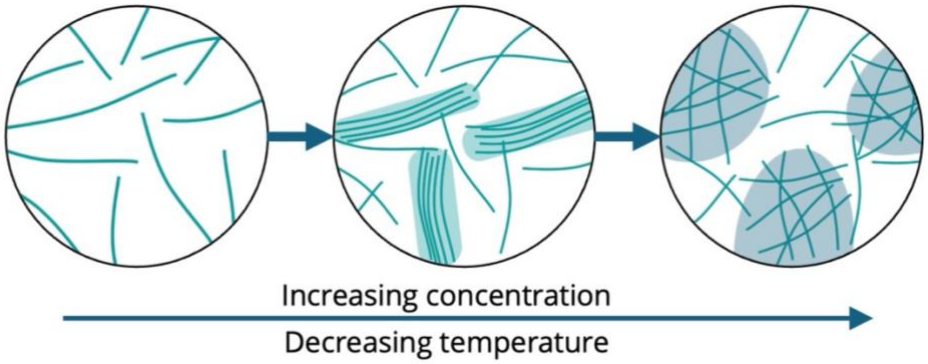

Figure 4-9: Drawing showing the aggregation behavior of $PIDT_{C16}$-BT in marginal and theta solvents. The polymer begins as isolated rods which form 2-dimensional aggregates which densify into 3-dimensional clusters.

solvents, aggregation has already begun to occur in the form of small disk like aggregates forming when chains align locally due to side chain interactions. In the aggregate regime, the chains form network-like aggregates with occasional overlap points where sidechain interdigitation and π-stacking are likely present. Last, the polymer aggregates into amorphous regions dense with polymer. The choice of polymer solvent affects the point at which aggregation occurs as well as the degree of formation of the aggregate clusters prior to solid state and therefore will affect final device performance. However, the low molecular weight of our example polymer led to low mobilities which affected the results.

Chapter 5. Conclusions and Outlook

The work described in Chapters 3 and 4 uncovered the specific roles that molecular structure and processing conditions of CP play in determining their physical properties. IDT-based polymer systems are very sensitive to side chain attachment density. Increased side chain density obtained by attaching a side chain to each monomer unit disrupts the phenomena of side chain interdigitation. This simple relationship can be used to tune the elasticity of the material, but at the cost of charge mobility, which is instrumental to the usability of CP in commercial applications. Decreasing side chain density by modifying the backbone extension is another tool developed that showed how interdigitation can be controlled by very simply synthetic modifications. The results of maintaining interdigitation while also maintaining increased side chain attachment density (keeping at least one side chain per monomer unit), still displayed decreased charge mobility. This result is surprising and leads to the conclusion that there is another interchain interaction which serves as the driver behind charge transfer between chains, a requirement for long-range conductivity. Future work should aim to elucidate further understanding of the mechanisms by which these extremely rigid polymers experience interchain charge transfer.

A proposed strategy that adopts a synthetic approach is to modify the backbone side chain density attachment to disrupt interdigitation while leaving gaps along the backbone to facilitate interchain crossing and π-stacking. This can be achieved by modifying the IDT core to include a higher side chain density attachment or include bulkier side chain groups that hinder interdigitation. Another strategy is to control the polymerization of IDT-based polymers to precisely place monomers with shorter side chains at discrete distances along the backbone. These strategies add synthetic complexity involving extending the IDT core monomer and changing the

synthetic route of polymerization altogether as controlled polymerizations necessitate a chain growth mechanism as opposed to the popularly used polycondensation.

One of the challenges of accurately characterizing the pi-stacking interactions through which chains transfer charges is that their infrequency and extremely local order make them difficult to identify. In this work, multiple GIWAXS profiles are presented in which the pi-stacking peaks are largely obfuscated by scattering from other interactions stemming from the side chains. Another strategy proposed is to use scattering techniques to further understand this elusive interchain interaction. Chapter 3.1 used deuteration of the matrix polymer to generate contrast and visualize only the polymer chains of the CP of interest. Multiple studies, including one in which I was a coauthor, have been able to selectively deuterate the side chains of CP to visualize only the backbone conformation and interactions. The strategy proposed here is to selectively isolate the backbone of IDT-based polymers and perform a suite of scattering experiments including neutron diffraction to better characterize interchain interactions.

Lastly, the effort to modify the film morphology and charge transport performance using only processing techniques should be expanded to other IDT-based polymers. The materials developed in Chapter 3.3 share the same IDT core molecular structure with polymers that have been shown to self-assemble through thermal annealing. A proposed study is that of the impacts of thermal and solvent annealing on the charge mobility and morphology of PIDTT$_{C16}$-TPD$_{C8}$ as well as other extended core IDT-based polymers. Lyotropic liquid crystalline phases have been found in DA copolymers that share a similar structure to that of IDT-based polymers. Future work should explore side chain modifications that can lead to these states to improve film morphology and macroscale properties.

Appendix A: Small Angle Scattering Models

5.1 Guinier-Porod

The Guinier-Porod model is defined as:

$$I(Q) = \begin{cases} \frac{G}{Q^s} \exp\left[-\frac{Q^2 R_g^2}{3-s}\right] & Q \le Q_1 \\ \frac{D}{Q^m} & Q \le Q_1 \end{cases}$$

$$Q_1 = \frac{1}{Rg}\sqrt{\frac{(m-s)(3-s)}{2}}$$

$$D = \frac{G}{R_g^{m-s}} \exp\left[\frac{s-m}{2}\right]\left(\frac{(m-s)(3-s)}{2}\right)^{\frac{m-s}{2}}$$

0-1

where G is a scale factor, R_g is the radius of gyration, m is the Porod exponent, and s is a variable in the range $0 \le s \le 2$. This variable, s, is related to the dimensionality of the scattering objects which can range from 3D when $s = 0$ (e.g. sphere), 2D when $s = 1$ (e.g. rods), and 1D when $s = 2$ (e.g. lamellae, plates).

5.2 Spherical Form Factors

The form factor for a spherical domain is defined as:

$$I(Q) = \frac{scale}{V}\left[3V(\Delta\rho)\frac{\sin(Qr) - Qr\cos(Qr)}{(Qr)^3}\right]^2$$

0-2

where V is the sphere volume and r is the sphere radius. The radius of gyration of a sphere is defined as:

$$R_g^2 = \frac{3}{5} r^2$$

0-3

The form factor for randomly oriented ellipsoids is defined as:

$$I(Q) = \frac{scale}{V} \int_0^{\frac{\pi}{2}} F^2(Q, \alpha) \sin \alpha \, d\alpha$$

$$F(Q, \alpha) = \Delta\rho V \frac{3(\sin(Qr) - Qr\cos(Qr))}{(Qr)^3}$$

$$r = \sqrt{R_{equatorial}^2 \sin^2(\alpha) + R_{polar}^2 \cos^2(\alpha)}$$

0-4

where *V* is the ellipsoid volume, $R_{equatorial}$ and R_{polar} are the equatorial and polar radii of the ellipsoid, respectively. α is the angle between the axis of the ellipsoid and *Q*.

5.3 Cylinders

The form factor for a randomly oriented cylinder is defined as:

$$I(Q) = \frac{scale}{V} \int_0^{\frac{\pi}{2}} F^2(Q, \alpha) \sin(\alpha) \, d\alpha$$

$$F(q, \alpha) = 2\,(\Delta\rho)V \frac{\sin\left(\frac{1}{2} QL\, cos(\alpha)\right)}{\frac{1}{2} QL\cos(\alpha)} \frac{J_1(QR\sin(\alpha))}{QRsin(\alpha)}$$

$$V = \pi R^2 L$$

0-5

where $R_{cylinder}$, and $L_{cylinder}$ are the cylinder radius and length, respectively, and J_1 is the Bessel function of the first kind.

The form factor for a semiflexible cylinder, derived from a worm-like chain model with excluded volume effects is given by:

$$I(Q) = \frac{scale}{V}\Delta\rho^2 S(Q, L_c, b)P(Q, R)$$

0-6

Where *V* is the volume of the cylinders given in Equation 0-5. *S(Q,L_c,b)* is the scattering function of a single semi-flexible polymer chain with excluded volume effects given in Scott *et al.* as they derived it from previous literature[85,190]. *P(Q,R)* is the scattering function accounting for the finite cross-section of a rigid rod, and is given by:

$$P(Q, R) = \left[\frac{2J_1(QR)}{QR}\right]^2$$

0-7

Where *R* is the cylinder radius and J_1 is the first order Bessel function of the first kind.

Appendix B: Other Notable Works

Together with the Xiao group in UW chemistry, we were able to fabricate and test OFETS using metal-organic macrocycles, derived from the large, conjugated metal-organic frameworks. Using field effect transistors, we were able to uncover the ambipolar behavior of these 0D materials. The work is published in the following article:

Zasada, L. B.; **Guio, L**.; Kamin, A. A.; Dhakal, D.; Monahan, M.; Seidler, G. T.; Luscombe, C. K.; Xiao, D. J. Conjugated Metal–Organic Macrocycles: Synthesis, Characterization, and Electrical Conductivity. J. Am. Chem. Soc. 2022, 144 (10), 4515–4521. https://doi.org/10.1021/jacs.1c12596.

The work done in this publication was a combination of efforts by all the authors. Specifically, I was responsible for the fabricating and testing organic field effect transistors and collection of hole mobility data. The first author, Leo Zasada, synthesized the materials used in this paper and performed the overall analysis. We also discussed ideas and conclusions from the data collaboratively prior to the writing of this paper.

Appendix C: References

(1) Allison, L. K.; Andrew, T. L. A Wearable All-Fabric Thermoelectric Generator. *Adv. Mater. Technol.* **2019**, *4* (5), 1800615. https://doi.org/10.1002/admt.201800615.

(2) Jiang, H.; Khang, D.-Y.; Song, J.; Sun, Y.; Huang, Y.; Rogers, J. A. Finite Deformation Mechanics in Buckled Thin Films on Compliant Supports. *Proc. Natl. Acad. Sci.* **2007**, *104* (40), 15607–15612. https://doi.org/10.1073/pnas.0702927104.

(3) Lang, R.; Schön, J.; Dimroth, F.; Lackner, D. Optimization of GaAs Solar Cell Performance and Growth Efficiency at MOVPE Growth Rates of 100 Mm/h. *IEEE J. Photovolt.* **2018**, *8* (6), 1596–1600. https://doi.org/10.1109/JPHOTOV.2018.2868021.

(4) Woodhouse, M.; Goodrich, A. *Manufacturing Cost Analysis Relevant to Single-and Dual-Junction Photovoltaic Cells Fabricated with III-Vs and III-Vs Grown on Czochralski Silicon (Presentation)*; NREL/PR-6A20-60126; National Renewable Energy Lab. (NREL), Golden, CO (United States), 2014. https://www.osti.gov/biblio/1132117 (accessed 2024-05-01).

(5) Shirakawa, H. Nobel Lecture: The Discovery of Polyacetylene Film---the Dawning of an Era of Conducting Polymers. *Rev. Mod. Phys.* **2001**, *73* (3), 713–718. https://doi.org/10.1103/RevModPhys.73.713.

(6) Chiang, C. K.; Fincher, C. R.; Park, Y. W.; Heeger, A. J.; Shirakawa, H.; Louis, E. J.; Gau, S. C.; MacDiarmid, A. G. Electrical Conductivity in Doped Polyacetylene. *Phys. Rev. Lett.* **1977**, *39* (17), 1098–1101. https://doi.org/10.1103/PhysRevLett.39.1098.

(7) MacDiarmid, A. G. "Synthetic Metals": A Novel Role for Organic Polymers. *Curr. Appl. Phys.* **2001**, *1* (4), 269–279. https://doi.org/10.1016/S1567-1739(01)00051-7.

(8) Andersen, T. R.; Dam, H. F.; Hösel, M.; Helgesen, M.; Carlé, J. E.; Larsen-Olsen, T. T.; Gevorgyan, S. A.; Andreasen, J. W.; Adams, J.; Li, N.; Machui, F.; Spyropoulos, G. D.; Ameri, T.; Lemaître, N.; Legros, M.; Scheel, A.; Gaiser, D.; Kreul, K.; Berny, S.; Lozman, O. R.; Nordman, S.; Välimäki, M.; Vilkman, M.; Søndergaard, R. R.; Jørgensen, M.; Brabec, C. J.; Krebs, F. C. Scalable, Ambient Atmosphere Roll-to-Roll Manufacture of Encapsulated Large Area, Flexible Organic Tandem Solar Cell Modules. *Energy Environ. Sci.* **2014**, *7* (9), 2925–2933. https://doi.org/10.1039/C4EE01223B.

(9) *Ribes Tech – official website*. https://www.ribestech.it/ (accessed 2024-05-07).

(10) Habas, S. E.; Platt, H. A. S.; van Hest, M. F. A. M.; Ginley, D. S. Low-Cost Inorganic Solar Cells: From Ink To Printed Device. *Chem. Rev.* **2010**, *110* (11), 6571–6594. https://doi.org/10.1021/cr100191d.

(11) Benight, S. J.; Wang, C.; Tok, J. B. H.; Bao, Z. Stretchable and Self-Healing Polymers and Devices for Electronic Skin. *Prog. Polym. Sci.* **2013**, *38* (12), 1961–1977. https://doi.org/10.1016/j.progpolymsci.2013.08.001.

(12) Khalili, N.; Naguib, H. E.; Kwon, R. H. Development, Fabrication, and Modeling of Highly Sensitive Conjugated Polymer Based Piezoresistive Sensors in Electronic Skin Applications. In *Behavior and Mechanics of Multifunctional Materials and Composites 2016*; SPIE, 2016; Vol. 9800, pp 152–159. https://doi.org/10.1117/12.2222086.

(13) Cronemeyer, D. C. Hall and Drift Mobility in High-Resistivity Single-Crystal Silicon. *Phys. Rev.* **1957**, *105* (2), 522–523. https://doi.org/10.1103/PhysRev.105.522.

(14) Paterson, A. F.; Singh, S.; Fallon, K. J.; Hodsden, T.; Han, Y.; Schroeder, B. C.; Bronstein, H.; Heeney, M.; McCulloch, I.; Anthopoulos, T. D. Recent Progress in High-Mobility

Organic Transistors: A Reality Check. *Adv. Mater.* **2018**, *30* (36), 1801079. https://doi.org/10.1002/adma.201801079.
(15) *Best Research-Cell Efficiency Chart*. https://www.nrel.gov/pv/cell-efficiency.html (accessed 2024-05-02).
(16) Green, M. A.; Dunlop, E. D.; Yoshita, M.; Kopidakis, N.; Bothe, K.; Siefer, G.; Hao, X. Solar Cell Efficiency Tables (Version 63). *Prog. Photovolt. Res. Appl.* **2024**, *32* (1), 3–13. https://doi.org/10.1002/pip.3750.
(17) Hu, P.; He, X.; Jiang, H. Greater than 10 Cm2 V−1 S−1: A Breakthrough of Organic Semiconductors for Field-Effect Transistors. *InfoMat* **2021**, *3* (6), 613–630. https://doi.org/10.1002/inf2.12188.
(18) Rhaman, M. M.; Matin, M. A. Organic Solar Cells: Historical Developments and Challenges. In *2015 International Conference on Advances in Electrical Engineering (ICAEE)*; 2015; pp 26–29. https://doi.org/10.1109/ICAEE.2015.7506788.
(19) Sirringhaus, H. 25th Anniversary Article: Organic Field-Effect Transistors: The Path Beyond Amorphous Silicon. *Adv. Mater.* **2014**, *26* (9), 1319–1335. https://doi.org/10.1002/adma.201304346.
(20) Salleo, A.; Kline, R. J.; DeLongchamp, D. M.; Chabinyc, M. L. Microstructural Characterization and Charge Transport in Thin Films of Conjugated Polymers. *Adv. Mater.* **2010**, *22* (34), 3812–3838. https://doi.org/10.1002/adma.200903712.
(21) Zuo, G.; Liu, X.; Fahlman, M.; Kemerink, M. Morphology Determines Conductivity and Seebeck Coefficient in Conjugated Polymer Blends. *ACS Appl. Mater. Interfaces* **2018**, *10* (11), 9638–9644. https://doi.org/10.1021/acsami.8b00122.
(22) Babel, A.; Jenekhe, S. A. Morphology and Field-Effect Mobility of Charge Carriers in Binary Blends of Poly(3-Hexylthiophene) with Poly[2-Methoxy-5-(2-Ethylhexoxy)-1,4-Phenylenevinylene] and Polystyrene. *Macromolecules* **2004**, *37* (26), 9835–9840. https://doi.org/10.1021/ma0482314.
(23) Root, S. E.; Savagatrup, S.; Printz, A. D.; Rodriquez, D.; Lipomi, D. J. Mechanical Properties of Organic Semiconductors for Stretchable, Highly Flexible, and Mechanically Robust Electronics. *Chem. Rev.* **2017**, *117* (9), 6467–6499. https://doi.org/10.1021/acs.chemrev.7b00003.
(24) Savagatrup, S.; Makaram, A. S.; Burke, D. J.; Lipomi, D. J. Mechanical Properties of Conjugated Polymers and Polymer-Fullerene Composites as a Function of Molecular Structure. *Adv. Funct. Mater.* **2014**, *24* (8), 1169–1181. https://doi.org/10.1002/adfm.201302646.
(25) Seitz, J. T. The estimation of mechanical properties of polymers from molecular structure. *J. Appl. Polym. Sci.* **1993**, *49* (8), 1331–1351. https://doi.org/10.1002/app.1993.070490802.
(26) Nunes, R. W.; Martin, J. R.; Johnson, J. F. Influence of Molecular Weight and Molecular Weight Distribution on Mechanical Properties of Polymers. *Polym. Eng. Sci.* **1982**, *22* (4), 205–228. https://doi.org/10.1002/pen.760220402.
(27) Billmeyer, F. W. *Textbook of Polymer Science*, 3rd ed.; Wiley: New York, 1984.
(28) Rodriguez, F.; Cohen, F.; Ober, C. K.; Archer, L. *Principles of Polymer Systems*, 5th ed.; CRC Press: Boca Raton, 2003. https://doi.org/10.1201/b12837.
(29) Fratini, S.; Nikolka, M.; Salleo, A.; Schweicher, G.; Sirringhaus, H. Charge Transport in High-Mobility Conjugated Polymers and Molecular Semiconductors. *Nat. Mater.* **2020**, *19* (5), 491–502. https://doi.org/10.1038/s41563-020-0647-2.

(30) Noriega, R.; Rivnay, J.; Vandewal, K.; Koch, F. P. V.; Stingelin, N.; Smith, P.; Toney, M. F.; Salleo, A. A General Relationship between Disorder, Aggregation and Charge Transport in Conjugated Polymers. *Nat. Mater.* **2013**, *12* (11), 1038–1044. https://doi.org/10.1038/nmat3722.

(31) Mollinger, S. A.; Krajina, B. A.; Noriega, R.; Salleo, A.; Spakowitz, A. J. Percolation, Tie-Molecules, and the Microstructural Determinants of Charge Transport in Semicrystalline Conjugated Polymers. *ACS Macro Lett.* **2015**, *4* (7), 708–712. https://doi.org/10.1021/acsmacrolett.5b00314.

(32) Mazzio, K. A.; Rice, A. H.; Durban, M. M.; Luscombe, C. K. Effect of Regioregularity on Charge Transport and Structural and Excitonic Coherence in Poly(3-Hexylthiophene) Nanowires. *J. Phys. Chem. C* **2015**, *119* (27), 14911–14918. https://doi.org/10.1021/acs.jpcc.5b02914.

(33) Ueji, K.; Ohno, M.; Takeya, J.; Watanabe, S. Correlation between Coherent Charge Transport and Crystallinity in Doped π -Conjugated Polymers. *Appl. Phys. Express* **2019**, *12* (1), 011004. https://doi.org/10.7567/1882-0786/aaf2cf.

(34) Lan, Y.-K.; Huang, C.-I. Charge Mobility and Transport Behavior in the Ordered and Disordered States of the Regioregular Poly(3-Hexylthiophene). *J. Phys. Chem. B* **2009**, *113* (44), 14555–14564. https://doi.org/10.1021/jp904841j.

(35) Nikolka, M.; Broch, K.; Armitage, J.; Hanifi, D.; Nowack, P. J.; Venkateshvaran, D.; Sadhanala, A.; Saska, J.; Mascal, M.; Jung, S.-H.; Lee, J.; McCulloch, I.; Salleo, A.; Sirringhaus, H. High-Mobility, Trap-Free Charge Transport in Conjugated Polymer Diodes. *Nat. Commun.* **2019**, *10* (1), 2122. https://doi.org/10.1038/s41467-019-10188-y.

(36) Cao, X.; Zhao, K.; Chen, L.; Liu, J.; Han, Y. Conjugated Polymer Single Crystals and Nanowires. *Polym. Cryst.* **2019**, *2* (3), e10064. https://doi.org/10.1002/pcr2.10064.

(37) Chang, M.; Su, Z.; Egap, E. Alignment and Charge Transport of One-Dimensional Conjugated Polymer Nanowires in Insulating Polymer Blends. *Macromolecules* **2016**, *49* (24), 9449–9456. https://doi.org/10.1021/acs.macromol.6b01721.

(38) Sommerville, P. J. W.; Li, Y.; Dong, B. X.; Zhang, Y.; Onorato, J. W.; Tatum, W. K.; Balzer, A. H.; Stingelin, N.; Patel, S. N.; Nealey, P. F.; Luscombe, C. K. Elucidating the Influence of Side-Chain Circular Distribution on the Crack Onset Strain and Hole Mobility of Near-Amorphous Indacenodithiophene Copolymers. *Macromolecules* **2020**, *53* (17), 7511–7518. https://doi.org/10.1021/acs.macromol.0c00512.

(39) Wang, W.; Tang, W.; Zhao, J.; Bao, B.; Xing, H.; Guo, X.; Wang, S.; Liu, Y. Probing the Intrinsic Charge Transport in Indacenodithiophene-Co-Benzothiadiazole Thin Films. *AIP Adv.* **2017**, *7* (12), 125314. https://doi.org/10.1063/1.5001986.

(40) Zhang, X.; Bronstein, H.; Kronemeijer, A. J.; Smith, J.; Kim, Y.; Kline, R. J.; Richter, L. J.; Anthopoulos, T. D.; Sirringhaus, H.; Song, K.; Heeney, M.; Zhang, W.; McCulloch, I.; DeLongchamp, D. M. Molecular Origin of High Field-Effect Mobility in an Indacenodithiophene–Benzothiadiazole Copolymer. *Nat. Commun.* **2013**, *4* (1), 2238. https://doi.org/10.1038/ncomms3238.

(41) Babel, A.; Jenekhe, S. A. Morphology and Field-Effect Mobility of Charge Carriers in Binary Blends of Poly(3-Hexylthiophene) with Poly[2-Methoxy-5-(2-Ethylhexoxy)-1,4-Phenylenevinylene] and Polystyrene. *Macromolecules* **2004**, *37* (26), 9835–9840. https://doi.org/10.1021/ma0482314.

(42) Liu, J.; Arif, M.; Zou, J.; Khondaker, S. I.; Zhai, L. Controlling Poly(3-Hexylthiophene) Crystal Dimension: Nanowhiskers and Nanoribbons. *Macromolecules* **2009**, *42* (24), 9390–9393. https://doi.org/10.1021/ma901955c.

(43) Tatum, W. K.; Luscombe, C. K. π -Conjugated Polymer Nanowires: Advances and Perspectives toward Effective Commercial Implementation. *Polym. J.* **2018**, *50* (8), 659–669. https://doi.org/10.1038/s41428-018-0062-6.

(44) Nawrocki, R. A.; Pavlica, E.; Ćelić, N.; Orlov, D.; Valant, M.; Mihailović, D.; Bratina, G. Fabrication of Poly(3-Hexylthiophene) Nanowires for High-Mobility Transistors. *Org. Electron.* **2016**, *30*, 92–98. https://doi.org/10.1016/j.orgel.2015.11.038.

(45) Park, Y. D.; Kim, D. H.; Jang, Y.; Cho, J. H.; Hwang, M.; Lee, H. S.; Lim, J. A.; Cho, K. Effect of Side Chain Length on Molecular Ordering and Field-Effect Mobility in Poly(3-Alkylthiophene) Transistors. *Org. Electron.* **2006**, *7* (6), 514–520. https://doi.org/10.1016/j.orgel.2006.07.007.

(46) Malik, S.; Nandi, A. K. Crystallization Mechanism of Regioregular Poly(3-Alkyl Thiophene)s. *J. Polym. Sci. Part B Polym. Phys.* **2002**, *40* (18), 2073–2085. https://doi.org/10.1002/polb.10272.

(47) Trznadel, M.; Pron, A.; Zagorska, M.; Chrzaszcz, R.; Pielichowski, J. Effect of Molecular Weight on Spectroscopic and Spectroelectrochemical Properties of Regioregular Poly(3-Hexylthiophene). *Macromolecules* **1998**, *31* (15), 5051–5058. https://doi.org/10.1021/ma970627a.

(48) Koch, F. P. V.; Rivnay, J.; Foster, S.; Müller, C.; Downing, J. M.; Buchaca-Domingo, E.; Westacott, P.; Yu, L.; Yuan, M.; Baklar, M.; Fei, Z.; Luscombe, C.; McLachlan, M. A.; Heeney, M.; Rumbles, G.; Silva, C.; Salleo, A.; Nelson, J.; Smith, P.; Stingelin, N. The Impact of Molecular Weight on Microstructure and Charge Transport in Semicrystalline Polymer Semiconductors–Poly(3-Hexylthiophene), a Model Study. *Prog. Polym. Sci.* **2013**, *38* (12), 1978–1989. https://doi.org/10.1016/j.progpolymsci.2013.07.009.

(49) Samitsu, S.; Shimomura, T.; Heike, S.; Hashizume, T.; Ito, K. Effective Production of Poly(3-Alkylthiophene) Nanofibers by Means of Whisker Method Using Anisole Solvent: Structural, Optical, and Electrical Properties. *Macromolecules* **2008**, *41* (21), 8000–8010. https://doi.org/10.1021/ma801128v.

(50) Chang, M.; Lee, J.; Kleinhenz, N.; Fu, B.; Reichmanis, E. Photoinduced Anisotropic Supramolecular Assembly and Enhanced Charge Transport of Poly(3-Hexylthiophene) Thin Films. *Adv. Funct. Mater.* **2014**, *24* (28), 4457–4465. https://doi.org/10.1002/adfm.201400523.

(51) An, L.; Duan, Y.; Yuan, Y.; Zhou, L.; Zhang, J. Effect of Thermal Annealing on the Microstructure of P3HT Thin Film Investigated by RAIR Spectroscopy. *Vib. Spectrosc.* **2013**, *68*, 40–44. https://doi.org/10.1016/j.vibspec.2013.05.002.

(52) Rafique, S.; Abdullah, S. M.; Sulaiman, K.; Iwamoto, M. Fundamentals of Bulk Heterojunction Organic Solar Cells: An Overview of Stability/Degradation Issues and Strategies for Improvement. *Renew. Sustain. Energy Rev.* **2018**, *84*, 43–53. https://doi.org/10.1016/j.rser.2017.12.008.

(53) Tong, Y.; Xiao, Z.; Du, X.; Zuo, C.; Li, Y.; Lv, M.; Yuan, Y.; Yi, C.; Hao, F.; Hua, Y.; Lei, T.; Lin, Q.; Sun, K.; Zhao, D.; Duan, C.; Shao, X.; Li, W.; Yip, H.-L.; Xiao, Z.; Zhang, B.; Bian, Q.; Cheng, Y.; Liu, S.; Cheng, M.; Jin, Z.; Yang, S.; Ding, L. Progress of the Key Materials for Organic Solar Cells. *Sci. China Chem.* **2020**, *63* (6), 758–765. https://doi.org/10.1007/s11426-020-9726-0.

(54) Chen, D.; Nakahara, A.; Wei, D.; Nordlund, D.; Russell, T. P. P3HT/PCBM Bulk Heterojunction Organic Photovoltaics: Correlating Efficiency and Morphology. *Nano Lett.* **2011**, *11* (2), 561–567. https://doi.org/10.1021/nl103482n.

(55) Holliday, S.; Li, Y.; Luscombe, C. K. Recent Advances in High Performance Donor-Acceptor Polymers for Organic Photovoltaics. *Prog. Polym. Sci.* **2017**, *70*, 34–51. https://doi.org/10.1016/j.progpolymsci.2017.03.003.

(56) Zhang, W.; Smith, J.; Watkins, S. E.; Gysel, R.; McGehee, M.; Salleo, A.; Kirkpatrick, J.; Ashraf, S.; Anthopoulos, T.; Heeney, M.; McCulloch, I. Indacenodithiophene Semiconducting Polymers for High-Performance, Air-Stable Transistors. *J. Am. Chem. Soc.* **2010**, *132* (33), 11437–11439. https://doi.org/10.1021/ja1049324.

(57) Venkateshvaran, D.; Nikolka, M.; Sadhanala, A.; Lemaur, V.; Zelazny, M.; Kepa, M.; Hurhangee, M.; Kronemeijer, A. J.; Pecunia, V.; Nasrallah, I.; Romanov, I.; Broch, K.; McCulloch, I.; Emin, D.; Olivier, Y.; Cornil, J.; Beljonne, D.; Sirringhaus, H. Approaching Disorder-Free Transport in High-Mobility Conjugated Polymers. *Nature* **2014**, *515* (7527), 384–388. https://doi.org/10.1038/nature13854.

(58) Wadsworth, A.; Chen, H.; Thorley, K. J.; Cendra, C.; Nikolka, M.; Bristow, H.; Moser, M.; Salleo, A.; Anthopoulos, T. D.; Sirringhaus, H.; McCulloch, I. Modification of Indacenodithiophene-Based Polymers and Its Impact on Charge Carrier Mobility in Organic Thin-Film Transistors. *J. Am. Chem. Soc.* **2020**, *142* (2), 652–664. https://doi.org/10.1021/jacs.9b09374.

(59) Ren, H.; Zhang, J.; Tong, Y.; Zhang, J.; Zhao, X.; Cui, N.; Li, Y.; Ye, X.; Tang, Q.; Liu, Y. Synchronously Improved Stretchability and Mobility by Tuning the Molecular Weight for Intrinsically Stretchable Transistors. *J. Mater. Chem. C* **2020**, *8* (44), 15646–15654. https://doi.org/10.1039/D0TC02363A.

(60) Bronstein, H.; Leem, D. S.; Hamilton, R.; Woebkenberg, P.; King, S.; Zhang, W.; Ashraf, R. S.; Heeney, M.; Anthopoulos, T. D.; Mello, J. de; McCulloch, I. Indacenodithiophene-Co-Benzothiadiazole Copolymers for High Performance Solar Cells or Transistors via Alkyl Chain Optimization. *Macromolecules* **2011**, *44* (17), 6649–6652. https://doi.org/10.1021/ma201158d.

(61) Li, Y.; Gu, M.; Pan, Z.; Zhang, B.; Yang, X.; Gu, J.; Chen, Y. Indacenodithiophene: A Promising Building Block for High Performance Polymer Solar Cells. *J. Mater. Chem. A* **2017**, *5* (22), 10798–10814. https://doi.org/10.1039/C7TA02562A.

(62) Li, Y.; Tatum, W. K.; Onorato, J. W.; Zhang, Y.; Luscombe, C. K. Low Elastic Modulus and High Charge Mobility of Low-Crystallinity Indacenodithiophene-Based Semiconducting Polymers for Potential Applications in Stretchable Electronics. *Macromolecules* **2018**, *51* (16), 6352–6358. https://doi.org/10.1021/acs.macromol.8b00898.

(63) Liang, C.; Wang, H. Indacenodithiophene-Based D-A Conjugated Polymers for Application in Polymer Solar Cells. *Org. Electron.* **2017**, *50*, 443–457. https://doi.org/10.1016/j.orgel.2017.06.059.

(64) Zhao, B.; Pei, D.; Jiang, Y.; Wang, Z.; An, C.; Deng, Y.; Ma, Z.; Han, Y.; Geng, Y. Simultaneous Enhancement of Stretchability, Strength, and Mobility in Ultrahigh-Molecular-Weight Poly(Indacenodithiophene-Co-Benzothiadiazole). *Macromolecules* **2021**, *54* (21), 9896–9905. https://doi.org/10.1021/acs.macromol.1c01513.

(65) Cendra, C.; Balhorn, L.; Zhang, W.; O'Hara, K.; Bruening, K.; Tassone, C. J.; Steinrück, H.-G.; Liang, M.; Toney, M. F.; McCulloch, I.; Chabinyc, M. L.; Salleo, A.; Takacs, C. J.

Unraveling the Unconventional Order of a High-Mobility Indacenodithiophene–Benzothiadiazole Copolymer. *ACS Macro Lett.* **2021**, *10* (10), 1306–1314. https://doi.org/10.1021/acsmacrolett.1c00547.

(66) Shin, E.-S.; Noh, Y.-Y. Effect of Pre-Aggregation in Solution State on the Performance of Organic Field-Effect Transistors with Indacenodithiophene-Co-Benzothiadiazole. *Org. Electron.* **2018**, *53*, 111–116. https://doi.org/10.1016/j.orgel.2017.11.032.

(67) Königlich Bayerische Akademie der Wissenschaften. Mathematisch-Physikalische Klasse. *Sitzungsberichte der Mathematisch-Physikalischen Classe der K.B. Akademie der Wissenschaften zu München*; München : Akademische Buchdruckere, 1871.

(68) Bragg, W. H.; Bragg, W. L. The Reflection of X-Rays by Crystals. *Proc. R. Soc. Lond. Ser. Contain. Pap. Math. Phys. Character* **1997**, *88* (605), 428–438. https://doi.org/10.1098/rspa.1913.0040.

(69) Howard, J. A. K. Dorothy Hodgkin and Her Contributions to Biochemistry. *Nat. Rev. Mol. Cell Biol.* **2003**, *4* (11), 891–896. https://doi.org/10.1038/nrm1243.

(70) Chadwick, J. The Existence of a Neutron. *Proc. R. Soc. Lond. Ser. Contain. Pap. Math. Phys. Character* **1997**, *136* (830), 692–708. https://doi.org/10.1098/rspa.1932.0112.

(71) Wollan, E. O.; Shull, C. G. The Diffraction of Neutrons by Crystalline Powders. *Phys. Rev.* **1948**, *73* (8), 830–841. https://doi.org/10.1103/PhysRev.73.830.

(72) *Shull and Wollan, neutron pioneers « ORNL and the Nobel Prize*. https://nobel.ornl.gov/laureate/the-detection-of-cosmic-neutrinos/ (accessed 2024-05-09).

(73) *Neutrons, X-Rays and Light: Scattering Methods Applied to Soft Condensed Matter*; Lindner, P., Zemb, Th., Eds.; Elsevier Science: Amsterdam, 2002.

(74) Hammouda, B. *Probing Nanoscale Structures - The SANS Toolbox.*; National Institute for Standards and Technology Center for Neutron Research: Gaithersburg, MD, 2016.

(75) *Polymers and Neutron Scattering*; Higgins, J. S., Benoit, H. C., Eds.; Oxford University Press Inc.: New York, 1994.

(76) Nedoma, A. J.; Robertson, M. L.; Wanakule, N. S.; Balsara, N. P. Measurements of the Composition and Molecular Weight Dependence of the Flory−Huggins Interaction Parameter. *Macromolecules* **2008**, *41* (15), 5773–5779. https://doi.org/10.1021/ma800698r.

(77) Russell, T. P.; Ito, H.; Wignall, G. D. Neutron and X-Ray Scattering Studies on Semicrystalline Polymer Blends. *Macromolecules* **1988**, *21* (6), 1703–1709. https://doi.org/10.1021/ma00184a029.

(78) *Neutrons, X-rays and Light: Scattering Methods Applied to Soft Condensed Matter - 1st Edition | Elsevier Shop*. https://shop.elsevier.com/books/neutrons-x-rays-and-light-scattering-methods-applied-to-soft-condensed-matter/lindner/978-0-444-51122-5 (accessed 2024-05-01).

(79) *Introduction to X-Ray Powder Diffractometry | Wiley*. Wiley.com. https://www.wiley.com/en-us/Introduction+to+X-Ray+Powder+Diffractometry-p-9780471513391 (accessed 2024-05-18).

(80) *Synchrotrons, the Swiss Army knives of science*. SLAC National Accelerator Laboratory. https://www6.slac.stanford.edu/research/slac-science-explained/synchrotrons (accessed 2024-05-18).

(81) Ishikawa, T.; Tamasaku, K.; Yabashi, M. High-Resolution X-Ray Monochromators. *Nucl. Instrum. Methods Phys. Res. Sect. Accel. Spectrometers Detect. Assoc. Equip.* **2005**, *547* (1), 42–49. https://doi.org/10.1016/j.nima.2005.05.010.

(82) Davies, R. J.; Zafeiropoulos, N. E.; Schneider, K.; Roth, S. V.; Burghammer, M.; Riekel, C.; Kotek, J. C.; Stamm, M. The Use of Synchrotron X-Ray Scattering Coupled with in Situ Mechanical Testing for Studying Deformation and Structural Change in Isotactic Polypropylene. *Colloid Polym. Sci.* **2004**, *282* (8), 854–866. https://doi.org/10.1007/s00396-004-1118-z.
(83) Kyrey, T.; Ganeva, M.; Witte, J.; Feoktystov, A.; Wellert, S.; Holderer, O. Grazing Incidence Small-Angle Neutron Scattering: Background Determination and Optimization for Soft Matter Samples. *Appl. Sci.* **2021**, *11* (7), 3085. https://doi.org/10.3390/app11073085.
(84) Steele, J. A.; Solano, E.; Hardy, D.; Dayton, D.; Ladd, D.; White, K.; Chen, P.; Hou, J.; Huang, H.; Saha, R. A.; Wang, L.; Gao, F.; Hofkens, J.; Roeffaers, M. B. J.; Chernyshov, D.; Toney, M. F. How to GIWAXS: Grazing Incidence Wide Angle X-Ray Scattering Applied to Metal Halide Perovskite Thin Films. *Adv. Energy Mater.* **2023**, *13* (27), 2300760. https://doi.org/10.1002/aenm.202300760.
(85) Pedersen, J. S.; Schurtenberger, P. Scattering Functions of Semiflexible Polymers with and without Excluded Volume Effects. *Macromolecules* **1996**, *29* (23), 7602–7612. https://doi.org/10.1021/ma9607630.
(86) Lightsource, S. S. R. *Stable Solvent for Solution-based Electrical Doping of Semiconducting Polymer Films and Its Application to Organic Solar Cells*. https://www-ssrl.slac.stanford.edu/content/science/highlight/2018-05-31/stable-solvent-solution-based-electrical-doping-semiconducting-polymer (accessed 2024-05-31).
(87) Hexemer, A.; Müller-Buschbaum, P. Advanced Grazing-Incidence Techniques for Modern Soft-Matter Materials Analysis. *IUCrJ* **2015**, *2* (1), 106–125. https://doi.org/10.1107/S2052252514024178.
(88) Akiba, I.; Sakurai, K. Characterizing Block-Copolymer Micelles Used in Nanomedicines via Solution Static Scattering Techniques. *Polym. J.* **2021**, *53* (9), 951–973. https://doi.org/10.1038/s41428-021-00489-9.
(89) Physics and Properties of Semiconductors—A Review. In *Physics of Semiconductor Devices*; John Wiley & Sons, Ltd, 2006; pp 5–75. https://doi.org/10.1002/9780470068328.ch1.
(90) Streetman, B. G.; Banerjee, S. *Solid State Electronic Devices*; Prentice Hall, 2000.
(91) Schott, S.; Gann, E.; Thomsen, L.; Jung, S.-H.; Lee, J.-K.; McNeill, C. R.; Sirringhaus, H. Charge-Transport Anisotropy in a Uniaxially Aligned Diketopyrrolopyrrole-Based Copolymer. *Adv. Mater.* **2015**, *27* (45), 7356–7364. https://doi.org/10.1002/adma.201502437.
(92) Jaeger, R. C. *Introduction to Microelectronic Fabrication*; Prentice Hall, 2002.
(93) Horowitz, G. Organic Field-Effect Transistors. *Adv. Mater.* **1998**, *10* (5), 365–377. https://doi.org/10.1002/(SICI)1521-4095(199803)10:5<365::AID-ADMA365>3.0.CO;2-U.
(94) *Silicon/Silicon Dioxide (Si/SiO2) Wet Thermal Oxide Silicon Wafer and Substrates, Prime Grade*. MSE Supplies LLC. https://www.msesupplies.com/products/silicon-silicon-dioxide-si-sio2-thermal-oxide-silicon-wafer-and-substrates-prime-grade (accessed 2024-05-22).
(95) Ulman, A. Formation and Structure of Self-Assembled Monolayers. *Chem. Rev.* **1996**, *96* (4), 1533–1554. https://doi.org/10.1021/cr9502357.

(96) Casalini, S.; Bortolotti, C. A.; Leonardi, F.; Biscarini, F. Self-Assembled Monolayers in Organic Electronics. *Chem. Soc. Rev.* **2017**, *46* (1), 40–71. https://doi.org/10.1039/C6CS00509H.
(97) Li, G.; Li, B.; Ren, B.; Li, Y.; Chen, H.; Chen, J. High-Thermal-Conductivity AlN Ceramics Prepared from Octyltrichlorosilane-Modified AlN Powder. *Processes* **2023**, *11* (4), 1186. https://doi.org/10.3390/pr11041186.
(98) Dong, J.; Wang, A.; Ng, K. Y. S.; Mao, G. Self-Assembly of Octadecyltrichlorosilane Monolayers on Silicon-Based Substrates by Chemical Vapor Deposition. *Thin Solid Films* **2006**, *515* (4), 2116–2122. https://doi.org/10.1016/j.tsf.2006.07.041.
(99) Ito, Y.; Virkar, A. A.; Mannsfeld, S.; Oh, J. H.; Toney, M.; Locklin, J.; Bao, Z. Crystalline Ultrasmooth Self-Assembled Monolayers of Alkylsilanes for Organic Field-Effect Transistors. *J. Am. Chem. Soc.* **2009**, *131* (26), 9396–9404. https://doi.org/10.1021/ja9029957.
(100) Perkampus, H.-H. *UV-VIS Spectroscopy and Its Applications*; Springer Science & Business Media, 2013.
(101) *UV-Vis Absorption Spectroscopy - Theory*. https://teaching.shu.ac.uk/hwb/chemistry/tutorials/molspec/uvvisab1.htm (accessed 2024-05-23).
(102) Casasanta, G.; Garra, R. Towards a Generalized Beer-Lambert Law. *Fractal Fract.* **2018**, *2* (1), 8. https://doi.org/10.3390/fractalfract2010008.
(103) Spano, F. C. Modeling Disorder in Polymer Aggregates: The Optical Spectroscopy of Regioregular Poly(3-Hexylthiophene) Thin Films. *J. Chem. Phys.* **2005**, *122* (23), 234701. https://doi.org/10.1063/1.1914768.
(104) Baghgar, M.; Labastide, J. A.; Bokel, F.; Hayward, R. C.; Barnes, M. D. Effect of Polymer Chain Folding on the Transition from H- to J-Aggregate Behavior in P3HT Nanofibers. *J. Phys. Chem. C* **2014**, *118* (4), 2229–2235. https://doi.org/10.1021/jp411668g.
(105) Spano, F. C. Absorption in Regio-Regular Poly(3-Hexyl)Thiophene Thin Films: Fermi Resonances, Interband Coupling and Disorder. *Chem. Phys.* **2006**, *325* (1), 22–35. https://doi.org/10.1016/j.chemphys.2005.08.019.
(106) Clark, J.; Chang, J.-F.; Spano, F. C.; Friend, R. H.; Silva, C. Determining Exciton Bandwidth and Film Microstructure in Polythiophene Films Using Linear Absorption Spectroscopy. *Appl. Phys. Lett.* **2009**, *94* (16), 163306. https://doi.org/10.1063/1.3110904.
(107) Hintz, H.; Egelhaaf, H.-J.; Lüer, L.; Hauch, J.; Peisert, H.; Chassé, T. Photodegradation of P3HT−A Systematic Study of Environmental Factors. *Chem. Mater.* **2011**, *23* (2), 145–154. https://doi.org/10.1021/cm102373k.
(108) Liu, Y.; Wu, L.; Lai, P. T.; Zuo, Q. Air-Stability Analysis and Improvement of Poly(3-Hexylthiophene) Field-Effect Transistors. *Semicond. Sci. Technol.* **2009**, *24* (9), 095013. https://doi.org/10.1088/0268-1242/24/9/095013.
(109) Kim, J.-S.; Kim, J.-H.; Lee, W.; Yu, H.; Kim, H. J.; Song, I.; Shin, M.; Oh, J. H.; Jeong, U.; Kim, T.-S.; Kim, B. J. Tuning Mechanical and Optoelectrical Properties of Poly(3-Hexylthiophene) through Systematic Regioregularity Control. *Macromolecules* **2015**, *48* (13), 4339–4346. https://doi.org/10.1021/acs.macromol.5b00524.
(110) Hou, S.; Yu, J.; Zhuang, X.; Li, D.; Liu, Y.; Gao, Z.; Sun, T.; Wang, F.; Yu, X. Phase Separation of P3HT/PMMA Blend Film for Forming Semiconducting and Dielectric Layers in Organic Thin-Film Transistors for High-Sensitivity NO_2 Detection. *ACS Appl. Mater. Interfaces* **2019**, *11* (47), 44521–44527. https://doi.org/10.1021/acsami.9b15651.

(111) Qiu, L.; Wang, X.; Lee, W. H.; Lim, J. A.; Kim, J. S.; Kwak, D.; Cho, K. Organic Thin-Film Transistors Based on Blends of Poly(3-Hexylthiophene) and Polystyrene with a Solubility-Induced Low Percolation Threshold. *Chem. Mater.* **2009**, *21* (19), 4380–4386. https://doi.org/10.1021/cm900628j.
(112) Han, S.; Yu, X.; Shi, W.; Zhuang, X.; Yu, J. Solvent-Dependent Electrical Properties Improvement of Organic Field-Effect Transistor Based on Disordered Conjugated Polymer/Insulator Blends. *Org. Electron.* **2015**, *27*, 160–166. https://doi.org/10.1016/j.orgel.2015.09.003.
(113) Bronstein, H. A.; Luscombe, C. K. Externally Initiated Regioregular P3HT with Controlled Molecular Weight and Narrow Polydispersity. *J. Am. Chem. Soc.* **2009**, *131* (36), 12894–12895. https://doi.org/10.1021/ja9054977.
(114) Kline, S. R. Reduction and Analysis of SANS and USANS Data Using IGOR Pro. *J. Appl. Crystallogr.* **2006**, *39* (6), 895–900. https://doi.org/10.1107/S0021889806035059.
(115) Doucet, M.; King, S.; Butler, P.; Kienzle, P.; Parker, P.; Krzywon, J.; Jackson, A.; Richter, T.; Gonzales, M.; Nielsen, T.; Ferraz, L. R. SasView (Version 5.0.1). 2020.
(116) Doucet, M.; King, S.; Butler, P.; Kienzle, P.; Parker, P.; Krzywon, J.; Jackson, A.; Richter, T.; Gonzales, M.; Nielsen, T.; Ferraz, L. R. Sasmodels (Version 1.0.1). 2020.
(117) Kienzle, P. A.; Krycka, J.; Patel, N.; Sahin, I. Bumps (Version 0.7.11). University of Maryland: College Park, MD 2011.
(118) *Polymers and Neutron Scattering*; Higgins, J. S., Benoit, H. C., Eds.; Oxford University Press Inc.: New York, 1994.
(119) Endo, H. Study on Multicomponent Systems by Means of Contrast Variation SANS. *Phys. B Condens. Matter* **2006**, *385–386*, 682–684. https://doi.org/10.1016/j.physb.2006.05.290.
(120) Hammouda, B. A New Guinier–Porod Model. *J. Appl. Crystallogr.* **2010**, *43* (4), 716–719. https://doi.org/10.1107/S0021889810015773.
(121) Hammouda, B. Analysis of the Beaucage Model. *J. Appl. Crystallogr.* **2010**, *43* (6), 1474–1478. https://doi.org/10.1107/S0021889810033856.
(122) Ilavsky, J.; Zhang, F.; Allen, A. J.; Levine, L. E.; Jemian, P. R.; Long, G. G. Ultra-Small-Angle X-Ray Scattering Instrument at the Advanced Photon Source: History, Recent Development, and Current Status. *Metall. Mater. Trans. A* **2013**, *44* (1), 68–76. https://doi.org/10.1007/s11661-012-1431-y.
(123) Ilavsky, J.; Jemian, P. R.; Allen, A. J.; Zhang, F.; Levine, L. E.; Long, G. G. Ultra-Small-Angle X-Ray Scattering at the Advanced Photon Source. *J. Appl. Crystallogr.* **2009**, *42* (3), 469–479. https://doi.org/10.1107/S0021889809008802.
(124) Ilavsky, J.; Zhang, F.; Andrews, R. N.; Kuzmenko, I.; Jemian, P. R.; Levine, L. E.; Allen, A. J. Development of Combined Microstructure and Structure Characterization Facility for in Situ and Operando Studies at the Advanced Photon Source. *J. Appl. Crystallogr.* **2018**, *51* (3), 867–882. https://doi.org/10.1107/S160057671800643X.
(125) Pozzo, L. *USAXS 48 Solid Film Holder*. https://www.thingiverse.com/thing:4639006/files (accessed 2020-11-02).
(126) Ilavsky, J. Nika : Software for Two-Dimensional Data Reduction. *J. Appl. Crystallogr.* **2012**, *45* (2), 324–328. https://doi.org/10.1107/S0021889812004037.
(127) Mitchell, G. R.; Windle, A. H. Structure of Polystyrene Glasses. *Polymer* **1984**, *25* (7), 906–920. https://doi.org/10.1016/0032-3861(84)90073-9.

(128) Gillich, D. J.; Kovanen, A.; Danon, Y. Deuterated Target Comparison for Pyroelectric Crystal D–D Nuclear Fusion Experiments. *J. Nucl. Mater.* **2010**, *405* (2), 181–185. https://doi.org/10.1016/j.jnucmat.2010.08.012.
(129) Wallace, W. E.; Beck Tan, N. C.; Wu, W. L.; Satija, S. Mass Density of Polystyrene Thin Films Measured by Twin Neutron Reflectivity. *J. Chem. Phys.* **1998**, *108* (9), 3798–3804. https://doi.org/10.1063/1.475769.
(130) Toolan, D. T. W.; Barker, R.; Gough, T.; Topham, P. D.; Howse, J. R.; Glidle, A. Gravimetric and Density Profiling Using the Combination of Surface Acoustic Waves and Neutron Reflectivity. *J. Colloid Interface Sci.* **2017**, *487*, 465–474. https://doi.org/10.1016/j.jcis.2016.10.039.
(131) Lu, G.; Blakesley, J.; Himmelberger, S.; Pingel, P.; Frisch, J.; Lieberwirth, I.; Salzmann, I.; Oehzelt, M.; Di Pietro, R.; Salleo, A.; Koch, N.; Neher, D. Moderate Doping Leads to High Performance of Semiconductor/Insulator Polymer Blend Transistors. *Nat. Commun.* **2013**, *4* (1), 1588. https://doi.org/10.1038/ncomms2587.
(132) Qiu, L.; Wang, X.; Lee, W. H.; Lim, J. A.; Kim, J. S.; Kwak, D.; Cho, K. Organic Thin-Film Transistors Based on Blends of Poly(3-Hexylthiophene) and Polystyrene with a Solubility-Induced Low Percolation Threshold. *Chem. Mater.* **2009**, *21* (19), 4380–4386. https://doi.org/10.1021/cm900628j.
(133) Qiu, L.; Lee, W. H.; Wang, X.; Kim, J. S.; Lim, J. A.; Kwak, D.; Lee, S.; Cho, K. Organic Thin-Film Transistors Based on Polythiophene Nanowires Embedded in Insulating Polymer. *Adv. Mater.* **2009**, *21* (13), 1349–1353. https://doi.org/10.1002/adma.200802880.
(134) Hellmann, C.; Treat, N. D.; Scaccabarozzi, A. D.; Razzell Hollis, J.; Fleischli, F. D.; Bannock, J. H.; de Mello, J.; Michels, J. J.; Kim, J.-S.; Stingelin, N. Solution Processing of Polymer Semiconductor: Insulator Blends-Tailored Optical Properties through Liquid-Liquid Phase Separation Control. *J. Polym. Sci. Part B Polym. Phys.* **2015**, *53* (4), 304–310. https://doi.org/10.1002/polb.23656.
(135) Goffri, S.; Müller, C.; Stingelin-Stutzmann, N.; Breiby, D. W.; Radano, C. P.; Andreasen, J. W.; Thompson, R.; Janssen, R. A. J.; Nielsen, M. M.; Smith, P.; Sirringhaus, H. Multicomponent Semiconducting Polymer Systems with Low Crystallization-Induced Percolation Threshold. *Nat. Mater.* **2006**, *5* (12), 950–956. https://doi.org/10.1038/nmat1779.
(136) Kumar, A.; Baklar, M. A.; Scott, K.; Kreouzis, T.; Stingelin-Stutzmann, N. Efficient, Stable Bulk Charge Transport in Crystalline/Crystalline Semiconductor-Insulator Blends. *Adv. Mater.* **2009**, *21* (44), 4447–4451. https://doi.org/10.1002/adma.200900717.
(137) Liu, J.; Arif, M.; Zou, J.; Khondaker, S. I.; Zhai, L. Controlling Poly(3-Hexylthiophene) Crystal Dimension: Nanowhiskers and Nanoribbons. *Macromolecules 42* (24), 9390–9393. https://doi.org/10.1021/ma901955c.
(138) Keum, J. K.; Xiao, K.; Ivanov, I. N.; Hong, K.; Browning, J. F.; Smith, G. S.; Shao, M.; Littrell, K. C.; Rondinone, A. J.; Andrew Payzant, E.; Chen, J.; Hensley, D. K. Solvent Quality-Induced Nucleation and Growth of Parallelepiped Nanorods in Dilute Poly(3-Hexylthiophene) (P3HT) Solution and the Impact on the Crystalline Morphology of Solution-Cast Thin Film. *CrystEngComm* **2013**, *15* (6), 1114–1124. https://doi.org/10.1039/C2CE26666K.
(139) Bastianini, F.; Pérez, G. E.; Hobson, A. R.; Rogers, S. E.; Parnell, A. J.; Grell, M.; Gutiérrez, A. F.; Dunbar, A. D. F. In−situ Monitoring Poly(3-Hexylthiophene) Nanowire Formation

and Shape Evolution in Solution via Small Angle Neutron Scattering. *Sol. Energy Mater. Sol. Cells* **2019**, *202*, 110128. https://doi.org/10.1016/j.solmat.2019.110128.
(140) Agbolaghi, S.; Zenoozi, S. A Comprehensive Review on Poly(3-Alkylthiophene)-Based Crystalline Structures, Protocols and Electronic Applications. *Org. Electron. 51*, 362–403. https://doi.org/10.1016/j.orgel.2017.09.038.
(141) Merlo, J. A.; Frisbie, C. D. Field Effect Transport and Trapping in Regioregular Polythiophene Nanofibers. *J. Phys. Chem. B 108* (50), 19169–19179. https://doi.org/10.1021/jp047023a.
(142) Salzmann, I.; Heimel, G.; Oehzelt, M.; Winkler, S.; Koch, N. Molecular Electrical Doping of Organic Semiconductors: Fundamental Mechanisms and Emerging Dopant Design Rules. *Acc. Chem. Res.* **2016**, *49* (3), 370–378. https://doi.org/10.1021/acs.accounts.5b00438.
(143) Snyder, C. R.; Nieuwendaal, R. C.; DeLongchamp, D. M.; Luscombe, C. K.; Sista, P.; Boyd, S. D. Quantifying Crystallinity in High Molar Mass Poly(3-Hexylthiophene). *Macromolecules* **2014**, *47* (12), 3942–3950. https://doi.org/10.1021/ma500136d.
(144) Samitsu, S.; Shimomura, T.; Heike, S.; Hashizume, T.; Ito, K. Field-Effect Carrier Transport in Poly(3-Alkylthiophene) Nanofiber Networks and Isolated Nanofibers. *Macromolecules* **2010**, *43* (19), 7891–7894. https://doi.org/10.1021/ma101655s.
(145) Dierckx, W.; Oosterbaan, W. D.; Bolsée, J.-C.; Maes, W.; Vanderzande, D.; Manca, J. Poly(3-Alkylthiophene) Nanofibers for Optoelectronic Devices. *J. Mater. Chem. C* **2014**, *2* (29), 5730. https://doi.org/10.1039/c4tc00308j.
(146) Newbloom, G. M.; de la Iglesia, P.; Pozzo, L. D. Controlled Gelation of Poly(3-Alkylthiophene)s in Bulk and in Thin-Films Using Low Volatility Solvent/Poor-Solvent Mixtures. *Soft Matter* **2014**, *10* (44), 8945–8954. https://doi.org/10.1039/C4SM00960F.
(147) Schara, S.; Blau, R.; Church, D. C.; Pokorski, J. K.; Lipomi, D. J. Polymer Chemistry for Haptics, Soft Robotics, and Human–Machine Interfaces. *Adv. Funct. Mater.* **2021**, *31* (39), 2008375. https://doi.org/10.1002/adfm.202008375.
(148) St. Onge, P. B. J.; Ocheje, M. U.; Selivanova, M.; Rondeau-Gagné, S. Recent Advances in Mechanically Robust and Stretchable Bulk Heterojunction Polymer Solar Cells. *Chem. Rec.* **2019**, *19* (6), 1008–1027. https://doi.org/10.1002/tcr.201800163.
(149) Sugiyama, F.; Kleinschmidt, A. T.; Kayser, L. V.; Rodriquez, D.; Finn, M.; Alkhadra, M. A.; Wan, J. M.-H.; Ramírez, J.; Chiang, A. S.-C.; Root, S. E.; Savagatrup, S.; Lipomi, D. J. Effects of Flexibility and Branching of Side Chains on the Mechanical Properties of Low-Bandgap Conjugated Polymers. *Polym. Chem.* **2018**, *9* (33), 4354–4363. https://doi.org/10.1039/C8PY00820E.
(150) Moulton, J.; Smith, P. Electrical and Mechanical Properties of Oriented Poly(3-Alkylthiophenes): 2. Effect of Side-Chain Length. *Polymer* **1992**, *33* (11), 2340–2347. https://doi.org/10.1016/0032-3861(92)90525-2.
(151) Savagatrup, S.; Printz, A. D.; Rodriquez, D.; Lipomi, D. J. Best of Both Worlds: Conjugated Polymers Exhibiting Good Photovoltaic Behavior and High Tensile Elasticity. *Macromolecules* **2014**, *47* (6), 1981–1992. https://doi.org/10.1021/ma500286d.
(152) Bridges, C. R.; Ford, M. J.; Thomas, E. M.; Gomez, C.; Bazan, G. C.; Segalman, R. A. Effects of Side Chain Branch Point on Self Assembly, Structure, and Electronic Properties of High Mobility Semiconducting Polymers. *Macromolecules* **2018**, *51* (21), 8597–8604. https://doi.org/10.1021/acs.macromol.8b01906.

(153) Ma, Z.; Geng, H.; Wang, D.; Shuai, Z. Influence of Alkyl Side-Chain Length on the Carrier Mobility in Organic Semiconductors: Herringbone vs. Pi–Pi Stacking. *J. Mater. Chem. C* **2016**, *4* (20), 4546–4555. https://doi.org/10.1039/C6TC00755D.
(154) Lamport, Z. A.; Barth, K. J.; Lee, H.; Gann, E.; Engmann, S.; Chen, H.; Guthold, M.; McCulloch, I.; Anthony, J. E.; Richter, L. J.; DeLongchamp, D. M.; Jurchescu, O. D. A Simple and Robust Approach to Reducing Contact Resistance in Organic Transistors. *Nat. Commun.* **2018**, *9* (1), 5130. https://doi.org/10.1038/s41467-018-07388-3.
(155) Li, Y.; Tatum, W. K.; Onorato, J. W.; Zhang, Y.; Luscombe, C. K. Low Elastic Modulus and High Charge Mobility of Low-Crystallinity Indacenodithiophene-Based Semiconducting Polymers for Potential Applications in Stretchable Electronics. *Macromolecules* **2018**, *51* (16), 6352–6358. https://doi.org/10.1021/acs.macromol.8b00898.
(156) Zheng, Y.; Wang, G. N.; Kang, J.; Nikolka, M.; Wu, H.; Tran, H.; Zhang, S.; Yan, H.; Chen, H.; Yuen, P. Y.; Mun, J.; Dauskardt, R. H.; McCulloch, I.; Tok, J. B. -H.; Gu, X.; Bao, Z. An Intrinsically Stretchable High-Performance Polymer Semiconductor with Low Crystallinity. *Adv. Funct. Mater.* **2019**, 1905340–1905340. https://doi.org/10.1002/adfm.201905340.
(157) Sommerville, P. J. W.; Li, Y.; Dong, B. X.; Zhang, Y.; Onorato, J. W.; Tatum, W. K.; Balzer, A. H.; Stingelin, N.; Patel, S. N.; Nealey, P. F.; Luscombe, C. K. Elucidating the Influence of Side-Chain Circular Distribution on the Crack Onset Strain and Hole Mobility of Near-Amorphous Indacenodithiophene Copolymers. *Macromolecules* **2020**, *53* (17), 7511–7518. https://doi.org/10.1021/acs.macromol.0c00512.
(158) Ilavsky, J. Nika: Software for Two-Dimensional Data Reduction. *J. Appl. Crystallogr.* **2012**, *45* (2), 324–328. https://doi.org/10.1107/S0021889812004037.
(159) Oosterhout, S. D.; Savikhin, V.; Zhang, J.; Zhang, Y.; Burgers, M. A.; Marder, S. R.; Bazan, G. C.; Toney, M. F. Mixing Behavior in Small Molecule:Fullerene Organic Photovoltaics. *Chem. Mater.* **2017**, *29* (7), 3062–3069. https://doi.org/10.1021/acs.chemmater.7b00067.
(160) Reimschuessel, H. K. On the Glass Transition Temperature of Comblike Polymers: Effects of Side Chain Length and Backbone Chain Structure. *J. Polym. Sci. Polym. Chem. Ed.* **1979**, *17* (8), 2447–2457. https://doi.org/10.1002/pol.1979.170170817.
(161) Cendra, C.; Balhorn, L.; Zhang, W.; O'Hara, K.; Bruening, K.; Tassone, C. J.; Steinrück, H.-G.; Liang, M.; Toney, M. F.; McCulloch, I.; Chabinyc, M. L.; Salleo, A.; Takacs, C. J. Unraveling the Unconventional Order of a High-Mobility Indacenodithiophene–Benzothiadiazole Copolymer. *ACS Macro Lett.* **2021**, *10* (10), 1306–1314. https://doi.org/10.1021/acsmacrolett.1c00547.
(162) Chen, H.; Wadsworth, A.; Ma, C.; Nanni, A.; Zhang, W.; Nikolka, M.; Luci, A. M. T.; Perdigão, L. M. A.; Thorley, K. J.; Cendra, C.; Larson, B.; Rumbles, G.; Anthopoulos, T. D.; Salleo, A.; Costantini, G.; Sirringhaus, H.; McCulloch, I. The Effect of Ring Expansion in Thienobenzo[b]Indacenodithiophene Polymers for Organic Field-Effect Transistors. *J. Am. Chem. Soc.* **2019**, *141* (47), 18806–18813. https://doi.org/10.1021/jacs.9b09367.
(163) Kline, R. J.; DeLongchamp, D. M.; Fischer, D. A.; Lin, E. K.; Richter, L. J.; Chabinyc, M. L.; Toney, M. F.; Heeney, M.; McCulloch, I. Critical Role of Side-Chain Attachment Density on the Order and Device Performance of Polythiophenes. *Macromolecules* **2007**, *40* (22), 7960–7965. https://doi.org/10.1021/ma0709001.
(164) Eder, T.; Stangl, T.; Gmelch, M.; Remmerssen, K.; Laux, D.; Höger, S.; Lupton, J. M.; Vogelsang, J. Switching between H- and J-Type Electronic Coupling in Single Conjugated

Polymer Aggregates. *Nat. Commun.* **2017**, *8* (1), 1641. https://doi.org/10.1038/s41467-017-01773-0.
(165) Venkateshvaran, D.; Nikolka, M.; Sadhanala, A.; Lemaur, V.; Zelazny, M.; Kepa, M.; Hurhangee, M.; Kronemeijer, A. J.; Pecunia, V.; Nasrallah, I.; Romanov, I.; Broch, K.; McCulloch, I.; Emin, D.; Olivier, Y.; Cornil, J.; Beljonne, D.; Sirringhaus, H. Approaching Disorder-Free Transport in High-Mobility Conjugated Polymers. *Nature* **2014**, *515* (7527), 384–388. https://doi.org/10.1038/nature13854.
(166) Zhang, S.; Galuska, L. A.; Gu, X. Water-Assisted Mechanical Testing of Polymeric Thin-Films. *J. Polym. Sci.* **2022**, *60* (7), 1108–1129. https://doi.org/10.1002/pol.20210281.
(167) Koch, F. P. V.; Heeney, M.; Smith, P. Thermal and Structural Characteristics of Oligo(3-Hexylthiophene)s (3HT)n, n = 4–36. *J. Am. Chem. Soc.* **2013**, *135* (37), 13699–13709. https://doi.org/10.1021/ja405792b.
(168) O'Connor, B.; Chan, E. P.; Chan, C.; Conrad, B. R.; Richter, L. J.; Kline, R. J.; Heeney, M.; McCulloch, I.; Soles, C. L.; DeLongchamp, D. M. Correlations between Mechanical and Electrical Properties of Polythiophenes. *ACS Nano* **2010**, *4* (12), 7538–7544. https://doi.org/10.1021/nn1018768.
(169) Rodriquez, D.; Kim, J.-H.; Root, S. E.; Fei, Z.; Boufflet, P.; Heeney, M.; Kim, T.-S.; Lipomi, D. J. Comparison of Methods for Determining the Mechanical Properties of Semiconducting Polymer Films for Stretchable Electronics. *ACS Appl. Mater. Interfaces* **2017**, *9* (10), 8855–8862. https://doi.org/10.1021/acsami.6b16115.
(170) Griffin, M. F.; Leung, B. C.; Premakumar, Y.; Szarko, M.; Butler, P. E. Comparison of the Mechanical Properties of Different Skin Sites for Auricular and Nasal Reconstruction. *J. Otolaryngol. - Head Neck Surg.* **2017**, *46* (1), 33. https://doi.org/10.1186/s40463-017-0210-6.
(171) Savagatrup, S.; Zhao, X.; Chan, E.; Mei, J.; Lipomi, D. J. Effect of Broken Conjugation on the Stretchability of Semiconducting Polymers. *Macromol. Rapid Commun.* **2016**, *37* (19), 1623–1628. https://doi.org/10.1002/marc.201600377.
(172) Zhang, W.; Han, Y.; Zhu, X.; Fei, Z.; Feng, Y.; Treat, N. D.; Faber, H.; Stingelin, N.; McCulloch, I.; Anthopoulos, T. D.; Heeney, M. A Novel Alkylated Indacenodithieno[3,2-b]Thiophene-Based Polymer for High-Performance Field-Effect Transistors. *Adv. Mater.* **2016**, *28* (20), 3922–3927. https://doi.org/10.1002/adma.201504092.
(173) Chen, H.; Hurhangee, M.; Nikolka, M.; Zhang, W.; Kirkus, M.; Neophytou, M.; Cryer, S. J.; Harkin, D.; Hayoz, P.; Abdi-Jalebi, M.; McNeill, C. R.; Sirringhaus, H.; McCulloch, I. Dithiopheneindenofluorene (TIF) Semiconducting Polymers with Very High Mobility in Field-Effect Transistors. *Adv. Mater.* **2017**, *29* (36), 1702523. https://doi.org/10.1002/adma.201702523.
(174) *Mixed-Ligand Approach to Palladium-Catalyzed Direct Arylation Polymerization: Effective Prevention of Structural Defects Using Diamines*. ACS Publications. https://pubs-acs-org.offcampus.lib.washington.edu/doi/full/10.1021/acs.macromol.6b00441 (accessed 2024-05-23).
(175) Sommerville, P. J. W.; Balzer, A. H.; Lecroy, G.; Guio, L.; Wang, Y.; Onorato, J. W.; Kukhta, N. A.; Gu, X.; Salleo, A.; Stingelin, N.; Luscombe, C. K. Influence of Side Chain Interdigitation on Strain and Charge Mobility of Planar Indacenodithiophene Copolymers. *ACS Polym. Au* **2023**, *3* (1), 59–69. https://doi.org/10.1021/acspolymersau.2c00034.
(176) Ponder Jr, J. F.; Chen, H.; Luci, A. M. T.; Moro, S.; Turano, M.; Hobson, A. L.; Collier, G. S.; Perdigão, L. M. A.; Moser, M.; Zhang, W.; Costantini, G.; Reynolds, J. R.; McCulloch,

I. Low-Defect, High Molecular Weight Indacenodithiophene (IDT) Polymers Via a C–H Activation: Evaluation of a Simpler and Greener Approach to Organic Electronic Materials. *ACS Mater. Lett.* **2021**, *3* (10), 1503–1512. https://doi.org/10.1021/acsmaterialslett.1c00478.

(177) Makki, H.; Burke, C. A.; Troisi, A. Microstructural Model of Indacenodithiophene-Co-Benzothiadiazole Polymer: π-Crossing Interactions and Their Potential Impact on Charge Transport. *J. Phys. Chem. Lett.* **2023**, *14* (39), 8867–8873. https://doi.org/10.1021/acs.jpclett.3c02305.

(178) Spano, F. C.; Silva, C. H- and J-Aggregate Behavior in Polymeric Semiconductors. *Annu. Rev. Phys. Chem.* **2014**, *65* (Volume 65, 2014), 477–500. https://doi.org/10.1146/annurev-physchem-040513-103639.

(179) O'Neill, L.; Byrne, H. J. Structure−Property Relationships for Electron−Vibrational Coupling in Conjugated Organic Oligomeric Systems. *J. Phys. Chem. B* **2005**, *109* (26), 12685–12690. https://doi.org/10.1021/jp050039w.

(180) Keum, J. K.; Xiao, K.; Ivanov, I. N.; Hong, K.; Browning, J. F.; Smith, G. S.; Shao, M.; Littrell, K. C.; Rondinone, A. J.; Payzant, E. A.; Chen, J.; Hensley, D. K. Solvent Quality-Induced Nucleation and Growth of Parallelepiped Nanorods in Dilute Poly(3-Hexylthiophene) (P3HT) Solution and the Impact on the Crystalline Morphology of Solution-Cast Thin Film. *CrystEngComm* **2013**, *15* (6), 1114–1124. https://doi.org/10.1039/C2CE26666K.

(181) Nawrocki, R. A.; Pavlica, E.; Ćelić, N.; Orlov, D.; Valant, M.; Mihailović, D.; Bratina, G. Fabrication of Poly(3-Hexylthiophene) Nanowires for High-Mobility Transistors. *Org. Electron.* **2016**, *30*, 92–98. https://doi.org/10.1016/j.orgel.2015.11.038.

(182) Mazzio, K. A.; Rice, A. H.; Durban, M. M.; Luscombe, C. K. Effect of Regioregularity on Charge Transport and Structural and Excitonic Coherence in Poly(3-Hexylthiophene) Nanowires. *J. Phys. Chem. C* **2015**, *119* (27), 14911–14918. https://doi.org/10.1021/acs.jpcc.5b02914.

(183) Tatum, W. K.; Luscombe, C. K. π-Conjugated Polymer Nanowires: Advances and Perspectives toward Effective Commercial Implementation. *Polym. J.* **2018**, *50* (8), 659–669. https://doi.org/10.1038/s41428-018-0062-6.

(184) Xi, Y.; Wolf, C. M.; Pozzo, L. D. Self-Assembly of Donor–Acceptor Conjugated Polymers Induced by Miscible 'Poor' Solvents. *Soft Matter* **2019**, *15* (8), 1799–1812. https://doi.org/10.1039/C8SM02517G.

(185) Li, M.; Bin, H.; Jiao, X.; Wienk, M. M.; Yan, H.; Janssen, R. A. J. Controlling the Microstructure of Conjugated Polymers in High-Mobility Monolayer Transistors via the Dissolution Temperature. *Angew. Chem. Int. Ed.* **2020**, *59* (2), 846–852. https://doi.org/10.1002/anie.201911311.

(186) Danielsen, S. P. O.; Bridges, C. R.; Segalman, R. A. Chain Stiffness of Donor–Acceptor Conjugated Polymers in Solution. *Macromolecules* **2022**, *55* (2), 437–449. https://doi.org/10.1021/acs.macromol.1c02229.

(187) Morimoto, M.; Fukatsu, N.; Tanaka, R.; Takanohashi, T.; Kumagai, H.; Morita, T.; Tykwinski, R. R.; Scott, D. E.; Stryker, J. M.; Gray, M. R.; Sato, T.; Yamamoto, H. Determination of Hansen Solubility Parameters of Asphaltene Model Compounds. *Energy Fuels* **2018**, *32* (11), 11296–11303. https://doi.org/10.1021/acs.energyfuels.8b02661.

(188) Hansen, C. M. *Hansen Solubility Parameters: A User's Handbook, Second Edition*, 2nd ed.; CRC Press: Boca Raton, 2007. https://doi.org/10.1201/9781420006834.

(189) Jin, T.; Li, J.; Li, H.; Liu, X.; Li, J.; Zhang, Q.; Yu, X.; Duan, X.; Han, Y. Improving the Hole Mobility of Conjugated Semiconducting Polymer Films by Fast Backbone Aggregation during the Film Formation Process. *J. Mater. Chem. C* **2024**, *12* (14), 5047–5061. https://doi.org/10.1039/D4TC00148F.
(190) Chen, W.-R.; Butler, P. D.; Magid, L. J. Incorporating Intermicellar Interactions in the Fitting of SANS Data from Cationic Wormlike Micelles. *Langmuir* **2006**, *22* (15), 6539–6548. https://doi.org/10.1021/la0530440.

Appendix D: List of Publications

1. LeCroy, G.; Ghosh, R.; Untilova, V.; **Guio, L**.; Stone, K. H.; Brinkmann, M.; Luscombe, C.; Spano, F. C.; Salleo, A. Polaron Absorption in Aligned Conjugated Polymer Films: Breakdown of Adiabatic Treatments and Going beyond the Conventional Mid-Gap State Model. *Mater. Horiz.* **2024**, *11* (2), 545–553. https://doi.org/10.1039/D3MH01278F.
2. **Guio, L**.; Liu, C.; Boures, D.; Getty, P. T.; Waldman, R.; Liu, X.; Darling, S. B. Procedure for the Transfer of Polymer Films Onto Porous Substrates with Minimized Defects. *JoVE (Journal of Visualized Experiments)* **2019**, No. 148, e59554. https://doi.org/10.3791/59554.
3. Wolf, C. M.; **Guio, L**.; Scheiwiller, S.; Pakhnyuk, V.; Luscombe, C.; Pozzo, L. D. Strategies for the Development of Conjugated Polymer Molecular Dynamics Force Fields Validated with Neutron and X-Ray Scattering. *ACS Polym. Au* **2021**, *1* (3), 134–152. https://doi.org/10.1021/acspolymersau.1c00027.
4. Zasada, L. B.; **Guio, L**.; Kamin, A. A.; Dhakal, D.; Monahan, M.; Seidler, G. T.; Luscombe, C. K.; Xiao, D. J. Conjugated Metal–Organic Macrocycles: Synthesis, Characterization, and Electrical Conductivity. *J. Am. Chem. Soc.* **2022**, *144* (10), 4515–4521. https://doi.org/10.1021/jacs.1c12596.
5. Wolf, C. M.; **Guio, L**.; Scheiwiller, S. C.; O'Hara, R. P.; Luscombe, C. K.; Pozzo, L. D. Blend Morphology in Polythiophene–Polystyrene Composites from Neutron and X-Ray Scattering. *Macromolecules* **2021**, *54* (6), 2960–2978. https://doi.org/10.1021/acs.macromol.0c02512.
6. Sommerville, P. J. W.; Balzer, A. H.; Lecroy, G.; **Guio, L**.; Wang, Y.; Onorato, J. W.; Kukhta, N. A.; Gu, X.; Salleo, A.; Stingelin, N.; Luscombe, C. K. Influence of Side Chain

Interdigitation on Strain and Charge Mobility of Planar Indacenodithiophene Copolymers. *ACS Polym. Au* **2023**, *3* (1), 59–69. https://doi.org/10.1021/acspolymersau.2c00034.

Appendix E: Vita

Lorenzo Guio was born in Bogota, Colombia. He moved with his family at a very young age to Miami, Florida where he grew up and began his early education. He began his research career at the University of Chicago, where he originally began a degree in physics. After switching to the newly minted program in molecular engineering, he worked with the lab of Prof. Seth Darling on developing film transfer methods. He was one of 12 students that became the first undergraduate cohort from the Pritzker School of Molecular Engineering in 2018. That fall, he began pursuing a master's degree in materials science and engineering with Prof. Christine Luscombe at the University of Washington focusing on polymer synthesis. In the Fall of 2019, he continued to pursue a PhD in materials science and engineering co-advised by Prof. Luscombe and Prof. Lilo Pozzo focusing on neutron and x-ray scattering, polymer synthesis and transistor fabrication and testing. During the 6 years he has been at UW, he has had the opportunity to collaborate with pioneers in the field, do research in Japan for 6 months, and start two companies.